UNIVERSITY OF CALIFORNIA,

IRVINE

Design and Optimization of Nanomaterials for Sensing Applications

DISSERTATION

submitted in partial satisfaction of the requirements

for the degree of

DOCTOR OF PHILOSOPHY

in Physics

by

Robert Noboru Sanderson

Dissertation Committee:
Professor Regina Ragan, Chair
Professor Reginald Penner
Professor Ruqian Wu

2017

DEDICATION

To

Jamie

Table of Contents

LIST OF FIGURES

Page

LIST OF TABLES

Page

ACKNOWLEDGMENTS

I would like to thank my committee chair and principal advisor, Professor Regina Ragan, who has offered me guidance, compassion, and support through my tenure as a graduate student. Her passion for research and academics has inspired me, and without her help this dissertation would not have been possible

I would also like to thank my committee members, Professor Ruqian Wu and Professor Reginald Penner for their insightful conversations, guidance, and patience.

Thank you, Professor Jory Yarmoff of UC Riverside, whose advice and support during my time as an undergraduate set me upon the path toward graduate study.

I thank IOP Publishing for permission to include Chapter 3 and the American Chemical Society for permission to include Chapter 4. I also thank the National Science Foundation for financial support.

ABSTRACT OF THE DISSERTATION

Design and Optimization of Nanomaterials for Sensing Applications

By

Robert Noboru Sanderson

Doctor of Physics

University of California, Irvine, 2017

Professor Regina Ragan, Chair

Nanomaterials, materials with one or more of their dimensions on the nanoscale, have emerged as an important field in the development of next-generation sensing systems. Their high surface-to-volume ratio makes them useful for sensing, but also makes them sensitive to processing defects and inherent material defects. To develop and optimize these systems, it is thus necessary to characterize these defects to understand their origin and how to work around them. Scanning probe microscopy (SPM) techniques like atomic force microscopy (AFM) and scanning tunneling microscopy (STM) are important characterization methods which can measure nanoscale topography and electronic structure. These methods are appealing in nanomaterial systems because they are non-damaging and provide local, high-resolution data, and so are capable of detecting nanoscale features such as single defect sites. There are difficulties, however, in the interpretation of SPM data. For instance, AFM-based methods are prone to experimental artifacts due to long-range interactions, such as capacitive crosstalk in

Kelvin probe force microscopy (KPFM), and artifacts due to the finite size of the probe tip, such as incorrect surface tracking at steep topographical features. Mechanical characterization (via force spectroscopy) of nanomaterials with significant nanoscale variations, such as tethered lipid bilayer membranes (tLBMs), is also difficult since variations in the bulk system's mechanical behavior must be distinguished from local fluctuations. Additionally, interpretation of STM data is non-trivial due to local variations in electron density in addition to topographical variations.

In this thesis we overcome some limitations of SPM methods by supplementing them with additional surface analytical methods as well as computational methods, and we characterize several nanomaterial systems. Current-carrying vapor-liquid-solid Si nanowires (useful for interdigitated-electrode-based sensors) are characterized using finite-element-method (FEM)-supplemented KPFM to retrieve useful information about processing defects, contact resistance, and the primary charge carriers. Next, a tLBM system's stiffness and the stiffness' dependence on tethering molecule concentration is measured using statistical analysis of thousands of AFM force spectra, demonstrating a biosensor-compatible system with a controllable bulk rigidity. Finally, we utilize surface analytical techniques to inform the development of a novel three-dimensional graphene system for sensing applications.

CHAPTER I: Introduction

A chemical sensor is any device that converts a concentration of a target material into a "signal"; a measurable quantity. There are many mechanisms by which these devices can operate. For example, there are chemiresistors and chemicapacitors for gas sensing, electrochemical sensors for gas and liquid concentration sensing, and even biologically inspired sensors composed of lipid bilayer membranes for the detection of single viruses. In recent decades, nanomaterials have risen as tools to optimize these sensors. This chapter will give a brief overview of nanomaterial-based chemical sensors, emphasizing the systems to be discussed in this dissertation, followed by a discussion of the properties of graphene and its role in next-generation nanosensors.

Nanomaterials for Sensing Applications

Nanomaterials have several advantages over traditional materials in sensing applications. First, their higher specific surface area makes their transport properties sensitive to adsorbed species, and as a result chemiresistors and chemicapacitors benefit from increased sensitivity. There is a similar benefit to selectivity, since the surface can be functionalized to be sensitive to a single process, and the selection process during chemical sensing is more impactful with a higher surface-to-volume ratio.[1] Additionally, nanomaterial devices can be designed to be smaller and less massive than traditional materials, which can be a great benefit for portable applications.

One-dimensional nanomaterials such as semiconducting nanowires are very important systems in the development of nanosensors due to their high aspect ratio, mechanical strength,

small size, and low cost.[2] Silicon nanowires in particular have gained attention as gas sensors and electrochemical sensors in recent years due to their reliability, sensitivity, and well-characterized growth processes.[3,4]

Planar nanosensors are frequently seen as well. Examples of these include thin-film gas sensors[5], biosensors derived from supported lipid bilayer membranes[6,7], and various sensors derived from graphene films[8–11]. These planar systems have the advantages of having a reduced dimensionality (compared to a three-dimensional crystal) which increases their surface area relative to their volume, they can benefit from enhanced structural stability compared to one-dimensional nanosystems, and they can have other chemical or electronic properties not possible in a one-dimensional system. As examples of this last point, supported lipid bilayer membrane systems can act to mimic cell membranes[12], and graphene has an extremely high electron mobility not found in carbon nanotubes[13].

Structure of the Dissertation

In Chapter 2, the experimental methods used in this work are outlined, and brief discussions of their advantages and disadvantages in characterizing sensing systems are given. First, scanning probe techniques are outlined, giving introductions to atomic force microscopy (AFM), Kelvin probe force microscopy (KPFM) and AFM force spectroscopy. Raman spectroscopy is then discussed, along with a thorough discussion of the characterization of graphene systems. Then, a derivation of the operating principles of scanning tunneling microscopy (STM) is given. This chapter concludes with brief discussions of additional techniques.

In Chapter 3, Kelvin probe force microscopy (KPFM) is used to characterize electrical characteristics of vapor-liquid-solid Si nanowires under an applied current. KPFM measurements detect changes surface potential, and we demonstrate that the varied contributions to the surface potential can be accounted for with voltage normalization and oxide normalization, alongside finite element method simulations. These techniques demonstrate a robust technique allowing for the electrical characterization of Si nanowire systems under operating conditions.

In Chapter 4, unilamellar vesicles composed of 1-palmitoyl-2-oleoyl-*sn*-glycero-3-phosphocholine (POPC) modified with varying concentrations (0 mol%-24 mol%) of 1,2-distearoyl-*sn*-glycero-3-phosphoethanolamine-*N*-poly (ethylene glycol)-2000-*N*-[3-(2-pyridyldithio) propionate] (DSPE-PEG-PDP) are assembled on template-stripped gold surfaces, forming tethered lipid bilayer membranes (tLBMs). Force spectroscopy is used to measure changes in the Young's modulus of the modified films, and a dependence on DSPE-PEG-PDP concentration is found. These results indicate that these systems are a biologically inspired scaffold with tunable rigidity, which could allow for tLBMs to be used as biosensing scaffolds with a controllable stiffness.

Chapter 5 gives a thorough introduction to graphene, and lays out its desirable properties in the field of nanomaterial sensing.

In Chapter 6, a highly multiplexed three-dimensional graphene system is synthesized using a novel material; the bicontinuous interfacially jammed emulsion gel (bijel). This system is thoroughly characterized morphologically and electronically. Scanning electron microscopy (SEM) and surface area measurements indicate that a highly consistent open pore morphology is preserved through sample synthesis. Raman spectroscopy and scanning tunneling microscopy (STM) indicate the presence of multi-layer rotationally misaligned graphene.

Finally, in Chapter 7, this system's potential applications in nanosensing systems are discussed, and potential routes forward in its development are explored.

References

[1] K. C. Honeychurch, Nanosensors for Chemical and Biological Applications: Sensing with Nanotubes, Nanowires and Nanoparticles, Elsevier, **2014**.

[2] X. Zhao, B. Cai, Q. Tang, Y. Tong, Y. Liu, Sensors **2014**, 14, 13999.

[3] F. Demami, L. Ni, R. Rogel, A. C. Salaun, L. Pichon, Sens. Actuators B Chem. **2012**, 170, 158.

[4] Y. Cui, Q. Wei, H. Park, C. M. Lieber, Science **2001**, 293, 1289.

[5] I. EMMER, Int. J. Electron. **1992**, 73, 875.

[6] M. Bally, M. Graule, F. Parra, G. Larson, F. Höök, Biointerphases **2013**, 8, 4.

[7] X. Wang, Y. Zhang, H. Bi, X. Han, RSC Adv. **2016**, 6, 72821.

[8] J. T. Robinson, F. K. Perkins, E. S. Snow, Z. Wei, P. E. Sheehan, Nano Lett. **2008**, 8, 3137.

[9] J. D. Fowler, M. J. Allen, V. C. Tung, Y. Yang, R. B. Kaner, B. H. Weiller, ACS Nano **2009**, 3, 301.

[10] S. Basu, P. Bhattacharyya, Sens. Actuators B Chem. **2012**, 173, 1.

[11] S. S. Varghese, S. Lonkar, K. K. Singh, S. Swaminathan, A. Abdala, Sens. Actuators B Chem. **2015**, 218, 160.

[12] S. G. Boxer, Curr. Opin. Chem. Biol. **2000**, 4, 704.

[13] D. S. L. Abergel, V. Apalkov, J. Berashevich, K. Ziegler, T. Chakraborty, Adv. Phys. **2010**, 59, 261.

CHAPTER II: Experimental Techniques

This chapter contains descriptive overviews of the characterization techniques most important to the work in this dissertation.

Force Probe Methods

Atomic Force Microscopy and Kelvin Probe Force Microscopy

In non-contact AFM, a sharp probe tip is raster scanned across the surface of a sample. The tip is attached to a vibrating cantilever beam with a known resonance frequency f_0. Interaction forces act between the probe and sample when they are very near each other, and a force gradient acting on the tip due to tip-sample interactions will cause a change in the probe cantilever's resonance frequency approximated by[1]:

$$\Delta f_0 = -\frac{f_0}{2k}\frac{\partial F_{ts}}{\partial z}. \qquad \text{Equation 1}$$

In this expression, z is the tip position normal to the sample's surface, and the cantilever/tip system is considered a harmonic oscillator with spring constant k. It is seen that a force gradient translates to a change in the resonant frequency of the cantilever. Figure 1 shows the standard simplified model of the tip-sample interaction potential; the Lennard Jones interaction potential, given by

$$U_{LJ}\ \alpha\ (\frac{\sigma_0}{r})^{12} - (\frac{\sigma_0}{r})^{6}. \qquad \text{tio n 2}$$

Figure 1E qua

If one chooses a tip-sample separation corresponding to the highlighted region in the figure, it is found that the vibrational frequency of the cantilever/tip system increases as the tip-sample

separation increases and *vice versa*. Two modes of operation are frequently used which take advantage of this behavior: Amplitude modulation mode (AM-AFM) and frequency modulation mode (FM-AFM) of which only AM-AFM is considered in this thesis.

In AM-AFM, the cantilever is excited near resonance with constant drive amplitude. As the tip is scanned across a sample, changes in tip-sample separation cause changes in the force gradient, which causes a change in resonant frequency. This change in cantilever resonance is detected as a decrease in cantilever oscillation amplitude. A feedback loop is used to adjust the tip's z-position to bring the oscillation amplitude back to its target value, thereby measuring the local topography change. Recording the changes in the tip-sample separation yields a topographical map of the sample.

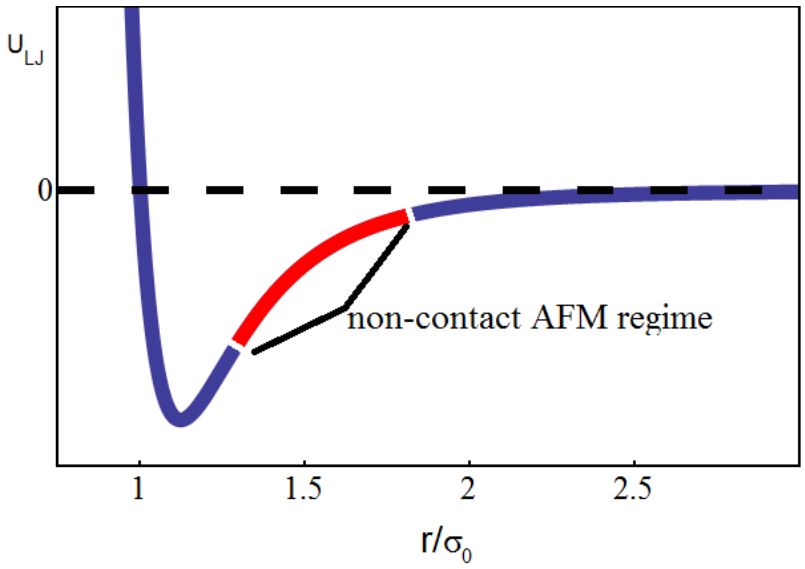

Figure 1 — Lennard-Jones Potential: The Lennard-Jones interaction potential provides a qualitative description of the tip-sample interaction in AFM. Highlighted in red is the region of interest during non-contact AFM experiments. $\boldsymbol{\sigma_0}$ is a characteristic length, and the potential ULJ is in arbitrary units.

KPFM is performed using the same basic apparatus as an AFM, except since this technique is sensitive to electrostatic interactions rather than the Lennard Jones interaction of

Equation 2, a conductive probe tip must be used to control the electrostatic potential of the probe.. In two-pass KPFM, AFM first determines the surface topography of a scan line, and then a second pass with a new feedback loop to minimize the electrostatic force by varying the tip-sample bias determines the local contact potential difference (CPD) between the probe and the sample. This allows for a detailed map of the CPD, which is essentially the local work function superposed with any other electronic potential variations.

Although KPFM is useful in mapping electronic structure, it is prone to experimental artifacts[22,27,28]. The electrostatic forces to which KPFM is sensitive are longer range than the Van der Waals interactions which dominate AFM studies, decaying as R^{-2} rather than R^{-7}. This long range behavior convolutes KPFM maps, making observed features a weighted average of surface potential features. This phenomenon makes careful interpretation of CPD measurements in KPFM essential in extracting useful information from the data. To accomplish this, computational work work as a supplement to atomic force studies has been demonstrated. Analytic computations from first-principles of simplified surface/probe systems have been used to understand the fundamental behavior of KPFM work[5,6]. Numerical simulations have also been used to approximate the probe/sample systems[3,4,7,8]. The inhomogeneous systems that are of interest to researchers studying devices are too complex to model analytically[4,8–10], so numerical approximations are more appropriate.

Finite element method (FEM) simulations are well suited to model complex geometries. . In FEM simulations, system geometries are divided into a finite number of elements, and continuous variables are discretized, and made constant within each of these elements. In this manner, the potential distributions in electrostatic systems with complex geometries that often arise in Kelvin probe experiments involving devices can be approximated. KPFM measurements

of various nanoscale potential distributions[3], surface topographies[4], and other phenomena such as grain boundaries[7,11] have been successfully modeled by using FEM simulations. By coupling FEM simulations with experimental data, it is possible to gain a better understanding of the surface topography and electronic structure of a surface when performing AFM/KPFM experiments.

Force Spectroscopy

FS is a family of experimental techniques that uses a mechanical force to probe the properties of a material. The work in this thesis focuses on FS on lipid bilayer membrane (LBM) samples performed using an atomic force microscope and all subsequent references to FS will refer to AFM-based FS of LBM systems. Here, an AFM probe tip is pressed down through a LBM and then retracted. The force data, the piezoelectric voltage data, and the tip deflection data are stored for analysis.

Correct interpretation of FS data requires an understanding of the dynamics of the AFM cantilever. Figure 2 shows schematically how the cantilever behaves during a FS experiment using a LBM on a hard substrate. In (a), the cantilever position z is adjusted to indent the tip into the sample. When contact is made, the cantilever beam deflects a distance d. The difference $|z|-|d|$ is the indentation distance δ, the position of the tip relative to the sample surface. The distance δ is the most widely used measurement value in AFM FS literature[12]. A closer view of the tip-sample interaction is shown in (b). The tip is brought into contact with the LBM, and pushed through it. The tip force as a function of δ for a sample FS experiment is shown in Figure 2(c). For large δ values, there is minimal force, since the tip does not interact with the surface. The vertical data points at $\delta = 0$ (Point A) indicate contact with the hard substrate. The jump between Point B and Point A is a breakthrough event, where the probe tip tears through the

LBM. Point C is the initial contact between tip and sample. These force/indentation spectra are useful measurements in FS, because they allow for the measurement of certain material properties of a surface. For instance, the rate at which the force increases with increased indentation (Point C) is related to the Young's modulus of the LBM. The exact relation needed to compute the Young's modulus is not simple, as it depends on tip geometry, tip-sample interactions, and LBM composition.

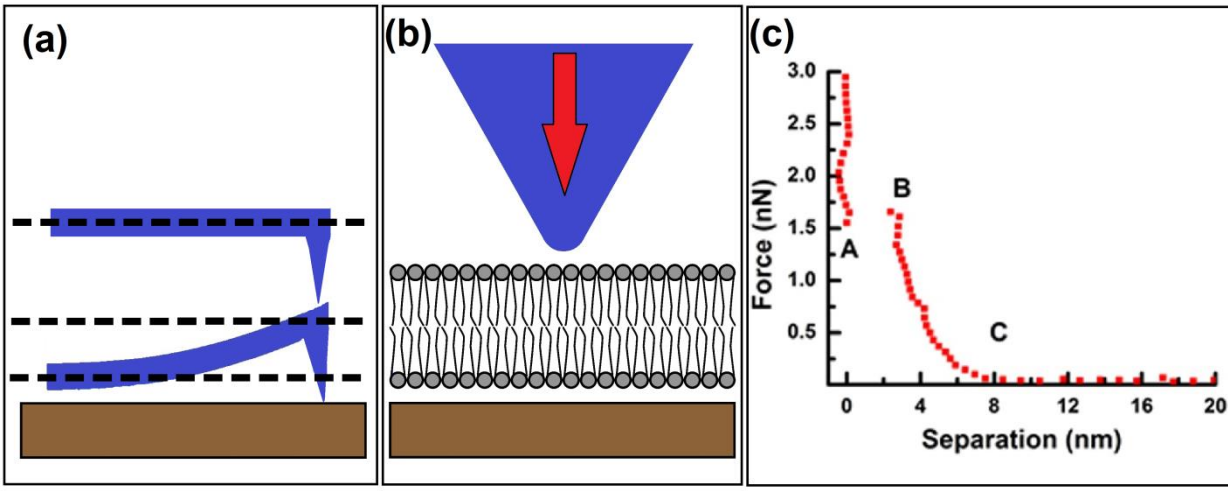

Figure 2 — Force Spectroscopy on Lipid Bilayers: (a) Schematic of cantilever behavior during FS. Tip-sample separation is calculated by taking the difference between the cantilever's displacement and its deflection. (b) Schematic representation of a tip being indented into a LBM during a FS experiment. (c) Force as a function of calculated tip-sample separation.

Models for tip force as a function of indentation have been the subject of much research in research years because of the rise of AFM FS as a materials characterization technique[13–19]. The Sneddon model isone such model that models a cone indenting into a semi-infinite elastic material[20]:

$$F_{Sneddon} = \frac{2}{\pi}\tan\theta\,\frac{E}{1-\nu^2}\delta^2. \qquad \text{Equation 3}$$

This expression relates the tip-sample force F to the indentation distance δ of the tip into the sample, with θ being the conical tip's opening angle, ν the Poisson ratio of the sample, and E the Young's modulus of the sample. The Sneddon model is a good approximation for the behavior of an elastic material, but it does not take into account the stiffness variation between the substrate and tLBM, causing the model to overestimate the membrane's Young's modulus. A modified model that accounts for the substrate stiffness, known as the bottom effect cone correction (BECC) model, is[21]:

$$F_{BECC} = \frac{8}{3\pi} E \tan\theta \, \delta^2 (1 + 1.7795 \, \frac{\tan\theta}{\pi^2} \frac{\delta}{h} + 16(1.7795)^2 tan^2\theta \, \frac{\delta^2}{h^2}). \quad \text{Equation 4}$$

In this adapted model, the finite thickness of the LBM is taken into account by considering an elastic membrane of thickness h on top of a semi-infinite rigid substrate.

Using these two models, the elastic modulus was computed for tLBMs using FS experimental data. Least-square fits of the force versus indentation data to the Sneddon and BECC models determine the elastic modulus of sample LBMs. A flow chart showing the basic logic behind the analysis of a single force-distance curve is shown in Figure 3. First, the force-distance data in the form of tab-separated text is imported as a list of ordered pairs and filtered to remove aberrational curves, such as those containing vibrational artifacts or multiple breakthrough events indicating overlap of LBMs. Three points of physical significance are then algorithmically determined: The hardwall contact point, the breakthrough point, and the contact point. The hardwall contact point corresponds to the point where the force versus indentation slope becomes infinite when the tip comes in contact with the hard substrate. The breakthrough point is the last point during the tip's approach before the tip overcomes the LBM's intra-membrane forces and breaks through, as signified by a sudden change of slope in the force-distance curve. The contact point is the point when the probe tip first comes in contact with the membrane surface. The locations of these points are determined and stored to be used in the modulus computations. The difference between the breakthrough point position and the hardwall contact point position is referred to as the breakthrough distance. An estimate for the total membrane thickness, computed as the difference between the contact point position and the hardwall contact point position, is referred to in this work as the onset compression distance. Finally, the data near the contact point are used in a native Mathematica fitting function to solve for the Young's modulus using either the Sneddon model (Equation 3) or the BECC model

(Equation 4), with appropriate parameter values substituted ($\theta = 35°$, $\nu = 0.5$, and h is given by the onset compression value.

Once this computation is completed for all sets of data, we can proceed to data analysis. The code used in this work calculated the breakthrough distance, onset compression distance, and Young's modulus for the LBM systems, allowing for a detailed analysis of changes in their stiffness and membrane strength.

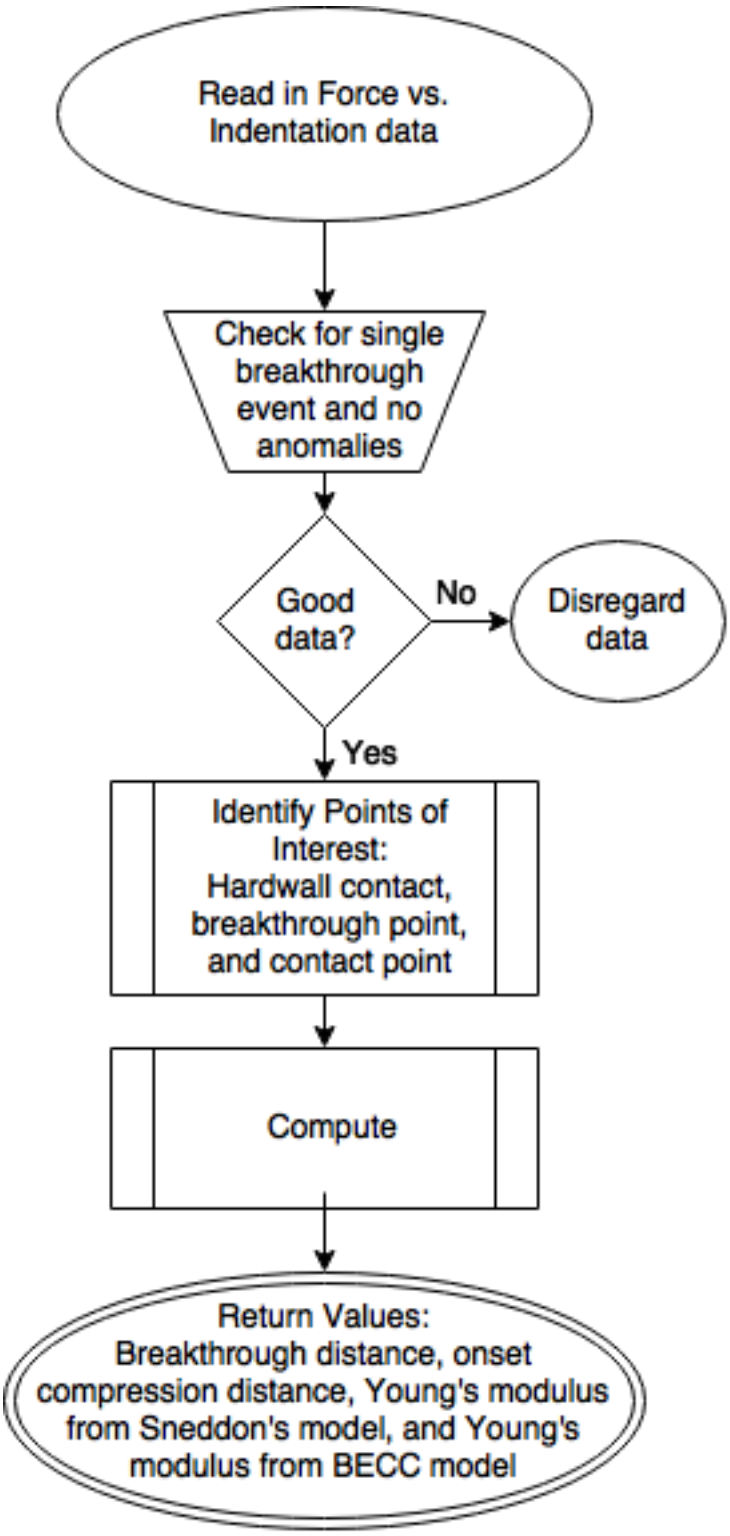

Figure 3 — Modulus Calculation Flow Chart*Raman Spectroscopy*

Raman spectroscopy is an important analytical technique which can be used to identify low-frequency energy modes in a system, such as vibrational and rotational modes, which can be used for chemical identification. Photon-induced inelastic scattering, the phenomenon at the heart of this technique, was first observed by C.V. Raman and K.S. Krishnan and published in a letter to Nature in 1928[22,23]. News of the discovery was incredibly influential, and the scientific community adopted the terms "Raman scattering" and "Raman Effect" for the phenomenon, and Raman was awarded the Nobel Prize in physics in 1930. In the following decades, thousands of chemical compounds were studied in experiments utilizing the Raman Effect. The invention of lasers, and their subsequent application to Raman spectroscopy systems 1962[24], led to a resurgence of Raman spectroscopy and its development into the broadly available analysis technique it is today.

Principles of Raman Spectroscopy

When light impinges on a material, much of it is either transmitted or reflected. A fraction of it, however, is scattered due to interactions with the medium. Of this scattered light, the majority of it is elastically scattered through Thomson scattering and Rayleigh scattering, but a very small fraction is scattered through inelastic processes, which will be discussed here.

If an incident photon is absorbed by the medium and an electron is excited to an excited state, this electron may then relax and recombine with the newly formed hole thereby emitting another photon which may have a new wave vector and energy due to non-radiative energy transitions during the fluorescence lifetime (on the order of several nanoseconds). This process is known as fluorescence (See **Figure 4**).

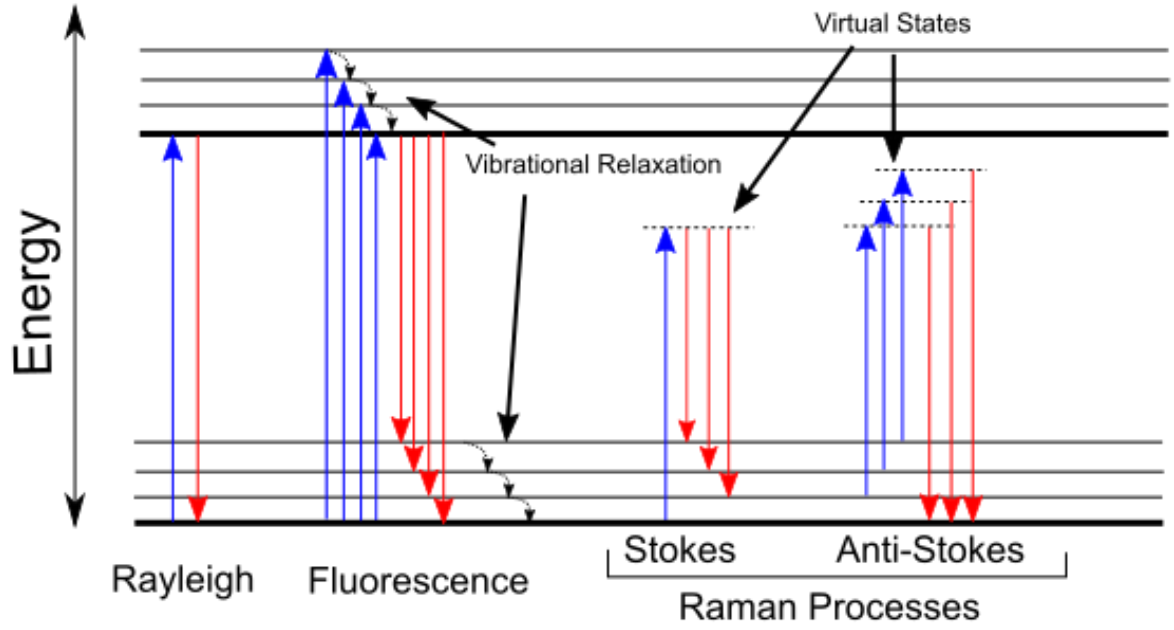

Figure 4 — Jablonski Diagram illustrating energy levels in scattering processes: Incoming electromagnetic radiation (blue) is absorbed by a material in scattering processes. An elastic process such as Rayleigh Scattering causes an electron in a material to excite to a real energy state and then re-emit a photon with equal energy. In fluorescence, there are a large number of possible paths the electron can take due to vibrational relaxation. Raman processes see the system excited to a short-lived virtual state before relaxing again. If the electron begins in the ground state this process is known as Stokes scattering, and if it begins in an excited state it is known as Anti-Stokes scattering.

The electric field of the incident radiation can also cause an oscillation in the polarization of the material, and this causes an excitation to a virtual state. These virtual energy levels are very short-lived, which removes the chance for non-radiative energy transitions while the system is excited. As a result, the energy of the photon emitted when the system relaxes gives more quantitative information about the energy levels of a system. We may consider **Figure 4** to understand this. During fluorescence, the frequency shift between incoming and outgoing photons may take on any number of values in general because the fluorescence lifetime is long enough for non-radiative transitions (i.e. vibrational relaxation) to take place. Additionally, the

system may relax into a vibrationally excited state rather than the ground state, meaning that the frequency shift of the outgoing photon is dependent on more than one phenomenon. Conversely, the systems that are excited to virtual states almost immediately relax, making frequency shifts in these cases solely the result of interactions with vibrational modes. This type of scattering involving excitation to virtual energy levels is known as Raman Scattering or the Raman Effect, and it is this ability to probe the vibrational modes of a sample by observing scattered light that has made the Raman effect such an important tool in materials characterization.

To better understand the Raman Effect in terms of polarization, we may consider an infinite crystalline medium at finite temperature with normal vibrational modes and follow a modified version of the derivation given in *Confocal Raman Microscopy* (2011). The crystal's polarization $\boldsymbol{P}(\boldsymbol{r},t)$ is given by

$$\boldsymbol{P}(\boldsymbol{r},t) = \epsilon_0 \,\hat{\chi}\, \boldsymbol{E}(\boldsymbol{r},t), \tag{5}$$

where $\boldsymbol{E}(\boldsymbol{r},t)$ is the electric field at position $\boldsymbol{r}$ and time t due to the incident light, and $\hat{\chi}$ is the susceptibility of the medium. If atomic displacements are much smaller than the crystal's lattice parameter, we may consider the first order Taylor expansion of this expression with respect to the displacement field $X(\boldsymbol{r},t)$ with

$$\hat{\chi} \approx \hat{\chi}_0 + \left(\frac{\partial \hat{\chi}}{\partial X}\right)_{X=0} X(\boldsymbol{r},t) \tag{6}$$

and

$$X(\boldsymbol{r},t) = \sum_{\boldsymbol{q}} [X(\boldsymbol{q},\omega_{\boldsymbol{q}}) e^{i(\boldsymbol{q}\cdot\boldsymbol{r}-\omega_{\boldsymbol{q}}t)} + X^*(\boldsymbol{q},\omega_{\boldsymbol{q}}) e^{-i(\boldsymbol{q}\cdot\boldsymbol{r}-\omega_{\boldsymbol{q}}t)}] \tag{7}$$

where the sum describes all random motions of the crystal with wave vectors **q** and characteristic frequencies $\omega_{\boldsymbol{q}}$. Now, if we consider the explicit expression for the electric field due to the incident light

$$\boldsymbol{E}(\boldsymbol{r},t) = \boldsymbol{E}e^{i(\boldsymbol{k}\cdot\boldsymbol{r}-\omega\, t)} + \boldsymbol{E}^{*}e^{-i(\boldsymbol{k}\cdot\boldsymbol{r}-\omega\, t)}, \tag{8}$$

we may combine these expressions and reduce the sum to a representative mode **q** to obtain:

$$\begin{aligned}\boldsymbol{P}(\boldsymbol{r},t) = {} & \epsilon_0\,\hat{\chi}_0\left(\boldsymbol{E}e^{i(\boldsymbol{k}\cdot\boldsymbol{r}-\omega\, t)} + \boldsymbol{E}^{*}e^{-i(\boldsymbol{k}\cdot\boldsymbol{r}-\omega\, t)}\right) \\ & + \epsilon_0\left(\frac{\partial\hat{\chi}}{\partial X}\right)_{X=0}\Big[X\left(\boldsymbol{q},\omega_{\boldsymbol{q}}\right)\boldsymbol{E}\,e^{i\left((\boldsymbol{k}+\boldsymbol{q})\cdot\boldsymbol{r}-(\omega+\omega_{\boldsymbol{q}})t\right)} \\ & + X^{*}\left(\boldsymbol{q},\omega_{\boldsymbol{q}}\right)\boldsymbol{E}^{*}\,e^{-i\left((\boldsymbol{k}+\boldsymbol{q})\cdot\boldsymbol{r}-(\omega+\omega_{\boldsymbol{q}})\,t\right)}\Big] \\ & + \epsilon_0\left(\frac{\partial\hat{\chi}}{\partial X}\right)_{X=0}\Big[X^{*}\left(\boldsymbol{q},\omega_{\boldsymbol{q}}\right)\boldsymbol{E}\,e^{i\left((\boldsymbol{k}-\boldsymbol{q})\cdot\boldsymbol{r}-(\omega-\omega_{\boldsymbol{q}})t\right)} \\ & + X\left(\boldsymbol{q},\omega_{\boldsymbol{q}}\right)\boldsymbol{E}^{*}\,e^{-i\left((\boldsymbol{k}-\boldsymbol{q})\cdot\boldsymbol{r}-(\omega-\omega_{\boldsymbol{q}})\,t\right)}\Big].\end{aligned} \tag{9}$$

This expression is at the heart of light scattering. The polarization of a material by a time-dependent electric field causes secondary emission in the form of photons. The first term in the polarization has a frequency ω; identical to the frequency of the incoming light. Photons emitted due to this component of the polarization are thus elastically scattered, and this process is known as Rayleigh scattering. The other two terms in the polarization are offset in frequency from the incoming light, and therefore contribute to the inelastic scattering signal. The $\omega - \omega_{\boldsymbol{q}}$ term emits a photon of lower energy than the incident light in a process called Stokes scattering. Likewise, the $\omega + \omega_{\boldsymbol{q}}$ term emits a photon of higher energy than the incident light in the Anti-Stokes scattering process.

Stokes and Anti-Stokes scattering processes are mediated by phonons, the quanta which describe lattice vibrations. Both momentum and energy must be conserved, so in a one phonon scattering process, the phonon (with wave vector **q**) can have a total wave vector magnitude no

greater than $2|\boldsymbol{k}|$. Moreover, in a Raman spectroscopy experiment, the excitation source is typically chosen to have an energy in the visible range, making its wave number ($2\pi/\lambda$) much smaller than the typical phonon wave number (on the order of $2\pi/a$, where a is the lattice constant). The condition $|\boldsymbol{q}| < 2|\boldsymbol{k}|$ therefore confines the phonon modes to those with very small wave numbers, leading to the common approximation $\boldsymbol{q} \approx 0$, sometimes referred to as the fundamental selection rule. Single-phonon scattering is therefore sensitive to the Γ-point phonon modes of a crystal. It should be noted that this wave vector limitation does not apply to individual phonons in multi-phonon processes since it is the net sum of phonon wave vectors that must satisfy conservation rules. In fact, one of the most prominent Raman processes that occurs in graphene-based systems, known as the 2D peak, relies on a multi-phonon process mediated by K-point phonons. This will be discussed in detail in a following section.

Most Raman spectroscopy experiments observe Stokes scattering events, since they can be produced from electrons initially in the ground state, but Anti-Stokes scattering is also used in some experimental apparatus. Anti-Stokes events require a system to be in an excited state prior to excitation by the photon, and as such the number of scattering events is dependent on sample temperature. These events are also much less frequent than their Stokes counterparts, necessitating specialized equipment that will not be discussed here.

The Raman Spectroscopy Experiment

In a Raman spectroscopy experiment, a sample is illuminated with a monochromatic light source and then the intensity of inelastically scattered light as a function of energy is measured. A simplified experimental apparatus is shown in **Figure 5**. Here, a monochromatic laser is directed toward a dichroic filter which reflects the light toward the sample. Scattered and reflected light from the sample then travels back toward the filter, which reflects light that is near

the laser's frequency and transmits light of other frequencies. This effectively filters out the elastic signal. The transmitted light is then focused into a monochromator and then a CCD detector to measure the scattered intensity as a function of energy.

Raman spectra are typically plotted as intensity versus "Raman shift", which is the difference in energy between the incident light and the scattered light. Raman shift is usually measured in cm^{-1}. Various bonding configurations show distinct "Raman peaks" with particular peak locations and peak shapes that allow for the identification of these bonds in a sample. For an example of a Raman spectrum, see the next section.

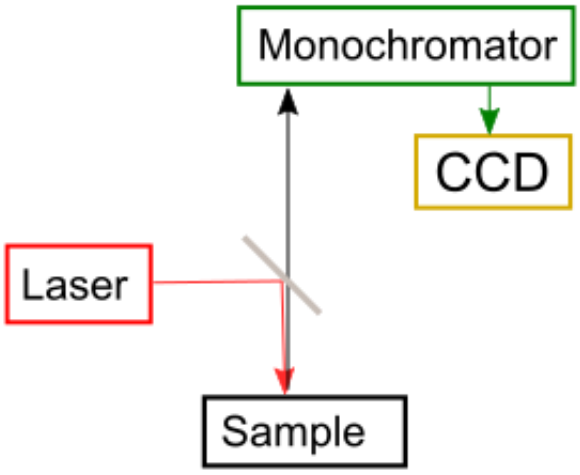

Figure 5 — Simplified diagram of a Raman spectrometer

Raman Spectrum of Graphene

Pristine monolayer graphene has two main features in its Raman spectrum; the G peak at ~1580 cm^{-1} and the 2D peak at ~2680 cm^{-1}. A typical spectrum for monolayer graphene is shown in **Figure 6**. We see a large intensity ratio I_{2D}/I_G and a sharp 2D peak with a FWHM less than 30 cm^{-1}, both of which are typical of monolayer graphene. We also see smaller peaks at ~1350 cm^{-1} (associated with lattice defects) and at 2450 cm^{-1} (an overtone peak due to LO phonons[25]). To

understand the origin of these peaks, we must consider the pathways that an excited electron can take to contribute to each peak.

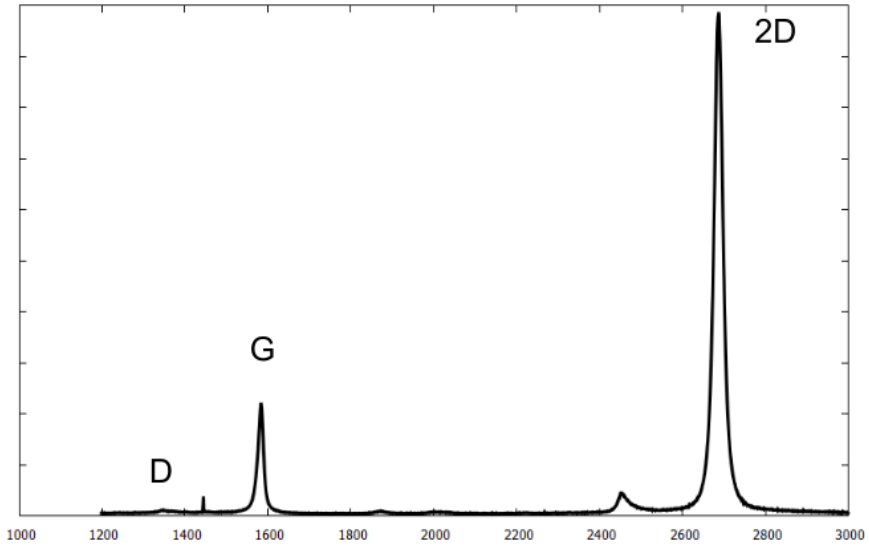

Figure 6 — Typical Raman Spectrum of monolayer graphene

First, consider the G peak. This peak is due to a one-phonon scattering process, where an incident photon is absorbed, exciting the system to a virtual state $|\alpha\rangle$ and creating an electron/hole pair. The electron then loses some energy creating a Γ-point optical phonon and bringing the system to a new virtual state $|\beta\rangle$. Finally, the electron recombines with the hole, emitting a photon with frequency ν_s. The continuous nature of the electronic dispersion of graphene allows for a continuum of different excitations to contribute to it, depending on the initial energy of the excited electron (See **Figure 7**(a)). There are both off-resonant and resonant contributions that all add to the total signal, and destructive quantum interference between the different pathways causes partial destructive interference[26]. This interference can be reduced by modulating the occupation of electronic states in graphene via doping[27,28], making the G peak an important tool in measuring graphene pristineness.

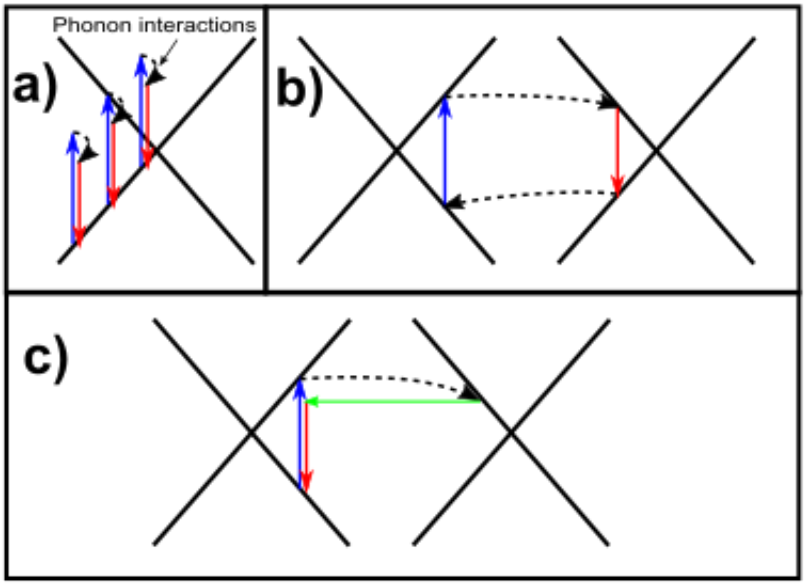

Figure 7 — Energy level diagrams of main Raman peaks in graphene: Energy level diagrams are superposed onto electronic dispersion diagrams of graphene near the Dirac point, illustrating incident photon absorption (blue), phonon interactions (dotted), and emitted photons (red). (a) Several contributions to the G band showing that both resonant and non-resonant contributions may occur. (b) An example process that contributes to the 2D peak, known as intervalley scattering. (c) An example process that contributes to the D peak which involves interaction with a photon and the elastic backscattering of the excited electron off of a defect (green).

The 2D peak is due to a multi-phonon event, and is a second-order triple-resonant process[29,30]. An example of a contribution to the 2D peak is illustrated in **Figure 7**(b). First, the incident photon is absorbed, exciting the system to a virtual state $|\alpha\rangle$, which is resonant with graphene's electronic dispersion. The electron then interacts with a transverse optical phonon with wave vector $\mathbf{q}$ near the K-point, shifting the electron to state $|\beta\rangle$ in another Dirac cone during a second resonant process referred to as intervalley scattering. The electron then relaxes to a third resonant virtual state $|\gamma\rangle$, emitting a photon in the process. Finally, the electron recombines with the hole by interacting with a second phonon with wave vector $-\boldsymbol{q}$. The probability of this process is enhanced not only by its triple-resonance, but also by the existence

of a Kohn anomaly in graphene near the K-point which leads to a large slope in the phonon dispersion and therefore also leads to enhanced electron-phonon coupling[31].

These two peaks, G and 2D, are together a very important tool for the qualitative interpretation of Raman spectra of graphene systems, especially in determining the number of graphene layers. Since the G peak is mediated solely by Γ-point phonons that correspond to $C-C$ bond-stretching, the G peak intensity simply increases as the number of graphene layers is increased. The 2D peak, however, is more sensitive to graphene's electronic dispersion near the K-point. To illustrate, we may consider AB-stacked bilayer graphene[32]. Near the K-point, bilayer graphene's band structure resembles that of monolayer graphene except that the conduction and valence bands are split due to interlayer coupling. Because of this, the pathway shown in **Figure 7**(b) can now occur in four different ways, with four distinct emitted photon energies since the states $|\alpha\rangle$ and $|\beta\rangle$ can be in either of the two conduction bands[33]. The result is that the 2D peak is divided into four Lorentzian contributions, reducing the total intensity. This phenomenon is why the intensity ratio I_{2D}/I_G is frequently used as a semi-quantitative method for identifying the number of graphene layers in a system[26,33,34]. It should be noted, however, that phenomena such as inhomogeneous self-doping[31] can cause sizeable variations in the intensity ratio even in monolayer graphene, making this metric alone insufficient to distinguish graphene systems.

Quantification of Raman spectra of graphene systems requires an in-depth analysis of not just peak intensities, but also peak shapes. The transition from monolayer graphene's single Lorentzian 2D peak with a small FWHM to the broader, four-component AB-stacked bilayer peak demonstrates just one way in which the line shape gives information about the graphene system. Highly oriented pyrolytic graphite (HOPG) exhibits a Raman spectrum reminiscent of

monolayer graphene except with a very pronounced G peak and a distinct "shoulder" on the 2D peak due to the large degree of band splitting. A number of groups have mapped out the transition in Raman spectra from monolayer graphene to few-layer graphene all the way to HOPG[35,36], but interlayer interactions also play a large role in determining line shape. For instance, turbostratic graphite (graphite with rotational misalignment, and therefore weak interlayer coupling) is characterized by a Lorentzian 2D peak with a FWHM that is approximately double that of monolayer graphene, and by a peak location that is blue-shifted by approximately 20 cm^{-1}([37,38]). Twisted bilayer graphene is also characterized by a single Lorentzian 2D peak[26], indicating that the 2D peak shape is an indicator of the interlayer coupling of a graphene system. With careful analysis of the 2D peak, one may therefore extract information about stacking order[33] and angular misorientation[39] between layers.

Raman spectroscopy is also sensitive to intralayer behavior of graphene. The most important example of this is the D peak, often referred to as the "defect peak". **Figure 7**(c) shows schematically the interactions that occur in this process, and we see initially that it begins identically to the process responsible for the 2D peak. Indeed, the 2D peak is the first overtone of the D peak; a second order process rather than a first order one. However, the D peak is forbidden in pristine graphene because of momentum conservation. The first-order (single phonon) process can proceed to state $|\gamma\rangle$, but then the electron cannot recombine with the hole since there is a K-space mismatch between the two and no second phonon to mediate the transition. In the presence of a defect, however, phonon backscattering allows for momentum conservation and makes the D peak process possible[40]. The D peak intensity has been used to gauge the defect density in graphene samples[31,41]. Graphene grain boundaries and edges can also permit backscattering, and the D peak can therefore be used to gauge grain size[26,42].

X-Ray Photoelectron Spectroscopy

X-ray photoelectron spectroscopy (XPS), also known as electron spectroscopy for chemical analysis (ESCA), is a widely used technique for chemical analysis at solid surfaces. In this dissertation, XPS is used to analyze the chemical composition and bonding configuration of experimental surfaces, so a brief introduction to the fundamentals of this technique is given here.

Principles

The photoelectric effect, the process wherein electrons are emitted when light is shone on a material, is the fundamental principle behind XPS. To a first approximation, photoemission caused by a photon with frequency υ can be understood with the following equation:

$$E_B = h\upsilon - K - \phi, \qquad 10$$

where E_B is the binding energy of the emitted electron prior to emission, K is the kinetic energy of the ejected electron, and ϕ is the work function. An XPS analyzer measures the kinetic energy of photoelectrons, so an instrument with a monochromatic light source can effectively measure the binding energy of each of the photoelectrons coming off of a sample.

Incident photons with energies in the X-ray regime (>100 eV) are sufficiently energetic to eject core electrons from atoms. Since core electron configurations are unique for each element, analysis of the photoelectron energies gives quantitative information about the elemental composition of a sample. For example, Figure [XPS SURVEY] shows a survey scan (a wide energy range scan) of a Ni film. [important peaks discussion, elemental analysis].

Chemical Shift

One of the most important qualities of XPS is its ability to discern differences in the bonding environment of the sample under investigation. To illustrate this, consider the binding energy of the 1s electrons in the core of Li metal versus its oxide form, Li_2O [Cite Hufner]. The wavefunctions of the 2s electrons in Li metal are delocalized, and this negatively charged electron cloud serves to partially mask the positively charged Li nuclei. However, in Li_2O the 2s electrons are donated to fill the 2p shell of the O atoms, and the resulting electronic wavefunction is entirely removed from the Li nuclei. As a result, the nuclear charge of Li atoms in Li_2O is not masked by these 2s electrons, increasing the binding energy. [cite values for xps peaks in the two cases]. This simple example demonstrates the power of XPS not only to perform elemental analysis of a surface but also to quantitatively assess its bonding configuration.

Other Features

In this dissertation, elemental analysis and chemical shift are the most important features of XPS spectra, but there are additional features worth mentioning. Spin-orbit coupling in p, d, and f orbitals leads to these main lines being split into multiplets. Transition metal ion compounds, due to different screening channels and exchange splitting, can have satellite lines. Secondary electrons emitted when a valence electron falls into a core hole can also be detected (Auger peaks). On top of these features and others, there is also an inelastic background due to other material interactions. The wide array of different features that show up in XPS spectra necessitate careful interpretation of experimental data.

Scanning tunneling microscopy and spectroscopy

This section will give a brief overview of STM and STS, beginning with a brief overview of the theory of operation, followed by a discussion of their use in the characterization of atomic-scale topographical and electronic features.

Fundamentals of STM – Bardeen's Formalism

Since its first presentation in 1982 by Binnig and Rohrer[43], scanning tunneling microscopy (STM) has become a ubiquitous tool in the field of surface science. The STM takes advantage of the phenomenon of quantum tunneling by creating a tunnel junction between an atomically sharp probe tip and a conductive sample. With a sufficiently small tip-sample separation, the electronic wavefunction of the tip overlaps with that of the sample, leading to tunneling current when a bias voltage V_0 is applied. To understand this tunneling mechanism in more detail, it is helpful to adopt the formalism introduced by Bardeen[44]. Here, we will consider a 1-dimensional tunnel junction, though this formalism can be expanded to three dimensions as well.

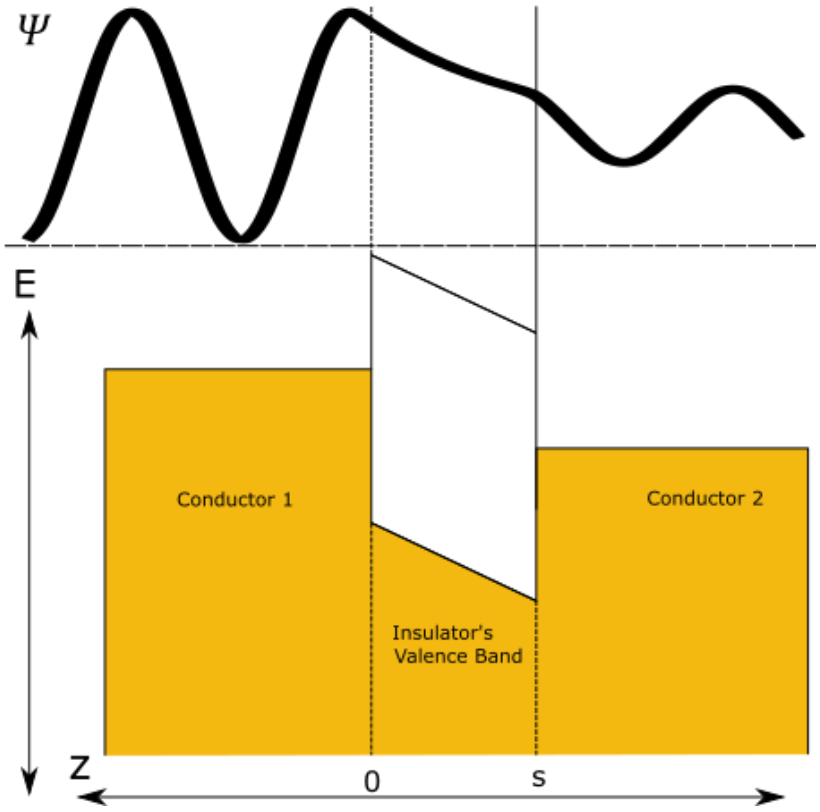

Figure 8 — Potential energy diagram for a one-dimensional tunnel junction: A bias has been applied between conductor 1 and conductor 2, causing a difference in Fermi energies. The wave function of an electron in conductor 1 is shown above the energy diagram. There is an exponential decrease in probability amplitude in the insulating barrier.

Consider a one-dimensional system consisting of two semi-infinite conductors separated by an insulating gap of width s, as depicted in **Figure 8**. We know that the electronic wavefunction for each conductor decays to zero outside of the conductor, so Bardeen introduced the following *ansatz* for the quasiparticle wavefunctions in the barrier:

$$\phi_L = a\, e^{-\chi \cdot z} \qquad z \geq 0 \tag{11}$$

$$\phi_R = e^{-\chi \cdot z} \qquad z \leq s,$$

where ϕ_L and ϕ_R are the electronic wavefunctions for the left and right conductors respectively, and χ is $\sqrt{2m(V_0 - E)}/\hbar$. If we consider an electron in the left electrode, we may write its time-dependent wavefunction as

$$\Psi(t) = c(t)\,\phi_L e^{-i\,E_L\,t/\hbar} + d(t)\,\phi_R\,E e^{-i\,E_R\,t/\hbar}, \qquad 12$$

Where c(t) and d(t) are the matrix elements corresponding to the electron being in the left and right electrodes. We may then substitute into the time-dependent Schrodinger equation, giving us

$$\widehat{H}\,\Psi(t) = i\,\hbar\,\frac{d}{dt}\Psi(t) \qquad 13$$

$$= i\,\hbar\left(\dot{c}(t)\phi_L e^{-i\,E_L\frac{t}{\hbar}} + \dot{d}(t)\phi_R\,e^{-i\,E_R\frac{t}{\hbar}}\right)$$

$$+ E_L c(t)\phi_L e^{-i\,E_L\frac{t}{\hbar}}$$

$$+ E_R\,d(t)\phi_R\,E e^{-i\,E_R\frac{t}{\hbar}}.$$

The electron originated in the left electrode, so in the limit of large barrier heights we may assume that there is a low chance of tunneling, and therefore $c(t) \cong 1$, $\dot{c}(t) \cong 0$ and $d(t) \cong 0$. This simplifies this equation to

$$\widehat{H}\,\Psi(t) = i\,\hbar\,\dot{d}(t)\phi_R\,e^{-i\,E_R\frac{t}{\hbar}} + E_L c(t)\phi_L e^{-i\,E_L\frac{t}{\hbar}}. \qquad 14$$

We now assume that the tunneling process is elastic (*i.e.* $E_L = E_R$). We can now define an operator $\widehat{H}_T = \widehat{H} - E_L = \widehat{H} - E_R$, which is known as the transfer Hamiltonian. With some rearrangement, Equation 14 now reads as

$$\widehat{H}_T\phi_L e^{-i\,E_L\frac{t}{\hbar}} = i\,\hbar\,\dot{d}(t)\phi_R\,E e^{-i\,E_R\frac{t}{\hbar}}. \qquad 15$$

And so,

$$\widehat{H}_T\phi_L = i\,\hbar\,\dot{d}(t)\phi_R\ . \qquad 16$$

And performing an inner product with ϕ_R^* on both sides of Equation 16 gives

$$\langle \phi_R^* | \hat{H}_T | \phi_L \rangle = i\,\hbar\,\dot{d}(t). \quad (17)$$

The integral $M_{TS} = \langle \phi_R^* | \hat{H}_T | \phi_L \rangle$ is known as the tunneling matrix element, and it describes the coupling between tip and sample. This expression is generalizable to three dimensions, and we will now change notation from right- and left-electrodes ("R" and "L") to tip and sample ("T" and "S"). We see from Equation 17 that M_{TS} is related to the tunneling probability, but we may use Fermi's Golden Rule to gain a more intuitive interpretation of M_{TS}. This rule gives the probability per unit time for an electron in the left electrode to tunnel across the gap as

$$w = \frac{2\pi}{\hbar}\,|M_{TS}|^2 \delta(E_S - E_T). \quad (18)$$

Using this expression and factoring in the density of states for the tip and sample, we can write expressions for the total current passing between tip and sample when a bias V is applied across the two electrodes:

$$I_{T\to S} = \frac{2\pi e}{\hbar}\int |M_{TS}|^2\, n_T(E - eV) n_S(E) f_T(E - eV)\big(1 - f_S(E)\big)dE, \quad (19)$$

$$I_{S\to T} = \frac{2\pi e}{\hbar}\int |M_{TS}|^2\, n_T(E - eV) n_S(E) f_S(E)\big(1 - f_T(E - eV)\big)dE, \quad (20)$$

$$I = I_{T\to S} - I_{S\to T} = \frac{2\pi e}{\hbar}\int |M_{TS}|^2\, n_T(E - eV) n_S(E)\big(f_T(E - eV) - f_S(E)\big)dE, \quad (21)$$

Where I is the net current and f_T and f_S are Fermi-Dirac distributions describing the occupancy of electronic states in the two electrodes. For temperatures satisfying kT ≪ eV, this expression becomes

$$I_{(kT \ll eV)} \propto \int_{E_F}^{E_F + eV} |M_{TS}|^2\; n_T(E - eV) n_S(E) dE. \quad (22)$$

This expression can be used to understand the fundamental operation of a STM. Consider the limit of low bias voltage V with respect to the sample's work function (*i.e.* eV << E_F), and

assume that the probe tip terminates with a metallic s-orbital. In this case, Equation 22 simplifies to[45]

$$I \propto V\, n_T(E_F - eV, \boldsymbol{R}_{T\,Center})\, n_S(E_F), \qquad 23$$

Where the tip's density of states n_T is evaluated at the center of curvature of the tip. From Equations 11, we approximate the electronic wavefunction of the sample, and hence the sample's density of states decays in the gap exponentially, giving us

$$I \propto e^{-2\chi z}, \qquad 24$$

This exponential behavior makes tunneling current extremely sensitive to changes in tip-sample separation. STMs utilize this phenomenon to map out variations in surface topography. The STM work presented in this dissertation utilizes the constant-current mode of operation for topography measurements, wherein the tunneling current is fed into a feedback loop controlling the z-position of a probe tip. In this setup, we record the voltage applied to the z-position piezoelectric actuator to maintain constant current as the tip is raster-scanned across a scan area consisting of a grid of points. The resultant array is interpreted as a map of the nanoscale topography of the sample's surface within the scan area.

Theory of Scanning Tunneling Spectroscopy

In addition to topography measurements, STM can be used to measure the electronic structure of nanoscale surfaces. If we look back at Equation 23, we see that tunneling current is sensitive to local variations in the sample's electronic density of states. To elucidate the precise nature of these density of states measurements, consider the derivative of Equation 22 with respect to bias voltage V:

$$\frac{dI}{dV} \propto |M_{TS}|^2 n_T(E_F) n_S(E_F - eV) + \qquad 25$$

$$\int_{E_F}^{E_F+eV}\left(\frac{\partial}{\partial V}|M_{TS}|^2\right)n_T(E-eV)n_S(E)dE +$$

$$\int_{E_F}^{E_F+eV}|M_{TS}|^2\left(\frac{\partial}{\partial V}n_T(E-eV)\right)n_S(E)dE$$

In the limit of low bias voltage V, the first term is much larger than the other terms. If the tip-sample separation is constant (which can be achieved by utilizing the constant-current feedback loop discussed in the previous section), the tunneling matrix element is approximately constant. With these approximations in mind, the differential conductance becomes,

$$\frac{dI}{dV} \propto n_S(E_F - eV) \qquad 26$$

We find a simple proportionality rule relating the differential conductance to the sample's density of states near the Fermi level. This measurement can be obtained by sweeping the bias voltage across a range of values, recording the tunneling current, and differentiating the resultant curve. Despite the many approximations used to obtain this expression, the general relation between differential conductance and sample density of states remains a good qualitative way to probe the density of states of non-insulating surfaces.

Additional Characterization Methods

This section outlines some additional methods that are referenced in the following chapters. Brief descriptions are given for scanning electron microscopy and the Brunauer-Emmett-Teller method for analysis of gas adsorption data.

Scanning Electron Microscopy

Scanning electron microscopy (SEM) is a surface imaging method that uses a focused electron beam to map the surface topography and composition of materials. The electron beam is aimed at a sample and raster-scanned, and secondary electrons emitted by the sample surface are

sent to a detector via a series of optics and analyzed to recreate a pseudo-three-dimensional map of the surface. For example SEM images, refer to **CHAPTER VI: Synthesis of Bijel-Templated 3-Dimensional Multi-layer Graphene**.

Determination of Surface Area by the Brunauer-Emmett-Teller Method

Brunauer-Emmett-Teller (BET) theory[46] describes the physisorption of gas molecules on solids, and although it was invented in 1938 and makes a number of broad assumptions, BET theory remains one of the most frequently used models for gas adsorption mechanics. Use of the BET method for interpreting N_2 adsorption isotherms has become a standard protocol for assessing the surface area of highly porous media[47]. To perform BET surface area measurements, a sample is first put in a vacuum system and ambient air is removed. A gas (often N_2) is then leaked into the vacuum system and the amount of adsorbed gas is measured as a function of gas pressure. By using BET theory to analyze this data allows for the calculation of the total accessible surface area.

References

[1] T. R. Albrecht, P. Grütter, D. Horne, D. Rugar, *J. Appl. Phys.* **1991**, *69*, 668.

[2] G. Cohen, E. Halpern, S. U. Nanayakkara, J. M. Luther, C. Held, R. Bennewitz, A. Boag, Y. Rosenwaks, *Nanotechnology* **2013**, *24*, 295702.

[3] R. Baier, C. Leendertz, M. C. Lux-Steiner, S. Sadewasser, *Phys. Rev. B* **2012**, *85*, DOI 10.1103/PhysRevB.85.165436.

[4] S. Sadewasser, C. Leendertz, F. Streicher, M. C. Lux-Steiner, *Nanotechnology* **2009**, *20*, 505503.

[5] J. Colchero, A. Gil, A. M. Baró, *Phys. Rev. B* **2001**, *64*, 245403.

[6] H. O. Jacobs, P. Leuchtmann, O. J. Homan, A. Stemmer, *J. Appl. Phys.* **1998**, *84*, 1168.

[7] C. Leendertz, F. Streicher, M. C. Lux-Steiner, S. Sadewasser, *Appl. Phys. Lett.* **2006**, *89*, 113120.

[8] A. Masago, M. Tsukada, M. Shimizu, *Phys. Rev. B* **2010**, *82*, 195433.

[9] S. Belaidi, F. Lebon, P. Girard, G. Leveque, S. Pagano, *Appl. Phys. A* **1998**, *66*, S239.

[10] R. Baier, C. Leendertz, M. C. Lux-Steiner, S. Sadewasser, *Phys. Rev. B* **2012**, *85*, DOI 10.1103/Physrevb.85.165436.

[11] S. S. Schmidt, D. Abou-Ras, S. Sadewasser, W. Yin, C. Feng, Y. Yan, *Phys. Rev. Lett.* **2012**, *109*, 095506.

[12] W. F. Heinz, J. H. Hoh, *Trends Biotechnol.* **1999**, *17*, 143.

[13] H.-J. Butt, E. K. Wolff, S. A. C. Gould, B. Dixon Northern, C. M. Peterson, P. K. Hansma, *J. Struct. Biol.* **1990**, *105*, 54.

[14] A. Calò, D. Reguera, G. Oncins, M.-A. Persuy, G. Sanz, S. Lobasso, A. Corcelli, E. Pajot-Augy, G. Gomila, *Nanoscale* **2014**, *6*, 2275.

[15] M. Lekka, P. Laidler, D. Gil, J. Lekki, Z. Stachura, A. Z. Hrynkiewicz, *Eur. Biophys. J.* **1999**, *28*, 312.

[16] M. Lekka, K. Pogoda, J. Gostek, O. Klymenko, S. Prauzner-Bechcicki, J. Wiltowska-Zuber, J. Jaczewska, J. Lekki, Z. Stachura, *Micron* **2012**, *43*, 1259.

[17] M. Prabhune, G. Belge, A. Dotzauer, J. Bullerdiek, M. Radmacher, *Micron* **2012**, *43*, 1267.

[18] A. Alessandrini, P. Facci, *Micron* **2012**, *43*, 1212.

[19] S. Li, F. Eghiaian, C. Sieben, A. Herrmann, I. A. T. Schaap, *Biophys. J.* **2011**, *100*, 637.

[20] I. N. Sneddon, *Int. J. Eng. Sci.* **1965**, *3*, 47.

[21] E. K. Dimitriadis, F. Horkay, J. Maresca, B. Kachar, R. S. Chadwick, *Biophys. J.* **2002**, *82*, 2798.

[22] R. S. Krishnan, R. K. Shankar, *J. Raman Spectrosc.* **1981**, *10*, 1.

[23] "A New Type of Secondary Radiation : Abstract : Nature," can be found under http://www.nature.com/nature/journal/v121/n3048/abs/121501c0.html, **n.d.**

[24] S. P. S. Porto, D. L. Wood, *J. Opt. Soc. Am.* **1962**, *52*, 251.

[25] T. Shimada, T. Sugai, C. Fantini, M. Souza, L. G. Cançado, A. Jorio, M. A. Pimenta, R. Saito, A. Grüneis, G. Dresselhaus, M. S. Dresselhaus, Y. Ohno, T. Mizutani, H. Shinohara, *Carbon* **2005**, *43*, 1049.

[26] A. C. Ferrari, D. M. Basko, *Nat. Nanotechnol.* **2013**, *8*, 235.

[27] M. Kalbac, A. Reina-Cecco, H. Farhat, J. Kong, L. Kavan, M. S. Dresselhaus, *ACS Nano* **2010**, *4*, 6055.

[28] C.-F. Chen, C.-H. Park, B. W. Boudouris, J. Horng, B. Geng, C. Girit, A. Zettl, M. F. Crommie, R. A. Segalman, S. G. Louie, F. Wang, *Nature* **2011**, *471*, 617.

[29] P. Venezuela, M. Lazzeri, F. Mauri, *Phys. Rev. B* **2011**, *84*, 035433.

[30] J. Maultzsch, S. Reich, C. Thomsen, *Phys. Rev. B* **2004**, *70*, 155403.

[31] A. C. Ferrari, *Solid State Commun.* **2007**, *143*, 47.

[32] T. Ohta, A. Bostwick, T. Seyller, K. Horn, E. Rotenberg, *Science* **2006**, *313*, 951.

[33] Y. Hao, Y. Wang, L. Wang, Z. Ni, Z. Wang, R. Wang, C. K. Koo, Z. Shen, J. T. L. Thong, *Small* **2010**, *6*, 195.

[34] D. Graf, F. Molitor, K. Ensslin, C. Stampfer, A. Jungen, C. Hierold, L. Wirtz, *Nano Lett.* **2007**, *7*, 238.

[35] L. M. Malard, M. A. Pimenta, G. Dresselhaus, M. S. Dresselhaus, *Phys. Rep.* **2009**, *473*, 51.

[36] A. C. Ferrari, J. C. Meyer, V. Scardaci, C. Casiraghi, M. Lazzeri, F. Mauri, S. Piscanec, D. Jiang, K. S. Novoselov, S. Roth, A. K. Geim, *Phys. Rev. Lett.* **2006**, *97*, 187401.

[37] A. Marchand, P. Lespade, M. Couzi, *15th Bienn. Conf Carbon* **1981**, 282.

[38] U. Mogera, R. Dhanya, R. Pujar, C. Narayana, G. U. Kulkarni, *J. Phys. Chem. Lett.* **2015**, *6*, 4437.

[39] K. Kim, S. Coh, L. Z. Tan, W. Regan, J. M. Yuk, E. Chatterjee, M. F. Crommie, M. L. Cohen, S. G. Louie, A. Zettl, *Phys. Rev. Lett.* **2012**, *108*, 246103.

[40] E. J. Heller, Y. Yang, L. Kocia, W. Chen, S. Fang, M. Borunda, E. Kaxiras, *ACS Nano* **2016**, *10*, 2803.

[41] A. Das, B. Chakraborty, A. K. Sood, *Bull. Mater. Sci.* **2008**, *31*, 579.

[42] C. Casiraghi, A. Hartschuh, H. Qian, S. Piscanec, C. Georgi, A. Fasoli, K. S. Novoselov, D. M. Basko, A. C. Ferrari, *Nano Lett.* **2009**, *9*, 1433.

[43] G. Binnig, H. Rohrer, *Helvetica Phys. Acta* **1982**, *55*, 726.

[44] J. Bardeen, *Phys. Rev. Lett.* **1961**, *6*, 57.

[45] J. Tersoff, D. R. Hamann, *Phys. Rev. B* **1985**, *31*, 805.

[46] S. Brunauer, P. H. Emmett, E. Teller, *J. Am. Chem. Soc.* **1938**, *60*, 309.

[47] D. Dollimore, P. Spooner, A. Turner, *Surf. Technol.* **1976**, *4*, 121.

CHAPTER III: Kelvin Probe Force Microscopy under an Applied Electric Field: Local Electronic Behavior of Vapor-Liquid-Solid Si Nanowires

The work presented in this chapter outlines a characterization methodology that allows for the characterization of Si nanowire systems as current is being driven through them. This can be a highly useful technique in the design of novel sensing systems, as the nanoscale potential distribution can be measured in the presence of gases which will be detected, allowing for a thorough understanding of detection mechanisms in nanowire-based sensors.

Reprinted with permission from N. J. Quitoriano, R. N. Sanderson, S.-S. Bae, R. Ragan, *Nanotechnology* **2013**, 24, 205704.

Abstract

Kelvin-probe force microscopy (KPFM) is used to characterize electrical characteristics of vapor-liquid-solid (VLS), Si Nanowires (NWs) that are grown in-place between two, predefined electrodes. KPFM measurements are performed under an applied bias. Besides contact potential differences due to differing materials, the two other primary contributions to measured variations on Si NWs between electrodes are: trapped charges at interfaces and parallel and serial capacitance that are accounted for with voltage-normalization and oxide-normalization. These two normalization processes alongside Finite-Element-Method simulations are necessary to characterize the bias-dependent response of Si NWs. After applying both normalization methods on open circuit NWs, which results in a baseline of zero, we conclude that we have accounted for all major contributions to CPDs

and we can isolate effects due to applied bias such as impurity states and charged carrier flow as well as find open connections when NWs are connected in parallel. These characterization and normalization methods can also be used to determine that the specific contact resistance of electrodes to the NWs is on the order of $\mu\Omega$ cm^2. Thus, the VLS growth method between predefined electrodes overcomes the challenge of making low-resistance contact to nanoscale systems. Thereby, the experiments and analysis presented outlines a systematic method for characterizing nanowires in parallel arrays under device operation conditions.

Introduction

Semiconductor nanowires (NWs) since the first demonstration of vapor-liquid solid (VLS) growth almost 50 years ago[1] have made remarkable progress in control of growth parameters and have received much attention in applications, for example as specialty, field-effect transistors.[2] In addition, self-assembled parallel arrays of nanowires have application in thermoelectric devices[3], complementary inverters[4] and interdigitated electrodes for electrochemical based detection in sensors.[5] Improved metrology is needed to guide synthesis of emerging research materials in the semiconductor roadmap[2] and for the many emerging low-cost applications.[3-5] Here we utilize a directed self-assembly process that allows for control of horizontal, planar growth of VLS Si NWs. The current-voltage response of these Si NWs have previously been characterized in top-gated, metal-oxide semiconductor field-effect transistors (MOSFETs)[6] and here we examine nanoscale electronic environment.

Kelvin-probe, force microscopy (KPFM) measures local electronic properties of nanoscale systems and is particularly useful for investigating local electronic behavior for

nanoscale systems connected in parallel since current-voltage measurements only probe collective behavior. KPFM is a scanning probe characterization method that measures the contact potential difference (CPD) between a sample and a probe tip and is typically conducted alongside atomic force microscopy (AFM) measurements in order to facilitate the understanding between surface structure and measured CPD. CPD is the difference between the work function of the probe tip and a conductive sample surface and is defined as:

$$CPD = \frac{\varphi_{tip} - \varphi_{sample}}{-e} = -\delta v \tag{1}$$

where e is the elementary charge, ϕ_{tip} and ϕ_{sample} are the work functions of the tip and sample, respectively, and δv is the applied external voltage. KPFM measures the electrostatic force between the probe tip and the surface to characterize the CPD. The force, due to the separation-dependant capacitance and potential between the tip and the sample,[7] is given by:

$$\mathrm{F} = -\frac{V^2}{2}\frac{\partial C}{\partial z} \tag{2}$$

where the potential, capacitance and distance between the probe tip and sample surface are V, C, and z, respectively. On the first trace, a non-contact AFM topography is acquired in our ambient system. On the retrace, acquired at constant tip-sample distance, KPFM maps the CPD between the sample surface and the probe tip by applying a small signal voltage (δv) on top of a time-varying bias (δV) at frequency ω on the tip. During KPFM, the small signal δv is varied to minimize the force between probe tip and sample surface and sampled at frequency ω. The voltage, δv, at which the minimum force is measured, is equal to the CPD between the substrate and probe tip that is measured using a lock-in technique.

The CPD can be understood by considering two materials that are electrically isolated from one another, their vacuum levels match but their Fermi energies typically do not (i.e. when the materials' work functions differ). When one electrically connects these two materials, electrons will flow from the material with a higher Fermi energy to the lower Fermi-energy material until an electric field is established to establish a constant Fermi level across the two materials thus reaching equilibrium. The CPD between the sample and the probe tip can be viewed in a number of ways. Practically, it is the potential difference required to prevent the flow of electrons between the probe tip and the sample surface to maintain equilibrium when the probe and sample are electrically connected. However, it can also be viewed as the difference between the Fermi energies of the two materials that is affected by the intrinsic Fermi energy, impurities and local surface charges.[8, 9] In the case of non-conductive surfaces and samples in ambient conditions, KPFM will also measure the surface charge between the tip and the underlying, conductive substrate.[10]

Analysis may appear straightforward, yet parallel capacitance between the sample background and local surface structure, a so-called averaging or weighting effect,[11] and serial capacitance[8] due to induced surface charge and/or passivating layers on semiconductor surfaces in device structures influence KPFM measurements, particularly on nanoscale features. These effects make the interpretation of raw KPFM images difficult. While KPFM has been used to characterize: surface defects in semiconductors,[9, 12] surface electronic structure of model bimetallic nanocatalysts,[13] as well as semiconductor nanowires (NWs),[14, 15] measurements are typically performed in ultrahigh vacuum and controlled environments. Few measurements are performed in conditions of device operation and/or on passivated material device structures.[16, 17, 18]

In addition few papers discuss KPFM measurements with an applied voltage across the material (other than the voltage between the sample and probe) to be characterized, see for

example these references.[17] [18-20] Recently, we have applied this technique to characterize local, defect states in Si NWs fabricated by etching the top, Si (device) layer of a silicon-on-insulator (SOI) substrate and compared the results with Si NWs produced using the vapor-liquid-solid (VLS), catalyzed-growth process to understand the relationship between processing conditions and surface electronic structure in device architectures.[18] Here, we use KPFM to characterize VLS, semiconductor NWs that have been grown, in-place, against a silicon dioxide surface, between two, Si electrodes with different applied voltages across them. We find that two normalization procedures are needed for data interpretation: (1) normalizing the measured CPD data across biased NWs with respect to CPD data across NWs with no bias and (2) normalizing the measured CPD data across NWs under an applied bias with respect to CPD data acquired adjacent to the NW at the same bias. The former we refer to as voltage-normalized surface potential and the latter oxide-normalized surface potential. We describe these normalization procedures and use them to estimate the contact resistance of the NWs as well as determine if the NW has made good contact with both electrodes.

Experimental Procedures

The semiconductor NW devices were made using a combination of top-down and bottom-up procedures. The Si, contact electrodes were defined and fabricated using a top-down procedure on a (001)-oriented, SOI substrate. The 100-nm-thick, n-type ($\sim 10^{19}/cm^3$ phosphorus), Si electrodes were isolated from one another by etching through the top (device-layer) Si and stopping at the underlying SiO_2. Nominally undoped, Si NWs were grown between these two electrodes by guiding the NW growth against the SiO_2 using a bottom up approach. Au colloids were deposited somewhat selectively onto the exposed Si surfaces, the underside of

the Si device layer (See the inset in **Figure 9**a). These Au particles acted as catalysts for Si NW growth and the NWs grew between the two Si contact electrodes to electrically connect them. **Figure 9** shows a schematic cross-section taken through the NW and a plan-view, scanning-electron-microscope (SEM) image. The details of the NW fabrication procedure are published elsewhere[6, 21] and these devices were essentially the same as those described in reference,[6] though without the top, metal gate deposited on the NW and with a ~ 3 nm, dry thermal oxidation process, SiO_2.

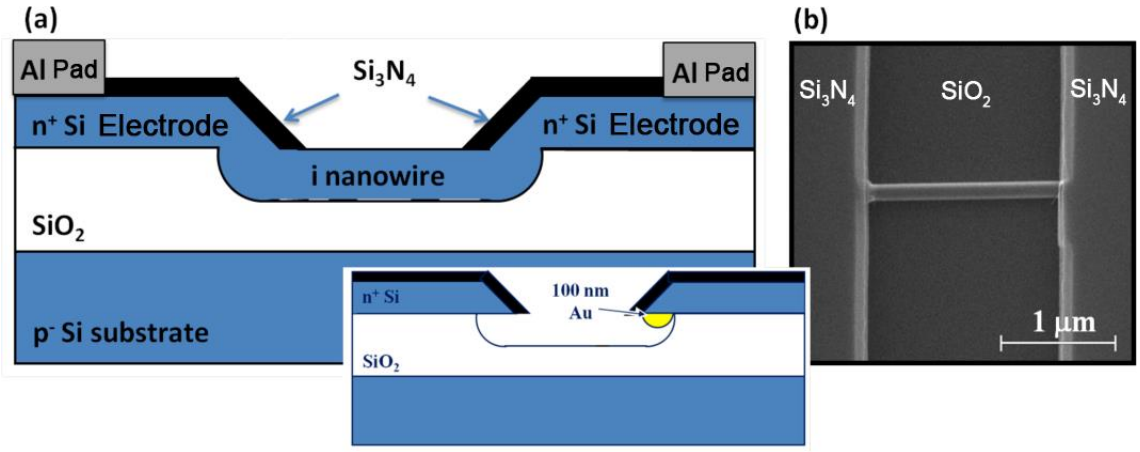

Figure 9: (a) Schematic cross section of a VLS NW grown between two electrodes taken through the NW which connects the two electrodes. (Inset) Schematic of the NW fabrication process, using Au particles to catalyze NW growth. (b) Plan-view SEM image of the two electrodes passivated with Si_3N_4 connected by a NW which was grown in between and electrically connects the two pads.

The samples were then scanned using AFM and KPFM to gather both the height and CPD information using the described two-pass technique. The samples had varying voltages across the electrodes from 0 – 1 V in 0.25 V intervals. AFM and KPFM measurements were performed using an Asylum Research AFM system, MFP-3D. The measurements were obtained in an air ambient at room temperature with a scan rate of 0.3 Hz to allow for adequate controller

response time.[22] Commercial, Si, AFM tips (Olympus AC-160TS) were coated with approximately 3 nm of Cr using an Ar sputtering system (IBS, Southbay Technology) to obtain a conducting tip for KPFM analysis. The resonance frequency of AFM tips was measured to be 310-320 kHz, and the spring constant was listed as 42 N/m. KPFM data was acquired in amplitude modulation mode. An AC voltage, δV, of 3V is applied to the tip at the first resonance of the cantilever. A lock-in technique is used to measure the applied DC voltage, δv, needed to minimize the electrostatic force between probe tip and sample surfaces that is monitored at the first resonance frequency of the cantilever oscillation.

The NW systems were modeled using Finite-Element-Method (FEM) simulations to lend understanding to the KPFM studies. The geometry of **Figure 9** was modeled and accepted values for the conductivity and permittivity were used for Si, SiO_2, and Si_3N_4. The SPM tip was modeled as a conical frustum with a semi-angle of 15º capped with a spherical tip of radius 9 nm. The simulations solved Laplace's equation $\nabla^2\varphi = 0$ and gave the electric potential distribution in 3 dimensions. The electric field was calculated using $E = -\nabla\varphi$, and the electrostatic force on the SPM tip was calculated by integrating the Maxwell stress tensor over the tip's surface area. CPD measurements were simulated by iterating for a number of tip biases, and fitting the results to find the tip bias that minimizes the z-component of the force on the SPM tip as is done in KPFM experiments to determine the CPD.

Results and Discussion

Figure 10 shows AFM (**Figure 10**a) and CPD (**Figure 10**b and **Figure 10**c with $V_{AB} = 0$ V and 1 V, respectively) images, scanned at an approximate 45° angle to capture all abrupt topographic variations, for Si NWs fabricated as depicted in Figure 1. In **Figure 10**c, electrode

B in the upper left has a lower potential than the electrode A in the lower right, this is because there is an applied bias ($V_{AB} = V_A - V_B = 1$ V) between the electrodes. As illustrated in **Figure 9**, when the NW bridges the gap between the two electrodes and a bias is placed across those two electrodes, current will flow. From **Figure 10**a and **Figure 10**b, NW1 is observed to have grown over the side of electrode A.

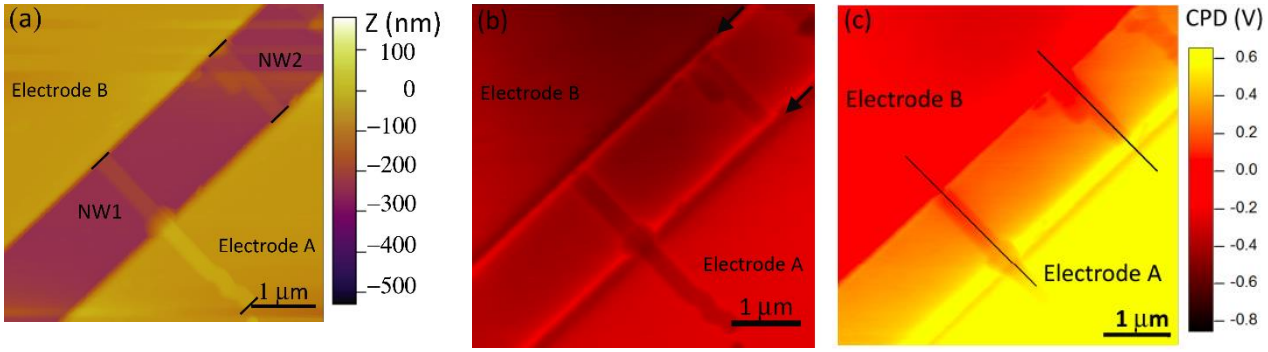

Figure 10: (Color online) (a) AFM and (b) CPD images at $V_{AB} = 0$ and (c) at $V_{AB} = 1$V of bridging NWs between electrodes A, lower right, and B, upper left. Lines in (a) highlight the ends of the NWs. Arrows in (b) point to the edge of the electrode. Electrode A is at a higher potential than electrode B in (c). The CPD voltage key for both Figures (b) and (c) is shown on the right of (c).

Line profiles were taken across the NWs between electrode A and electrode B at different voltages, V_{AB}, along the black lines indicated in **Figure 10**c. **Figure 11**a shows resulting CPD line profiles for voltages, V_{AB}, from 0 – 1 V in 0.25 V intervals for NW2. The regions on the line profiles corresponding to the NW are highlighted with arrows. As can be seen in **Figure 11**a, all of the CPD line profiles have a similar shape. For example, in **Figure 11**a, the curve corresponding to $V_{AB} = 0$ V has significant CPD variations as a function of position, related to surface charges and differing materials, etc. which are not related to an applied voltage across the NW.

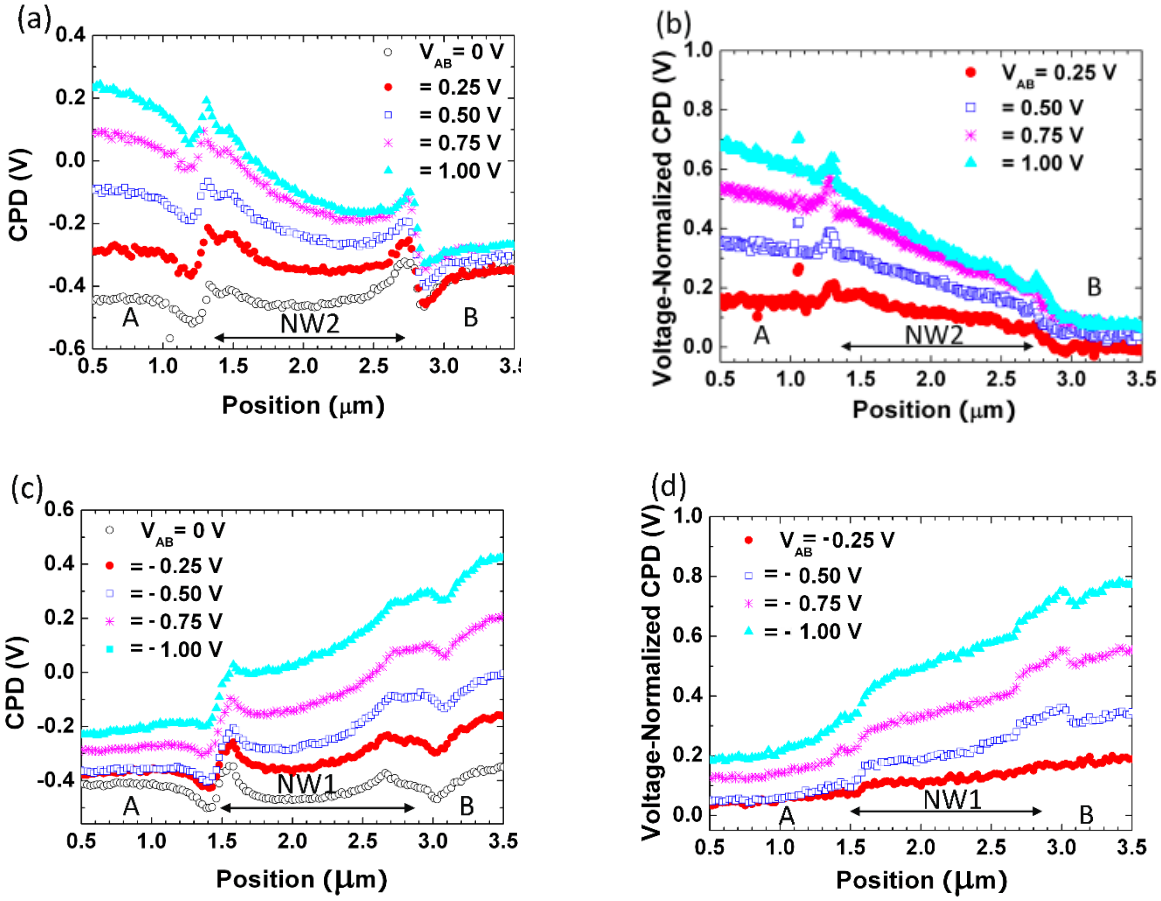

Figure 11: (color online) CPD line profiles at different applied voltages across (a) NW2 and (c) NW1 as labeled in (a). Electrode B corresponds to the electrical contact in the upper left corner of (a). (b) Voltage-normalized, CPD, line profiles obtained by subtracting the V_{AB} = 0 V line profile from the others in (a) for (b) NW2 and (d) for NW1.

One of the dominant features of all these CPD profiles is the increase in CPD values near the interfaces between the NW and the electrodes. Theses features are also observed in the line profile of NW1, shown in **Figure 11**c, with some slight variations where NW1 climbs over the side of electrode A. This CPD increase seen in the line profiles of **Figure 11**a and **Figure 11**c near the NW2/electrode A-B and NW1/electrode A interfaces could occur due to differing

doping densities,[23] occupied surface states,[24] and height variations between the NW and the electrodes.

To isolate and better understand the effect of the applied voltage on the CPD profiles, the line scan corresponding to V_{AB} = 0 V was subtracted from the other line scans, [20, 25] (V_{AB} = ±0.25, ±0.50, ±0.75 and ±1 V), and the resulting data are shown in **Figure 11**b and **Figure 11**d; we refer to this process as voltage-normalization. The line profiles are quite smooth except for some jumps in the CPD for one or two data points near the interfaces, corresponding to small misalignments in the line scan data taken across multiple scans. (Since the normalization process requires taking scans and subtracting them, anomalies can result from subtracting one from another when they are not exactly aligned.) Besides these anomalies, the voltage-normalized CPD increases nearly linearly with increasing V_{AB} with a small change in slope between NW2 and electrode B, near the 2.8 μm position and a CPD increase at the 1.3 μm position. Both of these features exhibit a small, bias dependence and have several data points associated with them thus do not represent normalization artifacts due to misalignment of data subtraction.

First we consider the linear current-voltage response along the NWs in the data of **Figure 11**b and **Figure 11**d. The linear potential drop across the NWs is 70%-80% of the applied bias; this behavior was reproducibly observed in the many measured NWs. Parallel capacitance contributions from the neighboring positive electrode is known to increase the CPD measured at the grounded electrode leading to a smaller potential drop in the applied bias.[11] The linear, current-voltage (Ohmic) response that was measured, in spite of the large differences in doping between the NW and electrodes, can be understood when considering the NW surface states.

Though the Si NWs have not been intentionally doped, positive surface charge density in between the NW and the 3 nm thermal SiO_2 on the order of $10^{12}/cm^2$, leads to an accumulation of electrons in the NW.[26] For a similar device[6] in a metal-oxide-semiconductor, field-effect transistor configuration, appreciable current was measured with a zero gate voltage, indicating that the NW is lightly n-type due to its surface states. Therefore, the near linear CPD response with applied V_{AB} is reasonable since the NW acts as a resistor with a decreased cross-section and decreased, (effective) doping density.

We now examine the CPD increases at the NW-electrode interfaces, e.g. at the 1.3 μm position in **Figure 11**a and the 1.5 μm position in **Figure 11**c. An increase in CPD would be consistent with the accumulation of positive charge at the interface that could be due to interface states at SiO_2 and Si_3N_4 junctions. It is also possible that positively-charged, surface states on Si NWs[26] would not be compensated by electrons in the undoped NWs near the depletion region; yet it would not be expected that such features would be symmetric as observed in the experimental data. The CPD increase, on the other hand, may also be associated with the tip-electrode separation. FEM simulations were utilized to lend further understanding to the results shown in **Figure 11**. The CPD increases seen near the NW2/electrode A-B and NW1/electrode A interfaces might be interpreted as measurement anomalies caused by the steep geometry of the nanowire trench ramp. AFM does not track the surface topography of a sample perfectly, and at steep topographical features the measured surface topography is distorted, causing downward slopes to become less pronounced.[27] It is thus possible that in **Figure 11** the probe tip was not properly tracking the sample surface at both ends of the SiO_2 trench, and was in fact further from the sample surface at this point relative to others. To investigate the plausibility of this explanation, FEM simulations were conducted for various tip-sample separations. The FEM

simulations used in this work modeled the KPFM tip (Olympus AC-160TS) as a sphere of radius 9 nm joined to the end of a right conical frustum, 11 microns tall, with an opening angle of 15 degrees. **Figure 12**(a) shows simulated CPD line profiles near the higher potential electrode which is held 0.50 V above the drain, which is held at ground. It is seen that an increased tip-sample separation causes a decrease in the detected CPD, rather than the increase seen in the experimental data. **Figure 12** (a) is the result of a series of FEM simulations for varying tip-sample separations and generally shows that decreasing the separation does lead to a CPD increase. Yet it was found in the FEM simulations that even if the tip-sample separation is halved, the corresponding CPD increase is ~ 30 mV; much less than the ~ 150 mV CPD increases seen in the experimental data. These results thereby show that the CPD increase near the edge of the electrodes is not primarily due to the sample geometry.

In order to examine if interface states give rise to the CPD increase, FEM simulations were also performed with a positive charge along the NW-electrode (SiO_2/Si_3N_4) interface, as indicated with arrows in the cross-sectional diagram inlaid in **Figure 12**(b). It is seen in **Figure 12**(b) that the CPD increases in FEM simulations are present on the same location and are of equal magnitude as in the experimental results in **Figure 11**. Thus, FEM simulations indicate that it is not the sample geometry but SiO_2/Si_3N_4 interface states that lead to the CPD increase. Moreover, when the CPD line profile taken with an applied voltage $V_{AB} = 0$ V is subtracted from the line profile for $V_{AB} = 0.50$ V, shown in **Figure 12** (c), we obtain a normalized CPD line profile with a linear drop along the NW. The large increase in CPD at NW-electrode interfaces is not observed in the voltage-normalized simulated curves similar to the experimental voltage-normalized data. Also in agreement with experimental results, the voltage-normalized simulated data has a smaller potential drop than the applied bias across electrodes. Parallel capacitance

between probe and neighboring high potential electrode raises the measured CPD at the grounded electrode. Voltage normalization is thus demonstrated to be valid in-principle for understanding CPD response due to applied bias and resulting charge transport.

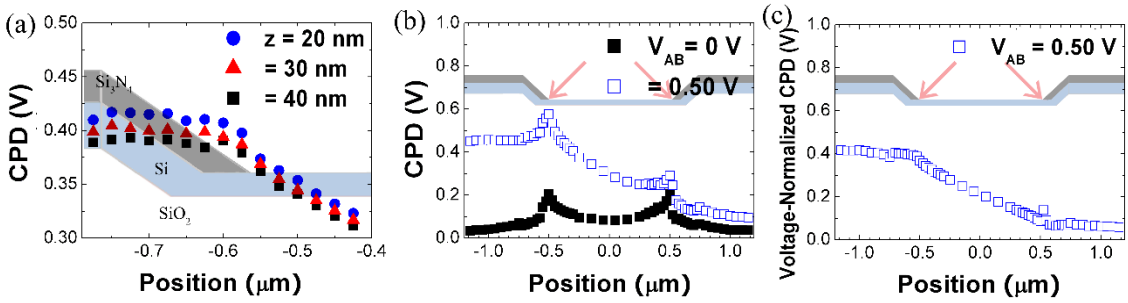

Figure 12: (a) Simulated CPD line profiles near the positive electrode, held at +0.50 V above the grounded electrode (V_{AB} = 0.50 V), for various tip-sample separations, where z is taken to be the vertical distance between the lowest point of the SPM tip and the sample. (b) Simulated CPD line profiles across a NW with positive interface charges inserted at the lowest point of the Si_3N_4 ramp (indicated with arrows). (c) Voltage-normalized CPD line profile, obtained by taking the difference between the two data sets in (b) point-by-point.

A CPD drop is observed in **Figure 11**b near 2.8 μm, at the NW2-electrode B junction that is not observed in simulated voltage-normalized curves. This change in the CPD at NW-electrode interface increases with increased applied bias indicating that it is correlated with contact resistance since FEM simulations do not include contact resistance. Using the voltage-normalized data and the measured current as a function of applied bias, contact resistance, R = ΔCPD(V)/I, was estimated between the NW and the electrodes from this feature at 2.8 μm. Note that there are several NWs between electrodes A and B; consequently, current can pass through multiple NWs. Thus, extracted contact resistances from the potential drops at the NW2-electrode interfaces can only provide minimum values for contact resistances; the actual contact

resistance is somewhat higher since the current through NW2 is somewhat lower than the total current. Due to a CPD spike in the voltage-normalized data near the high potential electrode (e.g. Electrode A in **Figure 10**c and **Figure 11**b), the contact resistance was thus only determined at the NW-low potential contact. For example, when the bias was reversed, we observed a similar CPD peak at the NW1-electrode B interface (opposite electrode from **Figure 11**b due to reversal of the bias). Thus in order to evaluate the contact resistance at both NW interfaces, the bias across the NW was reversed, thus reversing the location of the CPD spike and enabling the determination of the contact resistance on both sides of the NW. The measured potential drops, "ΔCPD: $V_{AB} > 0V$" and "ΔCPD: $V_{AB} < 0V$," at the NW2-electrode B and NW2-electrode A interface, respectively, are listed in **Table 1**as a function of applied bias, V_{AB}. Each value in the table corresponds to a single representative measurement. The applied bias is listed in the first row, the measured current across the electrodes in response to the listed V_{AB} is listed in the second row. The contact resistance (ΔCPD(V)/I) is estimated at 3.7 kΩ at the NW2-electrode B interface when $V_{AB} > 0V$ and 3.5 kΩ at the NW2-electrode A interface when $V_{AB} < 0V$. These values are basically the same within experimental error. Assuming the NW diameter of 240 nm, as determined from the full width at half maximum in topography line profiles, the specific resistance is estimated as 1.6 ± 0.3 (1σ, n=8) μΩ cm^2. Note that there are eight independent measurements in **Table 1** to estimate the contact resistance and the 19% standard deviation is consistent with some electrostatic screening of the surface potential due to the thin SiO_2 layer on the surface. Nevertheless, this determined specific resistance is consistent with that reported for a single VLS NW, 4.4±0.6 μΩ cm^2, grown in a similar manner to span two electrodes.[28] Furthermore, SEM images typically show less than 8 NWs across the electrodes.

Thus the contact resistance is still estimated to be very low (≤ 10 μΩ cm^2) even when considering there are other NWs in parallel. In comparison contact resistance for Ti/Au contacts to p-type Si NWs was reported as 500 μΩ cm^2.[29] The low contact resistance in the VLS Si NWs studied here is in agreement with a previously- measured, nearly ideal, current response (low contact resistance) as a function of applied gate voltage for devices fabricated using the same fabrication protocol.[6, 21]

Table 1: Current-Voltage response and associated CPD variation at NW2-electrode interfaces.

$\|V_{AB}\|$ (V):	0.25	0.50	0.75	1.00
Current (μA):	11	25	41	55
ΔCPD (mV): (V_{AB} < 0V)	50	80	120	180
ΔCPD (mV): (V_{AB} > 0V)	70	95	125	135

Figure 11 shows a clear trend between the CPD responses across the NW as a function of different applied voltages after voltage normalization. When examining similar data across a Si NW that is not connected to both electrodes there is a similar CPD response before normalization as can be seen in **Figure 13**a. **Figure 13**b shows the voltage-normalized CPD line profiles for this NW; the corresponding 3 μm × 3 μm KPFM image acquired at V_{AB} = 1 V is shown in **Figure 13**d. Surprisingly, the line profiles do not exhibit significant differences from those depicted in **Figure 11**b; the CPD across the disconnected NW versus voltage is slightly non-linear after voltage-normalization whereas the CPD across the connected NWs of **Figure 11**b

and **Figure 11**d are not. Yet the differences are not obvious. In **Figure 13**e, the CPD response of the SiO_2 trench under applied bias is shown. The CPD increases seen on both sides of the NW trench are still present here, where there is no NW. First, this data shows that the interface states that are responsible for this behavior are therefore not dependent on the NW-electrode interface, but rather on the SiO_2 trench- Si_3N_4 covered electrode interface. This can be explained as trapped charge, at the Si_3N_4-SiO_2 interfaces, which have been studied in depth for their charge storage properties.[30] Upon voltage-normalization, there is a similar non-linear response of the SiO_2 trench as observed for the disconnected NW. Voltage-normalized data for the SiO_2 trench is shown in **Figure 13**f. It has been observed previously, when examining CPD data across NWs that are not electrically connected,[18] that unconnected NWs also have a similar CPD response after voltage normalization as the SiO_2 trench.

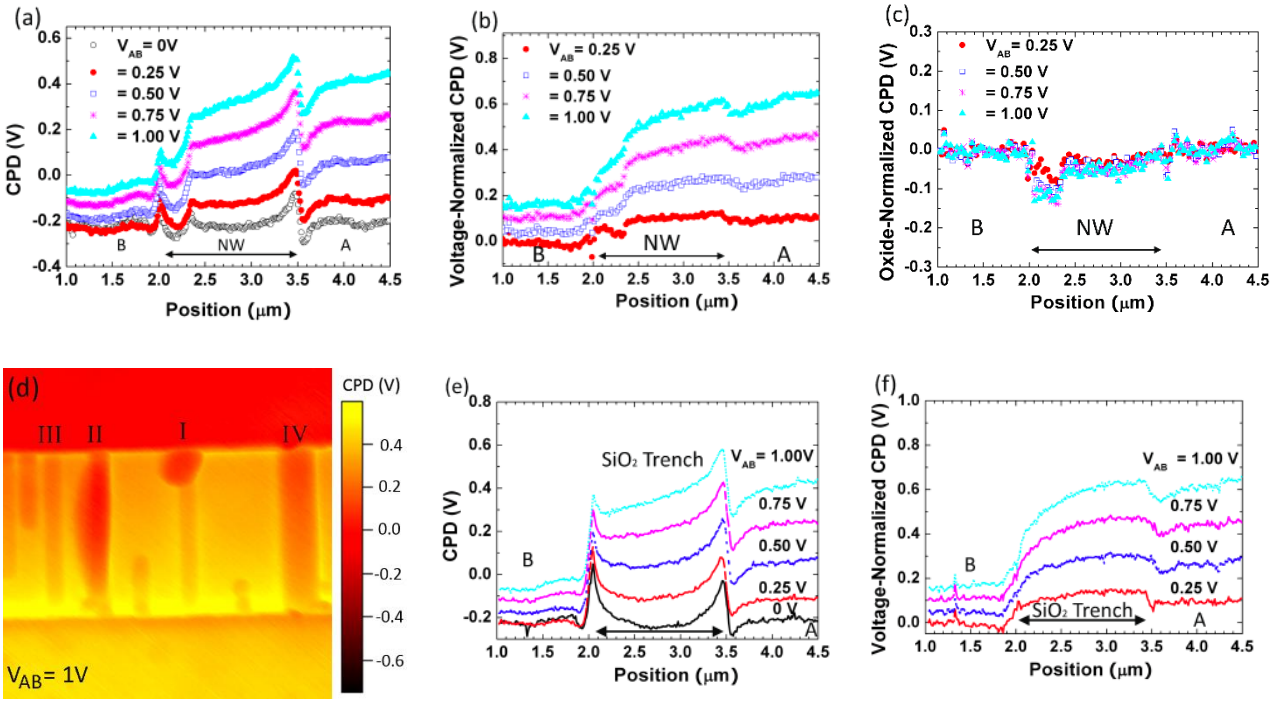

Figure 13: (color online): CPD line profiles at different applied voltages across (a) an unconnected Si NW. (b) Voltage-normalized CPD line profile and (c) oxide-normalized CPD data for the same NW labeled I in 3 μm × 3 μm KPFM image acquired at V_{AB} = 1 V shown in (d). (e) CPD line profiles at different applied voltages across SiO_2 trench adjacent to NW. (f) Voltage-normalized CPD line profiles for the SiO_2 trench.

The differences in physical connections of the NWs of **Figure 11** versus **Figure 13** suggest there should be a way to clearly differentiate the two NWs and their surface potential responses when there is an applied bias across them. We find that only when the CPD line profiles are normalized by subtracting the voltage-normalized SiO_2 CPD, e.g. at V_{AB} = 1 V, across the neighboring oxide trench from the voltage-normalized CPD taken across the NW at the same voltage, e.g. at V_{AB} = 1 V, can we distinguish between the connected and disconnected NWs. This procedure is referred to as oxide-normalization. (The oxide-normalized CPD thus has two normalization procedures, first voltage normalization followed by oxide normalization.) The oxide-normalized, CPD line profiles for the disconnected NW are shown in **Figure 13**c. After oxide-normalization the CPD response versus voltage is approximately zero across the NW. The only exception is the decrease in CPD associated with residual Au from the growth process that remains at the 2.2 μm position after oxide normalization. Au can induce acceptor defects in Si NWs that would exhibit a bias-dependent response[14, 18] that would remain after voltage normalization. The impurity state is clearly observed in the oxide-normalized data. Overall this analysis suggests that the surface potential of the disconnected NW does not significantly differ from the SiO_2 trench under an applied bias and the changes observed in the raw KPFM data of the disconnected NW in **Figure 13**a are attributable to the SiO_2 capacitive response to V_{AB} and are not related to current flow in the NW.

We investigated the bias-dependent behavior of several NWs in relationship to the bias-dependent response of the SiO_2 trench further to understand the response of Si NWs. For comparison an example of raw CPD data and voltage-normalized CPD data for a connected NW, labeled II in **Figure 13**d, is shown in **Figure 14**a and **Figure 14**b, respectively. The oxide-normalized, CPD line profiles for the connected NW II, **Figure 14**c, shows a monotonic decrease in surface potential as V_{AB} increases form 0.25 V to 1 V when compared to that acquired at V_{AB} = 0. In **Figure 14**c, the gradual reduction in the CPD as one decreases the applied bias from 1 to 0 V is associated with accumulation of electrons in the NWs leading to an increase in Fermi energy.[14] In **Figure 14**d and 6e, oxide-normalized CPD data is shown for two other NWs, labeled III and IV in **Figure 13**d, connected to the same electrodes. The increase in Fermi energy is larger with applied bias for NW II when comparing with NW III and NW IV. The oxide-normalized data of **Figure 14**c-e thus provides information of the relative amount of current flowing across the NWs.

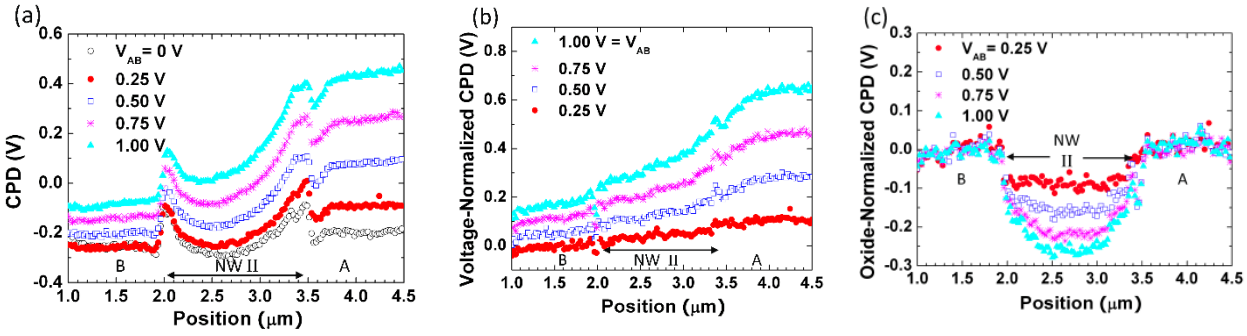

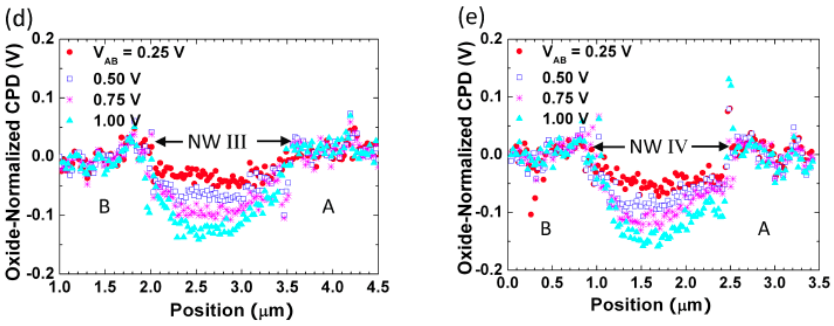

Figure 14: (color online): CPD line profiles at different applied voltages across (a) connected Si NW (labeled II in **Figure 13**d). (b) Voltage-normalized and (c) oxide-normalized CPD line profile for the same Si NW. Oxide-normalized CPD data for Si NW labeled (d) III and (e) IV in the KPFM image of **Figure 13**d.

Conclusion

We have characterized VLS-grown Si NWs using KPFM with an applied bias across the NWs and have found that proper normalization alongside FEM simulations is necessary to analyze the data. We have performed two types of normalization, voltage- and oxide-normalization procedures as detailed above. The results show that voltage normalization mitigated contact potential differences due to localized charge and material work function variations while oxide normalization mainly removed contact potential differences due to the structure's capacitance. These procedures have enabled us to estimate the NW contact resistance and locate poor NW connections to the electrodes. We estimated the contact resistance between the NW and the electrodes at a few $\mu\Omega$ cm^2. This is quite low and this KPFM method gives researchers a way to characterize contact resistance to semiconductor NWs; contact resistance has often been a problem when fabricating NW devices, especially when one deposits metal directly onto the semiconductor NW to make a device.

By correcting for contributions from the oxide capacitance, NWs with poor electrical connections have significantly different surface potential response to an applied bias than NWs connected to both electrodes. The CPD of the oxide-normalized, disconnected NW is about zero over all positions that do not have residual Au, suggests that all major contributions to CPD variations have been accounted for using these two normalization procedures and lends credence to the usage of voltage and oxide-normalization processes to understand the bias dependent response associated with current flow and impurity states. Overall, the presented characterization method is particularly useful for measuring uniformity of electronic behavior such as local current flow when NWs are connected in parallel.

References

[1] R. S. Wagner, W. C. Ellis, Appl. Phys. Lett. 1964, 4, 89.

[2] in *International Technology Roadmap for Semiconductors*, www.itrs.net/reports.html.

[3] D. K. Taggart, Y. G. Yang, S. C. Kung, T. M. McIntire, R. M. Penner, Nano Lett., 11, 2192.

[4] A. L. Briseno, S. C. B. Mannsfeld, C. Reese, J. M. Hancock, Y. Xiong, S. A. Jenekhe, Z. Bao, Y. N. Xia, Nano Lett. 2007, 7, 2847.

[5] J. I. Heo, D. S. Shim, G. T. Teixidor, S. Oh, M. J. Madou, H. Shin, J. Electrochem. Soc., 158, J76.

[6] N. J. Quitoriano, T. I. Kamins, Nano Lett. 2008, 8, 4410.

[7] Y. Martin, D. W. Abraham, H. K. Wickramasinghe, Appl. Phys. Lett. 1988, 52, 1103.

[8] S. Hudlet, M. Saintjean, B. Roulet, J. Berger, C. Guthmann, J. Appl. Phys. 1995, 77, 3308.

[9] Y. Rosenwaks, R. Shikler, T. Glatzel, S. Sadewasser, Physical Review B 2004, 70, 085320.

[10] G. N. Luo, K. Yamaguchi, T. Terai, M. Yamawaki, J. Alloy Compd. 2003, 349, 211.

[11] H. O. Jacobs, P. Leuchtmann, O. J. Homan, A. Stemmer, J. Appl. Phys. 1998, 84, 1168; R. Baier, C. Leendertz, M. C. Lux-Steiner, S. Sadewasser, Physical Review B 2012, 85.

[12] T. Glatzel, S. Sadewasser, R. Shikler, Y. Rosenwaks, M. C. Lux-Steiner, Mater. Sci. & Engin. B 2003, 102, 138.

[13] W. J. Ouyang, A. Shinde, Y. N. Zhang, J. X. Cao, R. Ragan, R. Q. Wu, ACS Nano, 5, 477.

[14] E. Koren, G. Elias, A. Boag, E. R. Hemesath, L. J. Lauhon, Y. Rosenwaks, Nano Letters 2011, 11, 2499.

[15] E. Koren, J. K. Hyun, U. Givan, E. R. Hemesath, L. J. Lauhon, Y. Rosenwaks, Nano Lett. 2011, 11, 183.

[16] A. K. Henning, T. Hochwitz, J. Slinkman, J. Never, S. Hoffmann, P. Kaszuba, C. Daghlian, J. Appl. Phys. 1995, 77, 1888; F. Robin, H. Jacobs, O. Homan, A. Stemmer, W. Bachtold, Appl. Phys. Lett. 2000, 76, 2907.

[17] T. Mizutani, M. Arakawa, S. Kishimoto, IEEE Electr. Device L. 1997, 18, 423.

[18] S. S. Bae, N. Prokopuk, N. J. Quitoriano, S. M. Adams, R. Ragan, submitted to Nanotechnology 2012.

[19] E. Koren, Y. Rosenwaks, J. E. Allen, E. R. Hemesath, L. J. Lauhon, Appl. Phys. Lett. 2009, 95, 092105.

[20] L. Yan, C. Punckt, I. A. Aksay, W. Mertin, G. Bacher, Nano Lett. 2011, 11, 3543.

[21] N. J. Quitoriano, W. Wu, T. I. Kamins, Nanotechnology 2009, 20, 145303.

[22] L. Nony, A. Baratoff, Phys. Rev. B 2006, 74, 235439.

[23] E. Koren, N. Berkovitch, Y. Rosenwaks, Nano Lett. 2010, 10, 1163.

[24] S. Saraf, M. Molotskii, Y. Rosenwaks, Appl. Phys. Lett. 2005, 86, 172104.

[25] G. Leveque, P. Girard, E. Skouri, D. Yarekha, Appl. Surf. Sci. 2000, 157, 251; K. D. Katzer, W. Mertin, G. Bacher, A. Jaeger, K. Streubel, Appl. Phys. Lett. 2006, 89, 3.

[26] K. I. Seo, S. Sharma, A. A. Yasseri, D. R. Stewart, T. I. Kamins, Electrochem. Solid St. 2006, 9, G69.

[27] S. Sadewasser, C. Leendertz, F. Streicher, M. C. Lux-Steiner, Nanotechnology 2009, 20, 10.

[28] A. Chaudhry, V. Ramamurthi, E. Fong, M. S. Islam, Nano Lett. 2007, 7, 1536.

[29] S. E. Mohney, Y. Wang, M. A. Cabassi, K. K. Lew, S. Dey, J. M. Redwing, T. S. Mayer, Solid-State Electron. 2005, 49, 227.

[30] V. Leonov, C. Van Hoof, M. Goedbloed, R. van Schaijk, IEEE Trns. Dielectr. Electr. Insul. 2012, 19, 1253.

CHAPTER IV: Evaluation of Young's Modulus of tethered POPC Membranes using Atomic Force Spectroscopy

The work presented in this chapter characterizes a tethered POPC lipid bilayer membrane system. It is found that by varying the concentration of tethering molecule DSPE-PEG-PDP, the stiffness of the membrane can be modulated. This is a highly desirable quality in a number of systems, including biosensing scaffolds. Control of a membrane's stiffness also allows for control of properties such as the membrane's bendability and diffusion rates through the membrane, and could give a degree of control over the sensitivity and specificity of lipid bilayer membrane-based biosensing systems.

Abstract

Unilamellar vesicles composed of 1-palmitoyl-2-oleoyl-*sn*-glycero-3-phosphocholine (POPC) with varying 1,2-distearoyl-*sn*-glycero-3-phosphoethanolamine-*N*-poly (ethylene glycol)-2000-*N*-[3-(2-pyridyldithio) propionate] (DSPE-PEG-PDP) concentration between 0 mol% and 24 mol% were assembled on atomically flat template-stripped gold (TS Au) surfaces. Force spectroscopy, using an atomic force microscope (AFM), of the resulting tethered lipid bilayer membranes (tLBMs) in buffer provided information regarding mechanical response as a function of tethering molecule, DSPE-PEG-PDP concentration. Young's modulus was

determined by fitting the force-indentation curve with a recently modified Sneddon model that corrects for contributions from the substrate underneath. At low concentrations, Young's modulus is lower than that of a supported POPC LBM, i.e., directly sitting on solid substrate. The decrease in modulus is attributed to increased membrane fluidity as coupling between the tLBM and solid substrate is reduced by the incorporation of DSPE-PEG-PDP tethering groups. From determined Young's modulus values, the PEG chain conformation is found to dominate tLBM rigidity at concentrations above 6 mol%. Analysis of AFM force spectroscopy data indicates the PEG mushroom to brush transition occurs near 6 mol%, and this leads to first softening and then abrupt stiffening of tLBMs at higher DSPE-PEG-PDP concentration associated with the transition. When DSPE-PEG-PDP concentration is increased to 24 mol%, AFM topography and Young's modulus appear correlated with another phase transition; AFM topography images are consistent with a bilayer disk structure with DSPE-PEG-PDP segregated at the rim of the disk.

Introduction

Lipid bilayer membranes (LBMs) are a systems of considerable research interest since early work showing their formation on solid supports,[1] and the ability to probe systems electrically[2] and to study molecular events during membrane-membrane interactions.[3] Incorporation of a polymer cushion layer between LBMs and substrates has been shown to alleviate both immobility of transmembrane proteins and reduced lipid diffusion rates that are observed in solid supported LBMs[4] providing a platform for studying biological processes in controlled systems.[5–8] The tethered lipid bilayer membrane (tLBM) is one type of hybrid bilayer membrane whose chemical affinity between the LBM and the solid substrate stabilizes

the system and can provide a hydrated spacer layer between LBM and substrate. Poly(ethylene glycol) (PEG) has been commonly used as a polymer cushion layer as it produces fluidic and stable LBMs.[9–11] LBM have become an important tool to understand biological mechanisms such as function of photosynthetic membrane proteins,[12] intercellular signaling,[13] small molecule interactions with membrane surfaces,[14] and create single virus sensors.[15]

Here we investigate the mechanical properties of tLBM on gold (Au) electrodes assembled using vesicle fusion. tLBMs are formed by incorporating DSPE-PEG-PDP molecules into POPC vesicles to affect vesicle substrate interactions in order to facilitate vesicle fusion.[11,16] The concentration of DSPE-PEG-PDP tethering molecules is varied and we investigate the resulting changes in morphology and mechanical properties using atomic force spectroscopy and analysis of force-separation data with analytical models. Understanding the mechanical properties of LBMs is important as this parameter plays a role in several membrane mediated biological processes. Molecular dynamics simulations have shown that lateral pressure in membranes affects protein function[17–19] and protein binding produces an asymmetrical mechanical response in the membrane.[20] Non-specific interactions with surrounding lipids and proteins such a membrane curvature and elastic moduli affect the function of ATP-binding cassette (ABC) proteins,[21] mechanosensitive ion channels important in bacterial membrane defense against lysis,[22] and mechanotransduction was found to initiate ATP release in urothelial cells.[23] Variations of Young's modulus have been found between malignant cancer cells and normal cells.[24–26]

Atomic force microscopy (AFM), since shortly after its invention, has been an important tool to image cells with nanometer resolution under physiological conditions[27] with pico-Newton force sensitivity[28,29] and combined with fluorescence microscopy nanoscale imaging of

cellular receptors is possible.[30] The nanoindentation function, where the AFM tip compresses the sample and records the resulting force as a function of indentation, allows for measuring local elastic properties of membranes and vesicles.[24–26,31–33] Uncertainties in the tip-sample contact point, assumptions in theoretical models, and instrument uncertainties can affect accuracy of determined moduli from force spectroscopy data.[34] Recently Wagner et al. found that the calibration of the sensitivity of the photodiode dominated instrument uncertainty rather than uncertainties in the cantilever stiffness or Z-piezo calibration.[35] Though this can be minimized by calibrating on a clean surface[36] and thus we address the latter two issues here.

The mechanical properties of untethered POPC LBM on mica and tLBM of POPC with varying DSPE-PEG-PDP concentration from 2.5 mol % to 24 mol % on Au were studied and compared using AFM force spectroscopy. Previously we found that higher DSPE-PEG-PDP concentration in large unilamellar vesicles (LUV) facilitated vesicle fusion on TS Au surfaces.[16] It was found that DSPE-PEG-PDP concentrations in LUV required less force for tLBM formation and this was attributed to increase in LUV-substrate interactions and mechanical properties were not studied. Here we compare the Sneddon[37] (semi-infinite sample contacted by a paraboloidal-shaped tip) with a new modified model, Bottom Effect Cone Correction,[38] that corrects for the thickness-dependent influence of the interaction of a sharp AFM tip with a hard substrate on measured mechanical response[39] of LBMs. We also provide new algorithms for determining the tip-sample contact point as misidentification of the contact point can lead to errors in determined mechanical properties.[34,40] Young's modulus (E) of tLBMs was determined by fitting experimental data to Sneddon and Bottom Effect Cone Correction (BECC) models. E was found to be directly correlated with PEG chain conformation. Results show an initial decrease in tLBM elastic modulus with respect to supported POPC LBM then an abrupt increase

at DSPE-PEG-PDP concentration of 8% after the mushroom to brush transition has been reported to occur.[41,42] Incorporating higher concentrations of DSPE-PEG-PDP, up to 24%, results in a further increase in E and a structural change, also associated with a phase transition, is observed in AFM topography. AFM topography data indicates that PEG chains segregate at the rim of bilayer disks at 24% DSPE-PEG-PDP concentration. Analysis of force spectroscopy data with the BECC model provides a cleaner signature of the phase transition points than the Sneddon model. These studies provide a systematic method to probe local mechanical properties and phase transitions of thin film polymers, biological membranes, and cellular structure using sharp AFM tips while mitigating influence from the hard substrate underneath and errors in determining the contact point.

Materials and Methods

Materials. 1-Palmitoyl-2-oleoyl-*sn*-glycero-3-phosphocholine (POPC) and 1,2-distearoyl-*sn*-glycero-3-phosphoethanolamine-*N*-poly(ethylene glycol)-2000-*N*-[3-(2-pyridyldithio) propion-ate] (DSPE-PEG-PDP) were obtained from Avanti Polar Lipids (Alabaster, AL). HEPES at >99.5% purity and chloroform at >99.8% purity were purchased from Sigma-Aldrich (St. Louis, MO). NaCl at >99.0% purity was from Fisher Scientific Inc. (Pittsburgh, PA). Water used in this study was purified with a Milli-Q water system (≥ 18.2 MΩ.cm, Millipore Corp., Billerica, MA). All chemicals were used as received.

Preparation of Unilamellar Vesicles. Large unilamellar vesicles were prepared following an extrusion method.[8,43] Vesicles composed primarily of POPC lipids with (i) 0 % (ii) 2.5 % (iii) 5 % (iv) 6 % (v) 8 % (vi) 10 % and (vii) 24 % DSPE-PEG-PDP were prepared. DSPE-PEG-PDP and POPC lipids were dissolved at specified molar ratios in chloroform at 1 mg/mL for stock

solutions. Lipid-chloroform mixtures were dried on the bottom of a glass vial by a gentle stream of nitrogen and desiccated in vacuum for at least 1 h to completely remove chloroform. Then, the dried lipid mixtures were rehydrated by the addition of HEPES buffer (5 mM HEPES, pH 7.4, with 150 mM NaCl) to yield a final lipid concentration of 5 mM. The resulting lipid suspensions were then subjected to five freeze-thaw cycles, and extruded 15 times through two polycarbonate membranes with a pore size of 100 nm using a syringe-type extruder (Avanti Polar Lipids, Alabaster, AL).

Sample Preparation. A tethered LBM refers to a membrane that is linked to a substrate via chemical bonding, while an untethered LBM indicates no chemical bond formation between the LBM and substrate. Untethered LBMs, or simply LBMs, were prepared by depositing a 100 μL aliquot of vesicle suspension composed of 0% DSPE-PEG-PDP/100% POPC on mica. Mica was freshly cleaved with scotch tape immediately prior to use. TLBMs with varied DSPE-PEG-PDP concentration were prepared at room temperature by depositing a 100 μL aliquot of vesicle suspension with lipids composition of (i) 2.5% DSPE-PEG-PDP/97.5% POPC, (ii) 5% DSPE-PEG-PDP/95% POPC, (iii) 6% DSPE-PEG-PDP/94% POPC, (iv) 8% DSPE-PEG-PDP/92% POPC, (v) 10% DSPE-PEG-PDP/90% POPC, and (vi) 24% DSPE-PEG-PDP/76 % POPC on an 8 mm × 8 mm Au substrate. Au substrates were prepared using the facile method of template stripping method to create a pristine and atomically flat surface for membrane assembly.[11,44] All samples were incubated at room temperature for 30 min. After incubation, samples were rinsed with 200 μL of HEPES buffer 4 times and glued to a glass slide for AFM characterization. Sample surfaces remained hydrated in HEPES buffer at all times during sample preparation and AFM characterization.

Atomic Force Microscopy Imaging and Force Spectroscopy. Both AFM imaging and force spectroscopy were performed using a MFP-3D-Bio AFM (Asylum Research, Santa Barbara, CA) in an acoustic isolation enclosure. Commercial silicon nitride AFM probes (OMCL-TR 400 PSA, Olympus) with pyramid-shaped tips and Au coating on the reflective side of the cantilever were used for all AFM measurements. The tip radius of curvature is 20 ± 5 nm as provided by the manufacturer. Both AFM imaging and force spectroscopy were carried out at a temperature of 23 ± 1 °C in HEPES buffer. AFM images were acquired under tapping mode with a scan speed of 1.0 Hz. All topography images were rendered with background slopes corrected using *Igor Pro* software v 6.0.

AFM force spectroscopy was performed in contact mode. The nominal spring constant of AFM cantilever specified by manufacturer is 0.08 N/m. Before acquiring force measurement data, AFM cantilever spring constant was calibrated by measuring deflection against a freshly stripped TS Au substrate to minimize surface contaminants and then calculated by the thermal noise method.[45] Force measurements were obtained on randomly chosen positions on tLBM covered substrates. Force measurements were performed with an approaching speed of 1.8 μm/s.

Analysis of Force-Separation Data. Force-separation data obtained from AFM force spectroscopy were analyzed using an algorithm developed within the framework of Wolfram Mathematica 9.0. The algorithm was designed to import force vs. separation data and to output LBM and tLBM thickness and Young's modulus using the two models, Sneddon and Bottom Effect Cone Correction (BECC). Identification of the AFM tip/LBM contact point was achieved by determining the change in force-separation behavior from a polynomial (predicted by the above two models) to an exponential decay that is related to long-range electrostatic interactions

and interactions with the polymer brush. The contact point was iterated until the theoretically expected fit to the experimental curves was within one standard deviation. Data points near this contact point were then fitted to Sneddon and BECC models of tip-LBM interaction using least-squares methods to find the elastic modulus of the tLBM.

Results and Discussion

Formation of LBMs as a function of DSPE-PEG-PDP concentration. Large unilamellar vesicles of POPC with DSPE-PEG-PDP concentration ranging from 0% to 24% were prepared in HEPES buffer. In the case of pure POPC vesicles, these were deposited on mica since POPC vesicles do not spontaneously fuse to form LBM on plasma treated TS Au but simply adsorb.[11] POPC vesicles with varied DSPE-PEG-PDP tethering molecule concentration, ranging from 2.5% to 24%, were incubated on TS Au surfaces as described above and in our previous work.[11] It was found that tLBMs form on TS Au via Au-thiolate interactions between the disulfide bond in PDP group and the Au substrate; the process can be assisted with an external force of an AFM probe.[16] In this prior work higher DSPE-PEG-PDP concentrations in vesicles required less force for tLBM formation that was attributed to increased vesicle substrate interactions and mechanical properties were not evaluated. Here we examine how the morphology and mechanical properties are affected by increasing the concentration of the tethering molecule. **Figure 15** shows 2 μm × 2 μm AFM topography images of (a) TS Au, (b) POPC LBM on on mica and (c-f) tLBM on TS Au with varying DSPE-PEG-PDP concentration.

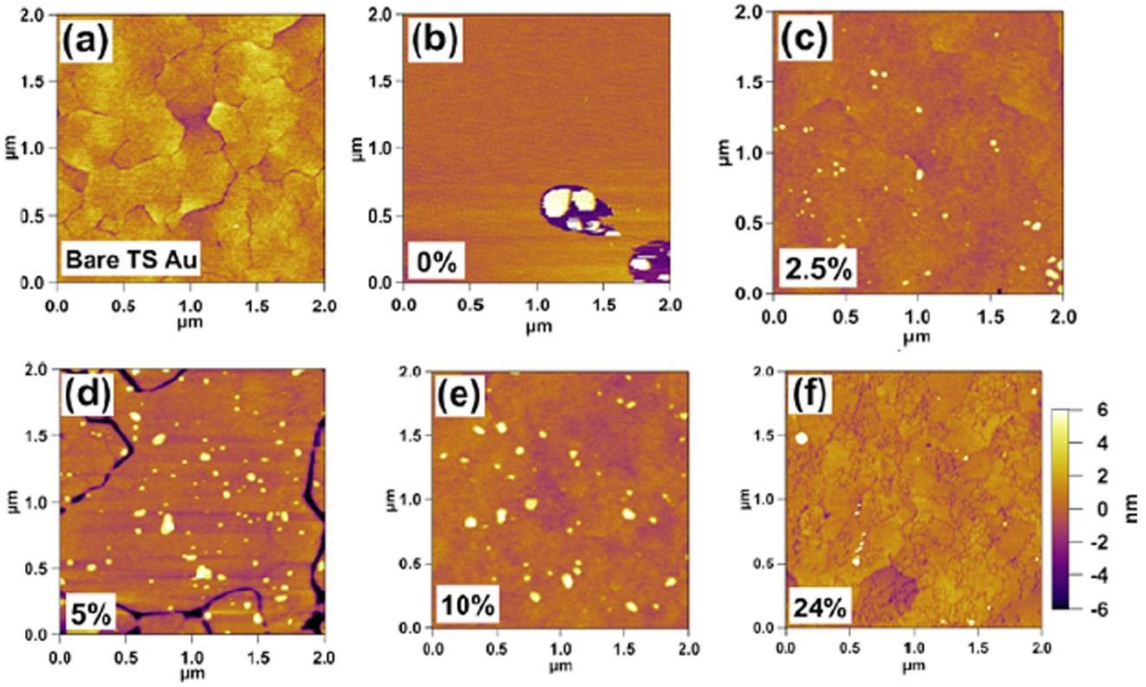

Figure 15: Tapping mode AFM topography images of (a) bare TS Au; (b) mica after incubation with vesicles composed of 100% POPC and TS Au after incubation with vesicles composed of (c) 2.5% DSPE-PEG-PDP/97.5% POPC; (d) 5% DSPE-PEG-PDP/95% POPC; (e) 10% DSPE-PEG-PDP/90% POPC; (f) 24% DSPE-PEG-PDP/76% POPC.

Subtle changes in topography can be observed in the AFM images of **Figure 15**. In **Figure 15**a, the surface topography of a typical TS Au substrate is shown having low root mean square roughness, less than 0.6 nm over 2 µm × 2 µm. An AFM topography image of mica after 30 min incubation of POPC vesicles and rinsing with HEPES buffer is shown in **Figure 15**b. This image exhibits flat featureless regions corresponding to a POPC LBM and a few bright regions, indicating unruptured vesicles incorporated in the LBM. **Figure 15**c-f shows AFM topography images of TS Au after 30 min incubation with POPC vesicles containing 2.5%, 5%, 10%, and 24% DSPE-PEG-PDP, respectively. AFM images after vesicle fusion with vesicles having DSPE-PEG-PDP concentration from 2.5% to 10% are consistent with large area tLBM formation. Yet when further increasing DSPE-PEG-PDP concentration to 24% in POPC vesicles,

domain boundaries are observed in the AFM image of **Figure 15**f. These domains vary in size from approximately 50 nm up to 400 nm in diameter and the domain boundaries exhibit high, local curvature and are different from the domain boundaries of bare TS Au (shown in **Figure 15**a) and thus are not attributable to the TS Au surface morphology. For reference, **Figure 15**d provides an example how Au defects interrupt tLBMs when the TS Au surface preparation is not optimized and one can observe the features differs from those in **Figure 15**f. (Note that Au domains can be increased by annealing such that large defect free areas can be obtained.[46,47])

AFM force spectroscopy measurements were also performed on samples shown in **Figure 15** to gain insight into the origin of different observed surface morphology. Representative force-separation curves obtained from tLBMs with DSPE-PEG-PDP concentration varying from 0% to 24% are shown in **Figure 16**. The AFM tip interaction with a hard wall (TS Au surface) is used as the reference point.[48] All the curves show the characteristic breakthrough events attributed to an AFM tip penetrating a membrane on a hard surface.[33] The breakthrough distance measures the thickness of a compressed LBM under the force applied by AFM tip.[49] Average measured distances from breakthrough events from force-separation data are listed in **Table 2**. Histograms of measured breakthrough distances from $n \geq 150$ curves are shown as insets in **Figure 16**. The average breakthrough distance of the LBM composed of pure POPC is 2.9 ± 0.4 nm (n=150) in agreement with values previously observed.[11] From these curves, the average breakthrough distance for DSPE-PEG-PDP concentration between 2.5% - 10% was determined to be approximately the same, approximately 4.5 nm as observed previously.[11,41] At DSPE-PEG-PDP concentration of 24%, the breakthrough distance decreases to 3.5 ± 0.5 nm.

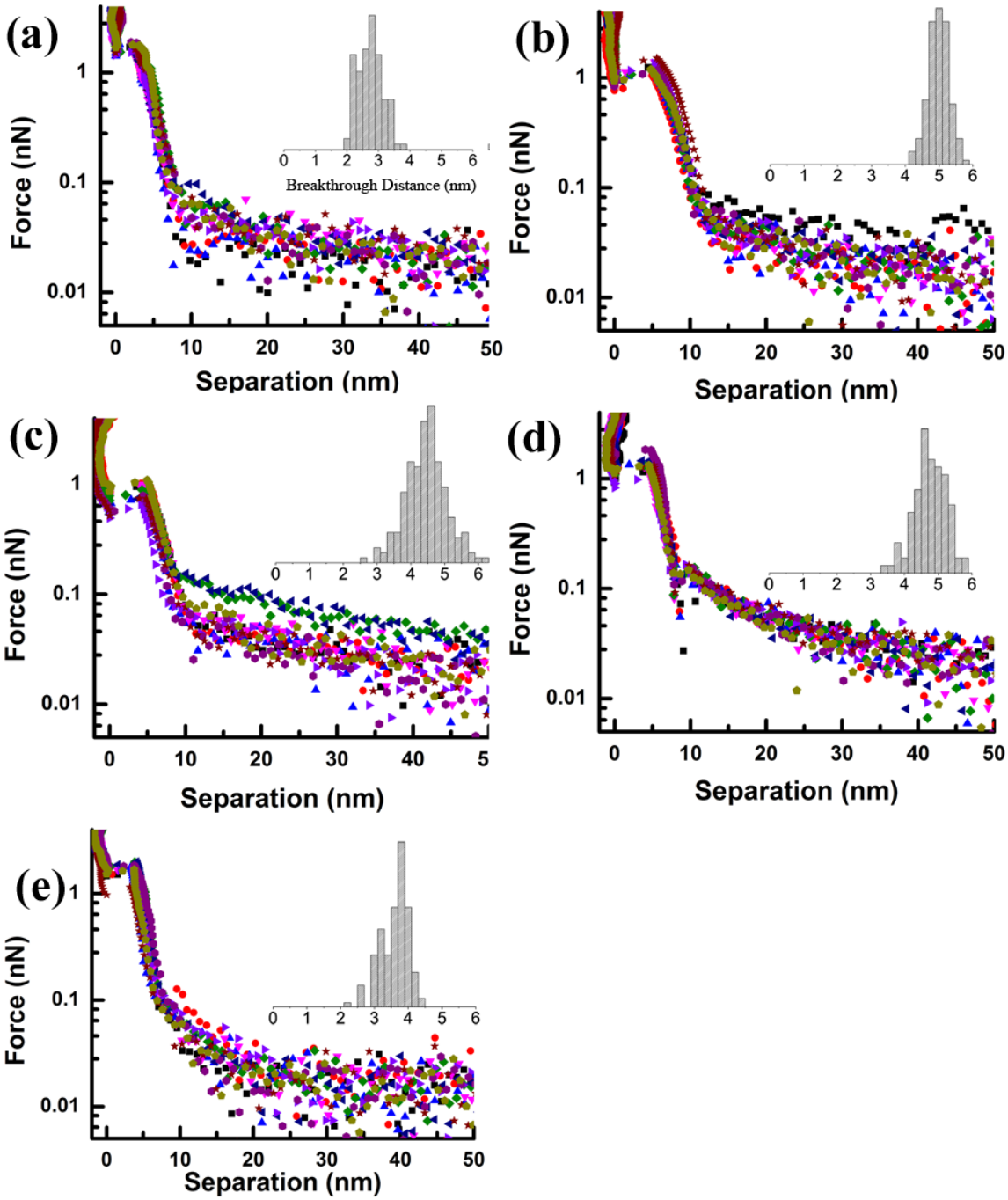

Figure 16: Representative force-separation curves in semilog-scale obtained from (a) 100% POPC LBM on mica and tLBM with (b) 2.5% DPSE-PEG-PDP/97.5% POPC, (c) 8% DSPE-PEG-PDP/92% POPC (d) 10% DSPE-PEG-PDP/90% POPC, and (e) 24% DSPE-PEG-PDP/76% POPC. Each force-separation plot in b-f includes ten curves from each sample. The insets are histograms of the breakthrough distance (in nm) determined from force-separation curves.

It is well known that the breakthrough distance underestimates the total thickness of LBM.[48,50] For example, the thickness for pure POPC membrane is calculated to be 3.9 nm[51,52] whereas the compressed LBM thickness measured via a breakthrough event is 2.9 nm. The total LBM thickness with hydration and spacer layer can be determined from the force-separation curve between the onset compression point and the hard wall contact point.[41,48] To obtain a statistically representative view of the samples, more than 150 force curves were analyzed for each data set in this study, necessitating the use of computational algorithms for data analysis. For each force curve, tLBM thickness was calculated using an iterative method. The batches of force-separation curves were analyzed using an algorithm implemented with Wolfram Mathematica 9.0. The hardwall (point A) and breakthrough (point B) locations were located by looking for the slope changes associated with the characteristic large jump in tip-sample separation as illustrated in **Figure 17**a between points 'A' and 'B.' The contact point (point C) was found by first performing a quadratic fit, as per the Sneddon Model,[37] representing the force on the AFM tip, on the data points to the right of point B, see **Figure 17**b. This is the first estimate of the location of the contact point that underestimates the LBM/tLBM thickness. The points immediately to the right of this first iteration of the contact point were then fitted to an exponential decay representing the longer-range interaction, such as electrostatic forces[33] and interaction with the polymer brush,[53] between the AFM tip and the LBM surface. The contact point was then iterated if the data to the right of the contact point deviated from an exponential fit by more than a standard deviation. The iteration continued until the fit beyond the contact point was within one standard deviation of an exponential fit. This provides a more accurate method to examine relative thicknesses of tLBMs as a function of DSPE-PEG-PDP concentration that is important to determine accurate values of elastic moduli.

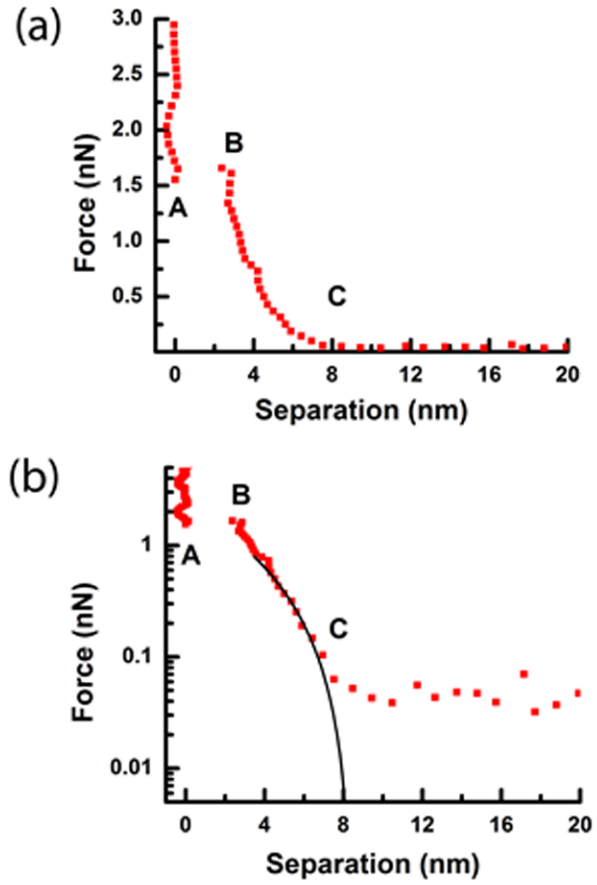

Figure 17: a) Characteristic force-separation curve. b) Semi-log force-separation curve with an overlay of a quadratic fit used to find the contact point.

Table 2: List of tLBM breakthrough distances and onset compression distances using the hard wall substrate contact for reference as measured from AFM force-separation as a function of DSPE-PEG-PDP concentration. Each listed value is the average mean determined from 25 different force-separation curves with the standard deviation also listed.

	0%	2.5%	5%	6%	8%	10%	24%
Breakthrough Distance	2.9	5.0	4.6	4.1	4.4	4.8	3.5

(nm)	± 0.4	± 0.3	± 0.5	± 0.7	± 0.8	± 0.6	± 0.5
Onset Compression Distance (nm)	8.8 ± 1.1	11.0 ± 0.6	9.2 ± 0.9	9.6 ± 1.4	10.0 ± 1.2	9.4 ± 1.03	8.2 ± 1.0

As listed in **Table 2**, the total LBM thickness estimated for 100% POPC LBM determined from the onset compression point to the hard wall contact point is 8.8 ± 1.1 nm, which is consistent with small angle neutron scattering measurements[54] for determination of POPC thickness and considering that an approximate 2 nm water layer is present between the hydrophilic substrate the inner leaflet of the LBM.[55,56] The force-separation curves for tLBMs with DSPE-PEG-PDP concentration ranging from 2.5% to 8% are not clearly distinguishable considering uncertainty in the thickness estimation. The estimated thickness is approximately 10 nm indicating an addition 2 nm hydration layer due to the tethering molecules. A slight decrease in thickness is observed at 10%, the estimated thickness of tLBMs formed from 10% DSPE-PEG-PDP/90% POPC vesicles is 9.4 ± 1.0 nm and then a large decrease to 8.2 ± 1.0 nm for tLBMs formed from 24% DSPE-PEG-PDP/76% POPC vesicles. The latter has an estimated thickness significantly smaller than those of lower DSPE-PEG-PDP concentrations and overlaps that of pure POPC. This abrupt thickness decrease indicates a structure change in the membrane at vesicle composition between 10% and 24 % DSPE-PEG-PDP concentration.

AFM tip-PEG polymer interaction. In order to further understand tLBM structure evolution with DSPE-PEG-PDP concentration, force-separation curves collected from tLBMs with varied

concentrations and were plotted in log-scale to expand the initial tip-sample interaction region. Note that in **Figure 16**a-e, ten data sets are plotted in each image to show the trends are reproducible. Backmann et al. studied conformational changes in PEG layers using AFM force spectroscopy; they observed an exponentially decaying long-range repulsive force when PEG was in the brush phase and a shorter range repulsive force when PEG was in the mushroom phase.[57] For example, in **Figure 16**a, pure POPC LBMs on mica shows an abrupt slope after the onset of the repulsive force as there are no PEG groups on the surface. At low DSPE-PEG-PDP concentration (2.5%), the force-separation curve shown in **Figure 16**b does not differ significantly from pure POPC, indicating PEG polymer chain on tLBM surface are in the mushroom phase. At higher DSPE-PEG-PDP concentration (8% and 10%), the long-range repulsive force increases in magnitude as observed in **Figure 16**c and **Figure 16**d; thus indicating the AFM tip is interacting with a PEG polymer brush on tLBMs. Though this is not a clear signature of a transition. A reverse trend occurs at DSPE-PEG-PDP concentration of 24 %, the overlaid force-separation curves in **Figure 16**e have an exponential tail lower in magnitude similar to pure POPC, **Figure 16**a. This data suggests that PEG polymer brushes are of lower density at DSPE-PEG-PDP concentration of 24% than 8% or 10%. This interaction was consistently observed in force-separation curves of tLBMs with 24% DSPE-PEG-PDP as observed in the overlaid data of **Figure 16**e; in addition all the curves at this highest measured concentration showed similar onset compression distance values similar to pure POPC on mica. Considering the observed changes in AFM topography in **Figure 15**f, changes in breakthrough distance, and total estimated thickness, a change in structure of tLBMS with 24% DSPE-PEG-PDP occurs that has not been observed before for tLBMs.

Determination of the Young's moduli of tLBMs with different DSPE-PEG-PDP concentration. In order to further understand differences in AFM data for tLBMs as a function of DSPE-PEG-PDP concentration, Young's modulus (E) of tLBM was extracted by first fitting force-indentation curves with the Sneddon model that assumes a conical shaped tip.[37] The relationship of the load (F_{cone}) versus indentation depth (δ) using the Sneddon model is given by:

$$F_{cone} = \frac{2}{\pi} \tan\alpha \frac{E}{1-\upsilon^2} \delta^2 \qquad (2)$$

where α is the opening angle of a conical tip (35° in this study), E is the Young's modulus of the film, ν is the Poisson's ratio of tLBMs equal to 0.5 assuming a perfectly incompressible materials in response to uniaxial strain.[34,39] With the contact point identified, the exponential long-range interaction was subtracted from the force data, and the data was then fit to the Sneddon model. **Figure 18**a shows histograms of the values of Youngs modulus as determined from the Sneddon model. **Figure 18**b is the plot of E as a function of DSPE-PEG-PDP concentration determined by fitting force spectroscopy data to the Sneddon model. Each E value plotted in **Figure 18**b is an average from those calculated from the slope of at least 150 force-indentation curves. For comparison, force spectroscopy data was also fit to a model, using the same method described above, that is a modification of the Sneddon model called the 'bottom effect cone correction' (BECC) that accounts for contribution of the substrate stiffness that lead to overestimation of E when fitting data acquired with a sharp AFM tip for polymer thin films or cell membranes.[38]

$$F_{\mathrm{BECC}} = \frac{8}{3\pi} E \tan\theta \, \delta^2 \left(1 + 1.7795 \frac{2\tan\theta}{\pi^2} \frac{\delta}{h} + 16(1.7795)^2 \tan^2\theta \, \frac{\delta^2}{h^2}\right) \qquad (3)$$

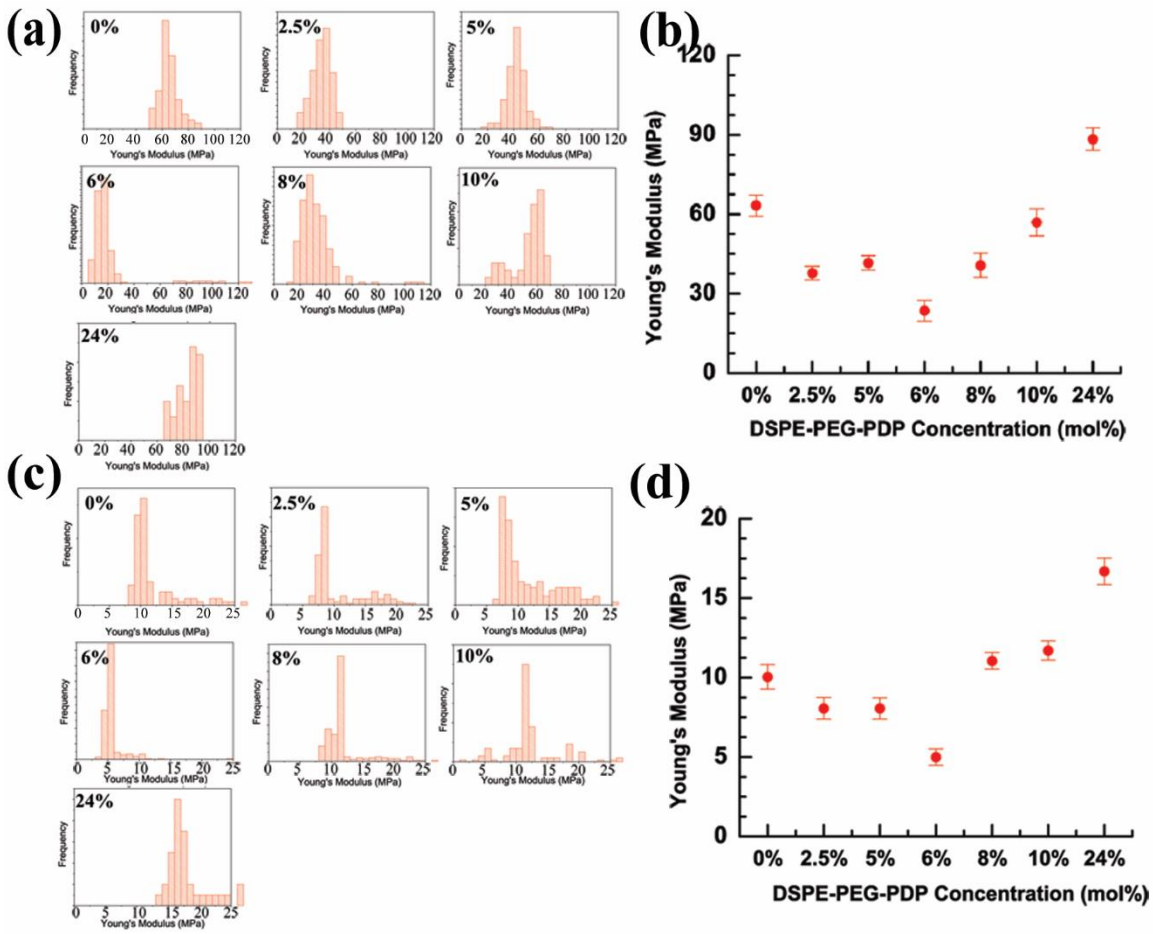

Figure 18: Histograms of the determined values of Young's modulus by fitting force-separation curves using the (a) Sneddon and (c) BECC models. Plot of tLBM Young's moduli as a function of DSPE-PEG-PDP concentration determined from force spectroscopy data by fitting the (b) Sneddon and (d) BECC model. The error bars represent the deviation in the measurements and fits.

Histograms of the value of Young's modulus determined from the BECC model and the resulting average value with standard deviation are shown in **Figure 18**c and **Figure 18**d, respectively. Qualitatively, in **Figure 18**b and **Figure 18**d, one can observe that fitting of the data with both models show an initial decrease in E with the addition of DSPE-PEG-PDP and then an increase at the highest concentrations. It is also immediately evident that E values are higher when analyzed with the Sneddon Model[37] versus BECC model.[38] It is expected as the BECC model

utilizes the Betti-Rayleigh reciprocal theorem to correct for finite thickness differences that influence analysis of force spectroscopy data and lead to higher values of E. The influence of the hard substrate in E values is expected to be greater as the thickness of films/membranes decreases.[38,39] Notice that the pure POPC data (onset compression distance of 8.8 nm) has a greater overestimation of the mean value of E, 63 ± 4.0 MPa from Sneddon model and 10.0 ± 0.8 MPa from BECC model, than 2.5% DSPE-PEG-PDP (onset compression distance of 11.0 nm), 38 ± 2.5 MPa from Sneddon model and 8.1 ± 0.7 MPa from BECC model. The decrease of E with the incorporation of DSPE-PEG-PDP is reflective of a PEG polymer cushion separating LBMs from TS Au substrates and is an indirect indication of increased membrane fluidity for tLBMs with respect to solid supported LBMs. Comparing the E values for tLBMs of **Figure 18** to published results, Picas et al. reported E values of dioleoyl PC/ dipalmitoyl PC (DOPC/DPPC) LBM on mica with an E value of 19.3 MPa and 28.1 MPa for liquid and gel phases, respectively.[58]

Further increases of DSPE-PEG-PDP concentration up to 6% shows a further decrease of E to 5.0 ± 0.5 MPa. (Note that from this point on mean values of E from only BECC model will the referred to in the text.) The reduction in membrane rigidity at 6% DSPE-PEG-PDP concentration that is evident in both models suggests a PEG mushroom to brush transition occurs near this concentration due to an increase in disorder in tLBMs at the phase transition. This is further substantiated by the abrupt increase in E at 8% DSPE-PEG-PDP, 11.0 ± 0.5 MPa, which overlaps with that for tLBMs containing 10% DSPE-PEG-PDP, 11.7 ± 0.6 MPa. The observed increase in E is consistent with incorporated PEG chains in the brush conformation as the brush conformation is less compressible than in the mushroom conformation.[41] The transition from the mushroom to brush above 6% DSPE-PEG-PDP concentration is consistent with prior results.

DSPE-PEG in hydro soy PC (HSPC) vesicles was found to undergo the mushroom to brush transition at a concentration of 6 mol%.[42] Fluorescence recovery after photobleaching results of 8% DOPE-PEG LBM showed no recovery.[41] It is well known that PEG polymers undergo a mushroom-to-brush transition when the surface density increases beyond the Flory radius. The Flory radius of polymer is given by:[59]

$$R_F = a \cdot N^{3/5} \qquad (3)$$

where *a* is the length of a subunit and N is the number of subunits. The DSPE-PEG-PDP molecule used in this study has 45 PEG subunits with length of approximately 3.5 Å.[60] Thus, R_F is calculated as 3.4 nm for PEG in DSPE-PEG-PDP. In order to estimate the surface density as a function of DSPE-PEG-PDP concentration in tLBMs, de Gennes theory[61] is used where the average distance between grafting sites (D) is governed by:

$$D = \left(\frac{A}{f}\right)^{1/2} \qquad (4)$$

A is the mean molecular area and f is the mol fraction of DSPE-PEG-PDP lipids in the tLBM. The mean molecular area for a POPC lipid is approximately in the range of 50 - 70 $Å^2$.[60] When D is greater than R_F, PEG chains are predicted to be in a random coil conformation (mushroom phase) with PEG chain length (L) equal to R_F (3.4 nm); while when D is less than R_F, PEG groups are predicted to be in an extended conformation (brush phase) due to lateral repulsion.[62] From equation (4), the PEG mushroom to brush transition would be expected to occur at DSPE-PEG-PDP concentration of 4.3% – 6.1%. Therefore, at the DSPE-PEG-PDP concentration less than or equal to approximately 6%, one would expect the PEG chain to be in the mushroom regime. The AFM force spectroscopy data clearly reflects this transition and narrows down the composition where it occurs as there is an abrupt increase in E above 6% concentration. The

consistent increased E values of tLBMs at 8% and 10% DSPE-PEG-PDP concentration indicate that the PEG polymer chain conformation can dominate tLBM stiffness. Note that the values listed for the onset compression distance do not include the polymer brush on the surface of tLBMs as the characteristic interaction between an AFM tip and polymer brush is in the exponential term of the repulsive interaction.[53] Thus we would only expect small changes in onset compression distance values with the mushroom to brush transition that is within experimental and fitting error. We do see a very slight increase in the breakthrough distance at 10% DSPE-PEG-PDP (4.8 ± 0.6 nm) than lower concentrations such as 8% (4.4 ± 0.8 nm) as the more closely packed PEG groups may become constrained and exhibit a different interaction with the AFM tip. Analysis of dense PEG brushes on Au surfaces found an increase in stiffness within 5 nm of the surface and a deviation from the exponential decay of the repulsive force predicted in de Gennes theory to quadratic behavior in this regime.[53] This would explain why the onset compression distances do not vary significantly. The semilog plots of force-separation in **Figure 16**c and **Figure 16**d, for 8% and 10% DSPE-PEG-PDP concentration clearly show a increase in the magnitude of the long range repulsive force as a signature of PEG groups in the brush phase.[57]

At DSPE-PEG-PDP concentration of 24%, E further increases to 16.7 ± 0.8MPa indicating another phase transition. This observed stiffening at 24 % DSPE-PEG-PDP concentration is consistent with a structural transition. The AFM topography and force spectroscopy data where a change in the morphology and breakthrough distance, respectively, of this membrane as compared to other membranes with differing DSPE-PEG-PDP concentrations are observed is also consistent with a structural transition. Edwards et al., using transmission electron microscopy (TEM), observed the structural transition of PEG-grated vesicles from a lamellar

(liposome) structure to a disk-like structure, so called bilayer disk, above 10 mol% PEG.[63] This transition from vesicles to micelles has been also observed in vesicles composed of DSPE/PEG[64] and DSPC/PEG (2000)[65] at PEG concentrations of 15-20 % in solution. Johnsson et al. using cryogenic TEM measured a transition from vesicles to a discoidal micelle structure dominates near 20% PEG-lipid concentration.[66] The authors determined by correlating TEM and dynamic light scattering data with a 'mixed-disk' model[67] that PEG appears to segregate to the edges to stabilize the edges.[66,67] The irregular boundaries of POPC membranes with 24 % DSPE-PEG-PDP concentration observed in the AFM topography data of **Figure 15**f are consistent with segregation of PEG chains to the boundary of membrane domains. Thus, bilayer disk structures containing 24% DSPE-PEG-PDP molecules appear to attach on TS Au via the Au-thiolate bonding. Consistent with prior models of discoidal micelles[66,67] and the AFM images of **Figure 15** and measured breakthrough distances for 24% DSPE-PEG-PDP, PEG chains appear to segregate to the disk rims; the total estimated membrane thickness with of such a structure would be 7.3 nm which is consistent with the onset compression thickness determined using AFM force spectroscopy.

Figure 19 is a schematic illustration of structures of (a) untethered and (b-c) tethered LBM with varied DSPE-PEG-PDP concentrations based on the above analysis. **Figure 19**a illustrates a POPC LBM sitting on mica substrate with a thin water layer in between. The proposed structure of tLBMs with DSPE-PEG-PDP concentration between 2.5% and 6% is shown in **Figure 19**b where DSPE-PEG-PDP, with PEG chains in mushroom phase is present on both sides of the tLBM. The structure of tLBM composed of 8% DSPE-PEG-PDP/92% POPC and 10% DSPE-PEG-PDP/90% POPC (**Figure 19**c) has a similar structure as shown in **Figure 19**b, with the only difference being that PEG chains are in the brush conformation. When the DSPE-PEG-PDP

concentration was increased to 24%, **Figure 19**d illustrates bilayer disks that attach to the TS Au substrate from solution where the DSPE-PEG-PDP molecules segregate to the rim of the disk. The proposed tLBM structures are in good agreement with the topography, relative onset compression thicknesses, and the fitted Young's modulus.

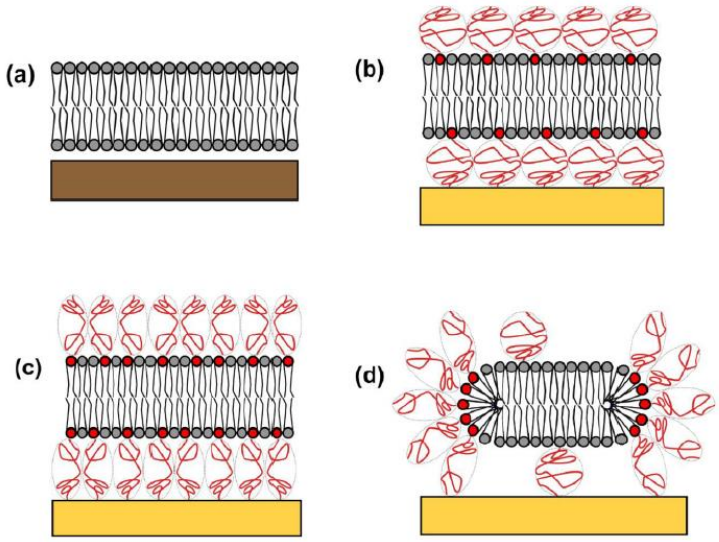

Figure 19: Schematic illustration of tLBM structures with lipid composition of (a) 100% POPC; (b) 1–6% DSPE-PEG-PDP/99–95% POPC; (c) 8–10% DSPE-PEG-PDP/92–90% POPC and (d) 24% DSPE-PEG-PDP/76% POPC.

Conclusion

In this study, Young's moduli (E) of tLBMs as a function of DSPE-PEG-PDP tethering molecule concentration are determined using AFM topography and analysis of AFM force spectroscopy data. Incorporating a polymer cushion layer, PEG, between POPC LBM and the solid substrate significantly decreases tLBM stiffness comparing to solid supported POPC LBM. The lowest tLBM stiffness appears to be correlated with disorder near the PEG mushroom to brush phase transition at 6 mol%. There is an abrupt increase in E after the mushroom to brush phase

transition occurs due to increased PEG grafting density. At 24% DSPE-PEG-PDP, tLBM structure appears to change to a flattened micelle disk on the Au substrates and this phase transition is also reflected in an increase in E. The variation of E, determined from fitting the Sneddon model and the BECC model follow the same qualitative trend. Yet the BECC model yield lower values for E, alleviating the contribution of the hard substrate underneath the tLBM, and reflects the variation of E with the phase transitions more clearly. In addition to providing a systematic method to study local mechanical properties of biological membranes with sharp AFM tips, this study also provides a tLBM platform with controllable membrane rigidity, which could be used as cell model to study mechanosensitive protein/peptide-membrane interactions as a function of membrane mechanical properties. This study demonstrates that AFM force spectroscopy alongside appropriate analysis can be used to determine mechanical properties of biological membranes. Methods to determine local mechanical properties will aid future studies such as understanding how this parameter affects regulation of transmembrane proteins.

References

[1] A. A. Brian, H. M. McConnell, *Proc. Natl. Acad. Sci.* **1984**, *81*, 6159.

[2] M. Stelzle, E. Sackmann, *Biochim. Biophys. Acta BBA - Biomembr.* **1989**, *981*, 135.

[3] H. M. McConnell, T. H. Watts, R. M. Weis, A. A. Brian, *Biochim. Biophys. Acta BBA - Rev. Biomembr.* **1986**, *864*, 95.

[4] C. Dietrich, R. Tampé, *Biochim. Biophys. Acta BBA - Biomembr.* **1995**, *1238*, 183.

[5] B. A. Cornell, V. L. B. Braach-Maksvytis, L. G. King, P. D. J. Osman, B. Raguse, L. Wieczorek, R. J. Pace, *Nature* **1997**, *387*, 580.

[6] C. A. Naumann, O. Prucker, T. Lehmann, J. Rühe, W. Knoll, C. W. Frank, *Biomacromolecules* **2002**, *3*, 27.

[7] M. Kühner, R. Tampé, E. Sackmann, *Biophys. J.* **1994**, *67*, 217.

[8] M. L. Wagner, L. K. Tamm, *Biophys. J.* **2000**, *79*, 1400.

[9] F. Albertorio, A. J. Diaz, T. Yang, V. A. Chapa, S. Kataoka, E. T. Castellana, P. S. Cremer, *Langmuir* **2005**, *21*, 7476.

[10] J. C. Munro, C. W. Frank, *Langmuir* **2004**, *20*, 10567.

[11] X. Wang, M. M. Shindel, S.-W. Wang, R. Ragan, *Langmuir* **2010**, *26*, 18239.

[12] A. Sumino, T. Dewa, T. Takeuchi, R. Sugiura, N. Sasaki, N. Misawa, R. Tero, T. Urisu, A. T. Gardiner, R. J. Cogdell, H. Hashimoto, M. Nango, *Biomacromolecules* **2011**, *12*, 2850.

[13] P. M. Nair, K. Salaita, R. S. Petit, J. T. Groves, *Nat. Protoc.* **2011**, *6*, 523.

[14] D. Huang, T. Zhao, W. Xu, T. Yang, P. S. Cremer, *Anal. Chem.* **2013**, *85*, 10240.

[15] M. Bally, M. Graule, F. Parra, G. Larson, F. Höök, *Biointerphases* **2013**, *8*, 4.

[16] X. Wang, M. M. Shindel, S.-W. Wang, R. Ragan, *Langmuir* **2012**, *28*, 7417.

[17] D. Marsh, *Biophys. J.* **2007**, *93*, 3884.

[18] O. H. Samuli Ollila, T. Róg, M. Karttunen, I. Vattulainen, *J. Struct. Biol.* **2007**, *159*, 311.

[19] M. F. Brown, *Biochemistry (Mosc.)* **2012**, *51*, 9782.

[20] N. Maftouni, M. Amininasab, M. R. Ejtehadi, F. Kowsari, R. Dastvan, *J. Chem. Phys.* **2013**, *138*, 065101.

[21] A. T. Clay, F. J. Sharom, *Biochemistry (Mosc.)* **2013**, *52*, 343.

[22] T. Nomura, C. G. Cranfield, E. Deplazes, D. M. Owen, A. Macmillan, A. R. Battle, M. Constantine, M. Sokabe, B. Martinac, *Proc. Natl. Acad. Sci.* **2012**, *109*, 8770.

[23] S. M. Olsen, J. D. Stover, J. Nagatomi, *Ann. Biomed. Eng.* **2011**, *39*, 688.

[24] M. Lekka, P. Laidler, D. Gil, J. Lekki, Z. Stachura, A. Z. Hrynkiewicz, *Eur. Biophys. J.* **1999**, *28*, 312.

[25] M. Lekka, K. Pogoda, J. Gostek, O. Klymenko, S. Prauzner-Bechcicki, J. Wiltowska-Zuber, J. Jaczewska, J. Lekki, Z. Stachura, *Micron* **2012**, *43*, 1259.

[26] M. Prabhune, G. Belge, A. Dotzauer, J. Bullerdiek, M. Radmacher, *Micron* **2012**, *43*, 1267.

[27] H.-J. Butt, E. K. Wolff, S. A. C. Gould, B. Dixon Northern, C. M. Peterson, P. K. Hansma, *J. Struct. Biol.* **1990**, *105*, 54.

[28] E. L. Florin, V. T. Moy, H. E. Gaub, *Science* **1994**, *264*, 415.

[29] J. te Riet, A. J. Katan, C. Rankl, S. W. Stahl, A. M. van Buul, I. Y. Phang, A. Gomez-Casado, P. Schön, J. W. Gerritsen, A. Cambi, A. E. Rowan, G. J. Vancso, P. Jonkheijm, J. Huskens, T. H. Oosterkamp, H. Gaub, P. Hinterdorfer, C. G. Figdor, S. Speller, *Ultramicroscopy* **2011**, *111*, 1659.

[30] M. Duman, M. Pfleger, R. Zhu, C. Rankl, L. A. Chtcheglova, I. Neundlinger, B. L. Bozna, B. Mayer, M. Salio, D. Shepherd, P. Polzella, M. Moertelmaier, G. Kada, A. Ebner, M. Dieudonne, G. J. Schütz, V. Cerundolo, F. Kienberger, P. Hinterdorfer, *Nanotechnology* **2010**, *21*, 115504.

[31] S. Li, F. Eghiaian, C. Sieben, A. Herrmann, I. A. T. Schaap, *Biophys. J.* **2011**, *100*, 637.

[32] A. Calò, D. Reguera, G. Oncins, M.-A. Persuy, G. Sanz, S. Lobasso, A. Corcelli, E. Pajot-Augy, G. Gomila, *Nanoscale* **2014**, *6*, 2275.

[33] A. Alessandrini, P. Facci, *Micron* **2012**, *43*, 1212.

[34] E. K. Dimitriadis, F. Horkay, J. Maresca, B. Kachar, R. S. Chadwick, *Biophys. J.* **2002**, *82*, 2798.

[35] R. Wagner, R. Moon, J. Pratt, G. Shaw, A. Raman, *Nanotechnology* **2011**, *22*, 455703.

[36] M. E. McConney, S. Singamaneni, V. V. Tsukruk, *Polym. Rev.* **2010**, *50*, 235.

[37] I. N. Sneddon, *Int. J. Eng. Sci.* **1965**, *3*, 47.

[38] N. Gavara, R. S. Chadwick, *Nat. Nanotechnol.* **2012**, *7*, 733.

[39] W. Ngwa, K. Chen, A. Sahgal, E. V. Stepanov, W. Luo, *Thin Solid Films* **2008**, *516*, 5039.

[40] S. L. Crick, F. C.-P. Yin, *Biomech. Model. Mechanobiol.* **2007**, *6*, 199.

[41] S. Kaufmann, O. Borisov, M. Textor, E. Reimhult, *Soft Matter* **2011**, *7*, 9267.

[42] O. Garbuzenko, Y. Barenholz, A. Priev, *Chem. Phys. Lipids* **2005**, *135*, 117.

[43] M. J. Hope, M. B. Bally, G. Webb, P. R. Cullis, *Biochim. Biophys. Acta BBA - Biomembr.* **1985**, *812*, 55.

[44] S. Lee, S.-S. Bae, G. Medeiros-Ribeiro, J. J. Blackstock, S. Kim, D. R. Stewart, R. Ragan, *Langmuir* **2008**, *24*, 5984.

[45] J. L. Hutter, J. Bechhoefer, *Rev. Sci. Instrum.* **1993**, *64*, 1868.

[46] M. Hegner, P. Wagner, G. Semenza, *Surf. Sci.* **1993**, *291*, 39.

[47] R. Ragan, D. Ohlberg, J. J. Blackstock, S. Kim, R. S. Williams, *J. Phys. Chem. B* **2004**, *108*, 20187.

[48] M. Li, M. Chen, E. Sheepwash, C. L. Brosseau, H. Li, B. Pettinger, H. Gruler, J. Lipkowski, *Langmuir* **2008**, *24*, 10313.

[49] H.-J. Butt, R. Stark, *Colloids Surf. Physicochem. Eng. Asp.* **2005**, *252*, 165.

[50] S. Ip, J. K. Li, G. C. Walker, *Langmuir* **2010**, *26*, 11060.

[51] N. Kučerka, M.-P. Nieh, J. Katsaras, *Biochim. Biophys. Acta BBA - Biomembr.* **2011**, *1808*, 2761.

[52] L. Janosi, A. A. Gorfe, *J. Chem. Theory Comput.* **2010**, *6*, 3267.

[53] G. Stan, F. W. DelRio, R. I. MacCuspie, R. F. Cook, *J. Phys. Chem. B* **2012**, *116*, 3138.

[54] F. A. Heberle, R. S. Petruzielo, J. Pan, P. Drazba, N. Kučerka, R. F. Standaert, G. W. Feigenson, J. Katsaras, *J. Am. Chem. Soc.* **2013**, *135*, 6853.

[55] T. M. Bayerl, M. Bloom, *Biophys. J.* **1990**, *58*, 357.

[56] B. W. Koenig, S. Krueger, W. J. Orts, C. F. Majkrzak, N. F. Berk, J. V. Silverton, K. Gawrisch, *Langmuir* **1996**, *12*, 1343.

[57] N. Backmann, N. Kappeler, T. Braun, F. Huber, H.-P. Lang, C. Gerber, R. Y. H. Lim, *Beilstein J. Nanotechnol.* **2010**, *1*, 3.

[58] L. Picas, F. Rico, S. Scheuring, *Biophys. J.* **2012**, *102*, L01.

[59] P. J. Flory, *Principles of Polymer Chemistry*, Cornell University Press, **1953**.

[60] A. K. Kenworthy, K. Hristova, D. Needham, T. J. McIntosh, *Biophys. J.* **1995**, *68*, 1921.

[61] P. G. de Gennes, *Adv. Colloid Interface Sci.* **1987**, *27*, 189.

[62] P. G. de Gennes, *Macromolecules* **1980**, *13*, 1069.

[63] K. Edwards, M. Johnsson, G. Karlsson, M. Silvander, *Biophys. J.* **1997**, *73*, 258.

[64] L. M. Ickenstein, M. C. Arfvidsson, D. Needham, L. D. Mayer, K. Edwards, *Biochim. Biophys. Acta BBA - Biomembr.* **2003**, *1614*, 135.

[65] K. Hristova, A. Kenworthy, T. J. McIntosh, *Macromolecules* **1995**, *28*, 7693.

[66] M. Johnsson, K. Edwards, *Biophys. J.* **2003**, *85*, 3839.

[67] N. A. Mazer, G. B. Benedek, M. C. Carey, *Biochemistry (Mosc.)* **1980**, *19*, 601.

CHAPTER V: Graphene-Derived Devices

Graphene, a one-atom-thick structure of carbon atoms arrayed in a honeycomb lattice, is the first two-dimensional crystal to be studied. Its electronic properties were theoretically studied as early as 1947 by Wallace using tight-binding calculations[14], and graphene grown by chemical vapor deposition and carbon segregation were also characterized in the following decades[15–19]. This early work identified some of graphene's physical characteristics such as it being a zero-gap semiconductor, but research interest was tempered by the prevailing misconception that two-dimensional metals are thermodynamically unstable, and are thus not suitable for practical applications (See Peierls[20], Landau[21], and Fradkin[22]). In 2004, Geim and Novoselov isolated monolayer graphene flakes from bulk graphite by mechanical exfoliation in ambient conditions[23], leaving little doubt as to the stability of isolated graphene's crystal structure. After this, commercial and scientific interest in graphene surged as researchers endeavored to take advantage of its numerous unique properties, including its high electron mobility at room-temperature, high thermal conductivity, extremely high tensile strength, and near impermeability. Graphene is now a heavily researched material with applications in lightweight materials, nanoelectronics, energy storage, chemical filtering, and more[23–31].

This chapter will introduce the reader to the properties of graphene relevant to this thesis. First, a simplified model of graphene's band structure is derived using a tight-binding description. Various techniques to modify the properties of graphene are then discussed. Some of the more common graphene synthesis methods are then presented, followed by a brief discussion of methods for creating modified graphene systems. Finally, there is a description of the current

state of graphene applied to three-dimensional applications in heterogeneous catalysis and gas sensing.

Tight-Binding Description of Graphene's Electronic Structure

To form graphene's electronic structure, the four valence electrons of each carbon atom form three sp2 bonding orbitals oriented in a plane and the remaining out-of-plane 2p orbital stays unhybridized. Because of the orthogonality between these orbitals, two separate band structures are formed from valence electrons in a graphene lattice: One corresponds to the sp2-derived σ bonds, and the other corresponds to the 2p-derived π orbitals. A large energy gap of more than 12 eV exists at the Γ-point between the sp2-derived conduction (σ*) and valence (σ) bands. These bands are largely irrelevant to electronic applications of graphene due to this large gap, but they are responsible for its mechanical strength. The π-orbitals in adjacent carbon sites overlap to form a delocalized electron cloud with π* and π energy bands which cross at six points in the Brillouin zone (making graphene a zero-bandgap semiconductor) and have a linear dispersion relation near the Fermi energy. This leads to some of its more exotic electronic behavior, such as massless Dirac fermions. To derive the primary low-energy behavior of graphene, a nearest-neighbor tight-binding description of graphene will now be presented, following closely the derivation given in *Introduction to Graphene-Based Nanomaterials: From Electronic Structure to Quantum Transport*[32].

Consider a lattice of carbon atoms, consisting of a simple hexagonal Bravais lattice in two dimensions with a basis of two atoms. In terms of the carbon-carbon bond length a_{cc}, the lattice parameter of the graphene lattice is $a = \sqrt{3}a_{cc}$. Considering that p_z orbitals make up the

relevant electronic structure of graphene, one can construct an *ansatz* for the total electron energy eigenfunction as a linear combination of Bloch sums for each sublattice:

$$\Psi(\boldsymbol{k},\boldsymbol{r}) = c_A(\boldsymbol{k})\tilde{p}_z^A(\boldsymbol{k},\boldsymbol{r}) + c_B(\boldsymbol{k})\tilde{p}_z^B(\boldsymbol{k},\boldsymbol{r}), \quad 27$$

and

$$\tilde{p}_z^{A/B}(\boldsymbol{k},\boldsymbol{r}) = \frac{1}{\sqrt{N_{cells}}}\sum_j e^{i\,\boldsymbol{k}\cdot\boldsymbol{R}_j}\; p_z\big(\boldsymbol{r} - \boldsymbol{r}_{A/B} - \boldsymbol{R}_j\big), \quad 28$$

where $\boldsymbol{k}$ is the electron's wave vector, $\boldsymbol{r}$ is the position in real space, $\boldsymbol{r}_{A/B}$ is the position of basis sites A or B within the Wigner Seitz cell, $\boldsymbol{R}_j$ are the Bravais lattice points, and p_z is the wave function for a p_z orbital. If we neglect the overlap $\langle p_z^A | p_z^B \rangle$ between nearest-neighbor orbitals, the Schrodinger equation for this system becomes a 2×2 eigenvalue problem:

$$\begin{bmatrix} \widehat{H_{AA}}(\boldsymbol{k}) & \widehat{H_{AB}}(\boldsymbol{k}) \\ \widehat{H_{BA}}(\boldsymbol{k}) & \widehat{H_{BB}}(\boldsymbol{k}) \end{bmatrix} \begin{bmatrix} c_A(\boldsymbol{k}) \\ c_B(\boldsymbol{k}) \end{bmatrix} = E(\boldsymbol{k}) \begin{bmatrix} c_A(\boldsymbol{k}) \\ c_B(\boldsymbol{k}) \end{bmatrix}, \quad 29$$

where

$$\widehat{H_{AA}}(\boldsymbol{k}) = \frac{1}{\sqrt{N_{cells}}}\sum_{i,j} e^{i\,\boldsymbol{k}\cdot(\boldsymbol{R}_j - \boldsymbol{R}_i)} \left\langle p_z^{A,\boldsymbol{R}_i} \middle| \widehat{H} \middle| p_z^{A,\boldsymbol{R}_j} \right\rangle, \quad 30$$

and

$$\widehat{H_{AB}}(\boldsymbol{k}) = \frac{1}{\sqrt{N_{cells}}}\sum_{i,j} e^{i\,\boldsymbol{k}\cdot(\boldsymbol{R}_j - \boldsymbol{R}_i)} \left\langle p_z^{A,\boldsymbol{R}_i} \middle| \widehat{H} \middle| p_z^{B,\boldsymbol{R}_j} \right\rangle. \quad 31$$

Here we have introduced the abbreviated notation $p_z^{A/B,\boldsymbol{\tau}} = p_z(r - r_{A/B} - \boldsymbol{\tau})$. These two expressions describe the Hamiltonian matrix completely since $\widehat{H_{AA}}(\boldsymbol{k}) = \widehat{H_{BB}}(\boldsymbol{k})$ and $\widehat{H_{AB}}(\boldsymbol{k}) = \widehat{H_{BA}^*}(\boldsymbol{k})$. These expressions can be simplified by only considering first-nearest-neighbors, where the sum $\widehat{H_{AB}}(\boldsymbol{k})$ simplifies to,

$$\widehat{H_{AB}}(\boldsymbol{k}) = \left\langle p_z^{A,0}\middle|\widehat{H}\middle|p_z^{B,0}\right\rangle + e^{-i\,\boldsymbol{k}\cdot\boldsymbol{a}_1}\left\langle p_z^{A,\boldsymbol{R}_i}\middle|\widehat{H}\middle|p_z^{B,-a_1}\right\rangle + \quad (32)$$

$$e^{-i\,\boldsymbol{k}\cdot\boldsymbol{a}_2}\left\langle p_z^{A,\boldsymbol{R}_i}\middle|\widehat{H}\middle|p_z^{B,-\boldsymbol{a}_2}\right\rangle$$

$$= -\gamma_0\,\alpha(\boldsymbol{k}),$$

where γ_0 is the transfer integral between first neighbor π orbitals, which has typical values between 2.9eV and 3.1eV[32,33]. The function $\alpha(\boldsymbol{k})$ is given by

$$\alpha(\boldsymbol{k}) = 1 + e^{-i\,\boldsymbol{k}\cdot\boldsymbol{a}_1} + e^{-i\,\boldsymbol{k}\cdot\boldsymbol{a}_2}. \quad (33)$$

With this notation in mind, we may change our energy reference so that the diagonal matrix elements are of zero energy, $\widehat{H_{AA}}(\boldsymbol{k}) = \widehat{H_{BB}}(\boldsymbol{k}) = \left\langle p_z^{A,0}\middle|\widehat{H}\middle|p_z^{A,0}\right\rangle = 0$, and the Hamiltonian becomes:

$$\widehat{H}(\boldsymbol{k}) = \begin{bmatrix} 0 & -\gamma_0\,\alpha(\boldsymbol{k}) \\ -\gamma_0\,\alpha^*(\boldsymbol{k}) & 0 \end{bmatrix}. \quad (34)$$

Diagonalizing this matrix gives the energy dispersion relation for the π band:

$$E_{\pm}(\boldsymbol{k}) = \pm\gamma_0\,|\alpha(\boldsymbol{k})| \quad (35)$$

$$= \pm\gamma_0\sqrt{3 + 2\cos(\boldsymbol{k}\cdot a_1) + 2\cos(\boldsymbol{k}\cdot a_2) + 2\cos(\boldsymbol{k}\cdot(a_2 - a_1))}$$

Figure 20(a) illustrates this dispersion relation. We see that the valence and conduction bands meet at six points in the first Brillouin zone. Furthermore, series expansion around these high-symmetry points $\boldsymbol{K}_{\pm} = \frac{4\pi}{3a}\left(\frac{\sqrt{3}}{2}, \mp\frac{1}{2}\right)$ gives:

$$E_{\pm}(\boldsymbol{k}) = \pm\gamma_0 \left\{\left(\frac{3}{4}a^2\left(\boldsymbol{k}_y - \boldsymbol{K}_{+,y}\right)^2 + O\left[\boldsymbol{k}_y - \boldsymbol{K}_{+,y}\right]^3\right)\right. \quad (36)$$

$$+ \left(\frac{3a^2}{4} + \frac{3}{8}\sqrt{3}a^3\left(\boldsymbol{k}_y - \boldsymbol{K}_{+,y}\right) - \frac{3}{32}a^4\left(\boldsymbol{k}_y - \boldsymbol{K}_{+,y}\right)^2\right.$$

$$\left.\left. + O\left[\boldsymbol{k}_y - \boldsymbol{K}_{+,y}\right]^3\right)\left(\boldsymbol{k}_x - \boldsymbol{K}_{+,x}\right)^2\right.$$

$$\left. + O\left[\boldsymbol{k}_x - \boldsymbol{K}_{+,x}\right]^3\right\}^{1/2}$$

$$\cong \pm\gamma_0 \left\{\left(\frac{3}{4}a^2\left(\left(\boldsymbol{k}_x - \boldsymbol{K}_{+,x}\right)^2 + \left(\boldsymbol{k}_y - \boldsymbol{K}_{+,y}\right)^2\right)\right)\right\}^{1/2}$$

$$= \pm\frac{\sqrt{3}}{2}a\,\gamma_0|\delta\boldsymbol{k}| = \pm\hbar\, v_F|\delta\boldsymbol{k}|,$$

Where v_F is known as the electronic group velocity and $\delta\boldsymbol{k}$ is the position in reciprocal space relative to a $\boldsymbol{K}$ point. Thus, for small deviations from the points $\boldsymbol{K}_{\pm}$, the energy dispersion relation is linear (See **Figure 20**(b)). This important result emerges from the symmetric bipartite lattice structure in graphene, and echoes the linear energy dispersion relation of massless Dirac fermions with an effective "speed of light" $v_F \cong 8.5 \times 10^5$m/s. For this reason, the symmetry points $\boldsymbol{K}_{\pm}$ are known as Dirac points, and the low-energy behavior around these points is responsible for much of the unique electronic behavior of graphene crystals.

For instance, the presence of a magnetic field causes massless Dirac fermions to have quantized cyclotron orbits, creating a discrete set of energy levels known as Landau levels[34,35]. Unlike other systems, however, Dirac fermions have Landau levels that are not evenly spaced and there is a level at zero energy, which leads to equal populations of holes and electrons at the Fermi level and hence explains the observation of the integer Quantum Hall effect[25,35,36]. Another consequence of massless particles is the Klein paradox[37]. When a relativistic particle impinges on an atomically smooth potential barrier, the probability of transmission is nearly 100%, making potential barriers such as charge puddles effectively transparent. This phenomenon helps to explain the very high charge mobility in graphene even at varying temperatures[38]

From the electronic dispersion, we may also compute the density of states, defined as:

$$D(E) = \iint \delta\left(E - E_{\pm}(\boldsymbol{k})\right) d\boldsymbol{k}, \qquad 37$$

where the integral is over the first Brillouin zone. The density of states is shown in **Figure 20**(c), where we see that the density of electronic states goes to zero near the Fermi level and does not have an energy gap.

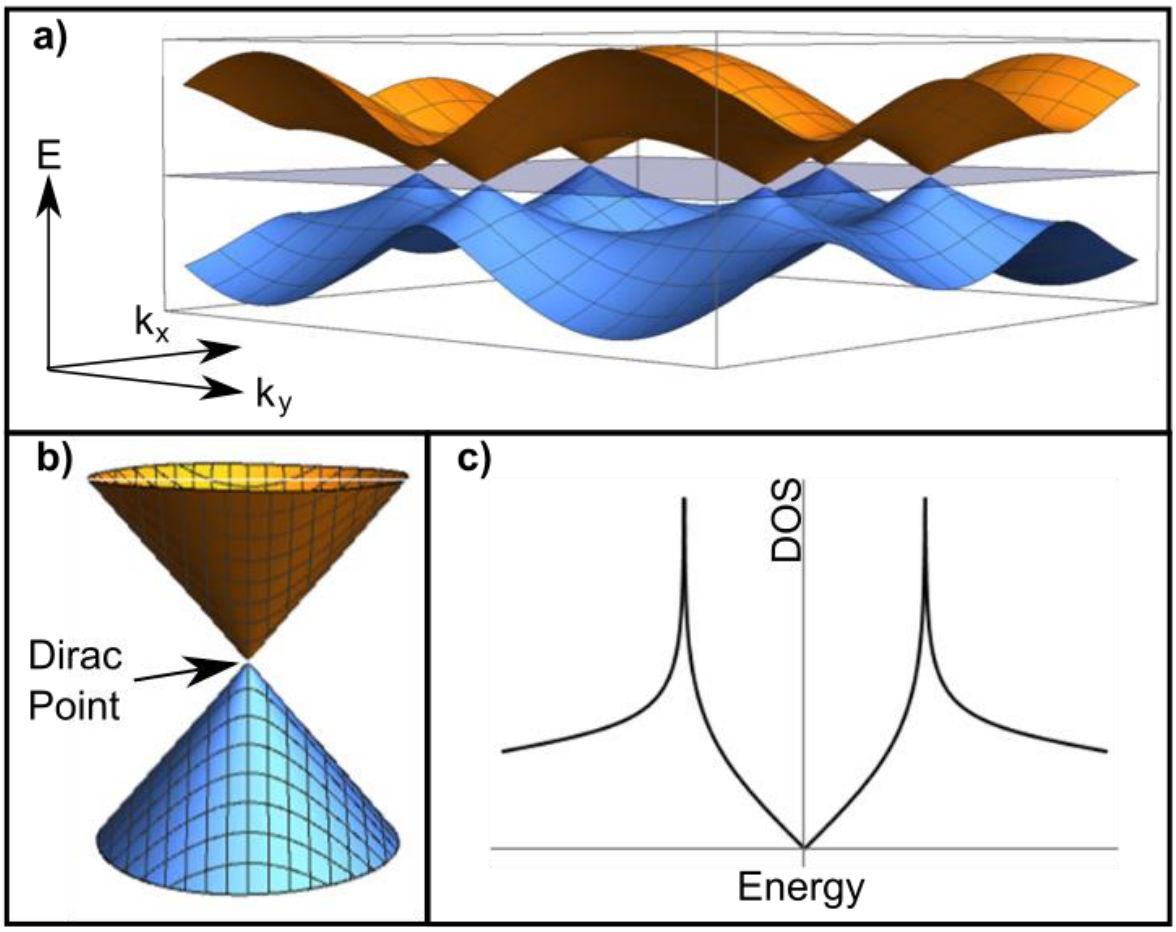

Figure 20) Electronic dispersion and density of states of monolayer graphene: Electronic dispersion near the first Brillouin zone (a) and zoomed in near a high-symmetry "K-point" or "Dirac point" (b) of a simplified graphene system, along with the corresponding density of states plot (c).

Modification of Graphene

Graphene's strength and extremely high group velocity make it attractive for various fields, but *pristine* graphene is not necessarily suited for applications such as graphene transistors or catalysts. The electronic structure of graphene is responsible for this since the vanishing

density of states near the Dirac points and the lack of bandgap are undesirable properties for certain applications such as nanoelectronics. The low density of charge carriers inhibits the conductivity of pristine graphene and reduces charge transfer to adsorbed species. Simultaneously, the lack of a band gap causes leakage current in graphene transistors, hampering efforts to create graphene-based electronics. Both issues can be addressed by various forms of graphene modification.

Modification by Doping

Doping, one of the most explored methods of graphene modification, is the process of introducing impurities into a crystal lattice to manipulate its electrical properties. When a material is doped, carriers (electrons or holes) are introduced to the crystal, which has several effects on the crystal's properties. First, since the carrier concentration is increased, the bulk conductivity is also generally increased. Doping also shifts the charge neutrality level relative to the vacuum level and can introduce new electronic states, allowing for the tailoring of a crystal's properties.

There are numerous doping approaches that have been used to modify graphene to introduce carriers and shift the charge neutrality point. Heteroatom dopants incorporated into the graphene lattice are one widely used method. Nitrogen doping has been studied extensively to introduce n-type doping in graphene, and has been demonstrated to effectively tune graphene's band gap, to introduce accessible electronic states near the Dirac point, and to shift the charge neutrality level[31,39–43]. Nitrogen-doped graphene has even been shown to catalyze the oxygen reduction reaction efficiently[44,45] without the presence of expensive noble metals. Other heteroatom dopants have also been used, the most common being Sulfur[46–48], Boron[49,50], and

Phosphorous[51,52], giving a variety of different dopant species to fine-tune graphene's density of states near the Dirac points for specific applications. More than just modifying conductivity and catalytic activity, some of these same heteroatom dopants have also been found to introduce appreciable bandgaps, with particular success with dual-doping[53]. Other dopant species (Si and Si/Al) have resulted in band gaps large enough for room-temperature graphitic electronic devices to be feasible[54,55].

In addition to heteroatom dopants, various other techniques have been demonstrated to dope graphene. Defect doping is one of the most commonly used doping methods for graphene. Lattice defects can lead to modulation in the magnetic susceptibility of graphene and self-doping effects[13,56], with divacancies being one of the most frequently studied defect species[57,58]. Besides defect doping, interface engineering[59], carefully adjusted substrate interactions[60] and even merely being in contact with metal substrates[61] have been found to modulate the doping of graphene to introduce bandgaps, adjust carrier density, and shift the work function. Doping via adsorption has also proven to be effective at tuning graphene's band structure. Monolayer graphene on Ir(111) gains an appreciable bandgap when treated with hydrogen[62], and noncovalent functionalization of graphene with tetrafluorotetracyanoquinodimethane[63] and with benzyl viologen[64] has been demonstrated to shift the charge neutrality level and modulate the bandgap.

Layer Engineering: Bi-, Few-, and Multi-Layer Graphene

Bulk graphites have unique electronic properties distinct from graphene, and are strongly dependent on the number of layers and the stacking geometry between layers[32]. Bilayer, few-layer, and multilayer graphene have properties reminiscent of both bulk graphites and single-

layer graphene, and there has been much research interest in these systems as tunable graphene systems. For instance, bilayer graphene has exhibited an electrostatically tunable band gap[65], and DFT calculations have suggested that phosphorous-doped bilayer graphene exhibits an appreciable bandgap and a reduced formation energy when compared to the analogous single-layer system[54], making it a promising semiconductor for electronics applications. Bilayer graphene with AB stacking (Bernal stacking) is of particular interest for bandgap engineering due to its breaking of single layer graphene's inversion symmetry[66]. Few-layer graphene's properties are especially sensitive to stacking configuration. For instance, the two most common stacking orders for 3-layer graphene, AB-stacked and ABC-stacked, have distinct band structures. AB-stacked 3-layer graphene's band structure near the Fermi level consists of overlapping linear and quadratic bands[67] and is metallic for all applied fields[68], while ABC-stacked 3-layer graphene has a cubic dispersion relation near the Fermi level[69] and exhibits an electrostatically tunable bandgap similar to that of bilayer graphene[70]. As the number of layers increases and the layer-layer interactions change, many different band configurations become possible. These variations in the band structure of thin graphene systems therefore makes layer engineering a powerful tool to tune their properties and optimize them for specific applications.

Graphene Growth

One of the most important challenges in graphene research has been to develop synthesis methods that are cost-effective and scalable while still producing high quality graphene. Currently the "Scotch tape method" of mechanical exfoliation used by Geim and Novoselov in 2004 remains the standard for obtaining high-quality defect-free graphene sheets. With this technique, adhesive tape is applied to a piece of highly oriented pyrolytic graphite (HOPG) and

peeled off, and additional pieces of tape are used to repeatedly strip layers from the graphite adhered to the tape eventually leaving single- to few-layer graphene. Graphite's very weak binding energy between graphitic planes allows for mechanical exfoliation to work, allowing for individual sheets of graphene to be isolated from bulk graphite with very few defects. The time-consuming and labor-intensive nature of this process makes mechanical exfoliation of HOPG not scalable for use in industry[71].

Chemical vapor deposition (CVD) is currently the most widely investigated method of synthesizing graphene as it is inexpensive and scalable[72]. In CVD, a metal substrate (e.g. a transition metal such as Cu or Ni) is heated in a vacuum furnace, and carbon-containing gas species are fed in, which then decompose to carbon radicals at the metal surface and form graphene. The decomposition of the carbon precursor in CVD deposition is a nontrivial process, requiring several steps. For instance, methane (CH_4) is the simplest hydrocarbon, and it decomposes as:

$$CH_4(g) + (s) \rightarrow CH_3(s) + H(s) \qquad 38$$

$$CH_3(s) + (s) \rightarrow CH_2(s) + H(s)$$

$$CH_2(s) + (s) \rightarrow CH(s) + H(s)$$

$$CH(s) \rightarrow C(s) + H(s).$$

The metal surface is an essential catalyst in this process, especially for the dissociative chemisorption of CH_4 on the solid surface, which is the rate limiting step[73,74]. Once carbon radicals are present, graphene is formed as the most energetically favorable bonding configuration of 2-dimensional carbon.

The choice of growth substrate in CVD synthesis is important, because the surface changes the growth process. For instance, consider Cu and Ni, two of the most commonly used

CVD substrates in graphene synthesis[74,75]. The carbon solubility in Cu crystals is very low, meaning that the growth kinetics occur almost solely on the Cu surface.[76] As a result, graphenes grown on Cu surfaces tend to be single-layered, since the graphene films cover up surface sites where carbon precursor decomposition occurs. Conversely, Ni crystals have a high carbon solubility, so graphene grows in a two-step bulk-mediated process wherein carbon atoms are first incorporated into the Ni substrate at elevated temperatures and then the substrate is cooled, decreasing carbon solubility, causing carbon segregation to the surface, forming graphene[77]. Graphenes grown on Ni substrates are more likely to be multi-layer than those grown on Cu because the higher availability of carbon radicals. Differences like these make substrate choice important in CVD graphene synthesis.

Additional methods of graphene synthesis have also been reported, though they are less widespread. Solid precursors such as poly-methyl-methacrylate (PMMA), fluorene ($C_{13}H_{10}$), and sucrose ($C_{12}H_{22}O_{11}$) have all been used to synthesize graphene[78], and monolayer graphene has been reported using polystyrene as the carbon source[79,80]. Amorphous carbon can be crystallized into graphene on a catalyst substrate as well[81]. Some groups have also reported successful graphene growth using liquid precursors such as hexane[82] and various alcohols[83,84].

Graphene Lattice Modification

There is much innovation in the field of modifying graphene to adjust its properties. To achieve heteroatom doping during CVD graphene synthesis, one method is to incorporate heteroatom dopants into the carbon precursor gas mixture. Notably, nitrogen substitutional defects have been incorporated into CVD graphene on Cu by using a NH_3/CH_4 mixture as the CVD reagent[85]. Annealing graphene in the presence of dopant-containing compounds has also

been investigated. Nitrogen doping has been achieved this way by annealing CVD graphene in NH_3 after N^+ ion irradiation, and sulfur doping has been achieved by annealing pristine graphene in the presence of H_2S gas[46]. Hole doping has been achieved through ion irradiation[86], α-radiation[87], and plasma irradiation[88] on prepared graphene films.

Three-Dimensional Graphene Constructs as Heterogeneous Catalysts and Catalyst Supports

The aim of this thesis is ultimately to produce three-dimensional graphene structures, and a natural application for these structures is as robust supports for catalytic nanoparticles and adatoms. Nearly 90% of all industrially produced chemicals utilized catalysts in their synthesis[89], making catalyst manufacture and design a huge business. Generally, one can classify each catalyst as one of two types: homogeneous and heterogeneous. Homogeneous catalysts are in the same phase as the reactants to be catalyzed. Homogeneous catalysts are an essential part of industrial catalysis, important in various processes including oxidation, hydrogenation, carbonylation, and hydrocyanation among others[90]. The problem with homogeneous catalysts is the difficulty in separating them from the reaction media, which is why industries try to use heterogeneous catalysts when able[91]. A heterogeneous catalyst is in a different phase as the reactants, and can thus be more easily separated from reaction media. This reduces waste and pollution, driving the research into heterogeneous catalysts as part of green chemistry. Conventional heterogeneous catalysts, for instance noble metal nanoparticles, are limited by relatively low activity due to limitations in exposed active sites[91,92]. Heterogeneous catalysts therefore must have very high surface area, and they must be resilient to sintering, clustering, poisoning, and other processes that reduce the catalytically active surface area.

An important method to improve the performance of heterogeneous catalysts is to introduce a support structure on which the catalytically active material binds to maximize available surface area and improve its mechanical properties. Catalyst supports have been in use for decades[93–96], and are now an integral part of many commercially important applications, such as proton exchange membrane fuel cells (PEMFCs)[97], batteries[52,98], and as catalysts for the oxygen reduction reaction (ORR)[99,100] and the oxygen evolution reaction (OER)[100,101]. Currently, supported catalysts suffer from several drawbacks. For instance, Pt nanoparticles supported on carbon supports (e.g. carbon black) are the current "gold standard" for ORR applications, but they suffer from poisoning from reagents as well as fuel crossover effects[102,103]. Additionally, the most common supported catalysts use noble metals, hindering the cost-effectiveness of catalyst systems. Factors such as these are responsible for the recent demand for low-cost, durable, and efficient heterogeneous catalyst systems.

Graphene is particularly attractive in addressing these issues. Its high intrinsic carrier mobility gives the potential for fast charge transport through the catalyst support matrix, and its high electron transfer rate allows for quick charge transfer to analytes, which makes graphene promising in enhancing reaction rates for slow reactions such as the ORR[104]. Additionally, graphene's two-dimensional geometry, strength, and flexibility makes seamless, porous, interconnected graphene structures possible for catalyst support applications[105,106]. These factors, along with the low cost of precursor materials for graphene growth (almost any carbon source can work, including food waste[107]) and reports of modified graphene acting as a metal-free catalyst, have driven considerable research interest to graphene systems as three-dimensional catalysts and catalyst supports.

Still, there are problems with graphene that must be considered in the design and fabrication of graphene-based catalyst supports. For instance, the vanishing density of states near the Dirac points in pristine graphene makes the conductivity prohibitively low, necessitating modifications to increase the carrier density. Grain boundaries also hinder the transport of electrons through bulk graphene, so growth methods must increase graphene grain size or must otherwise mitigate the resistivity introduced by these effects[108–110]. Care must also be taken when synthesizing three-dimensional graphene structures to prevent graphene layer re-stacking[111] and to ensure the stability of the graphene matrix as the analyte flows through.

Three-Dimensional Graphene Constructs as Gas Sensors

Gas sensing is an important field, allowing for the detection of toxic gases for safety applications as well as other sensing applications in industrial, environmental, and military monitoring systems. The last decade has seen a large uptick in the number of publications featuring nanostructured materials for sensing applications[112]. Graphene-based sensors have played no small role in this trend. Carbon materials have long attracted interest for sensing due to their low noise, transduction properties, and detection sensitivity[10,113]. Low-dimensional carbon materials such as graphene, nanotubes, and nanoribbons are of interest due partly to their simplicity, making them good model materials to compare with theory, and partly to their high specific surface area.

Single- to many-layer graphene films are relevant to this dissertation, and gas sensors based on sheet graphene have demonstrated remarkable promise in next-generation gas sensing. The chemiresistive properties of graphene was first investigated by the Novoselov group by measuring changes in Hall resistance due to adsorbed gas molecules[113]. In fact, this study

claims the achievement of single-molecule detection, making graphene sensitive to gas detections in a very wide range of concentrations. Additionally, sensors made from graphene and the closely related reduced graphene oxide have shown high sensitivity to NH_3, NO_2, H_2O, H_2, Cl_2 and CO[8,9,114–118]. The adsorption of many species on graphene is highly dependent on defects and dangling bonds, making surface modification of graphene sensor systems a widely used step in sensor fabrication[10,112]. Types of surface modification include functionalization with polymers, metal decoration, heteroatom doping, and defect doping, and by tailoring the surface chemistry these graphene-based systems can be optimized for specific sensing applications.

These graphene-based sensors suffer from several drawbacks. Defect-free and low-defect graphene have been demonstrated to be sensitive to molecules adsorbed on their surface, but the adsorption probability tends to be low in the absence of dangling bonds. Conversely, defective graphene systems have higher adsorption rates but suffer from long recovery times and lower sensitivity[11]. Three-dimensional ordered graphene constructs, however, may help to overcome these problems. By being composed of few- to multi-layer graphene sheets, these structures have the potential sensitivity of graphene-based sensors while gaining a three-dimensional interconnected framework which lends stability and robustness to the device[119,120]. The added surface area of a three-dimensional system partially mitigates the issue of low adsorption probability, while a carefully engineered three-dimensional geometry allows for the transduction properties of lower-dimensional graphene systems to be preserved. Additionally, these systems may still be modified with defects, heteroatom dopants, or metals to optimize their sensing performance, giving these systems the potential to be important players in next-generation gas sensors.

References

[1] P. R. Wallace, *Phys. Rev.* **1947**, *71*, 622.

[2] X. Q. D. Li, T. Radojicic, R. Vanselow, *Surf. Sci.* **1990**, *225*, L29.

[3] N. R. Gall', E. V. Rut'kov, A. Y. Tontegode, M. M. Usufov, *Tech. Phys.* **1999**, *44*, 1066.

[4] *J. Appl. Phys.* **1966**, *37*, 2179.

[5] C. Oshima, A. Nagashima, *J. Phys. Condens. Matter* **1997**, *9*, 1.

[6] M. Eizenberg, J. M. Blakely, *Surf. Sci.* **1979**, *82*, 228.

[7] R. Peierls, *Ann. Inst. Henri Poincaré* **1935**, *5*, 177.

[8] L. D. Landau, *Phys. Z. Sowjetunion* **1937**, *11*, 26.

[9] null Fradkin, *Phys. Rev. B Condens. Matter* **1986**, *33*, 3263.

[10] K. S. Novoselov, A. K. Geim, S. V. Morozov, D. Jiang, Y. Zhang, S. V. Dubonos, I. V. Grigorieva, A. A. Firsov, *Science* **2004**, *306*, 666.

[11] A. K. Geim, *Science* **2009**, *324*, 1530.

[12] Y. Zhang, Y.-W. Tan, H. L. Stormer, P. Kim, *Nature* **2005**, *438*, 201.

[13] Z. Yan, D. L. Nika, A. A. Balandin, *IET Circuits Devices Amp Syst.* **2015**, *9*, 4.

[14] A. Ambrosi, M. Pumera, *Chem. – Eur. J.* **2016**, *22*, 153.

[15] Y. A. Samad, Y. Li, A. Schiffer, S. M. Alhassan, K. Liao, *Small* **2015**, *11*, 2380.

[16] X. Li, J. Feng, Y. Du, J. Bai, H. Fan, H. Zhang, Y. Peng, F. Li, *J. Mater. Chem. A* **2015**, *3*, 5535.

[17] B. Wicklein, A. Kocjan, G. Salazar-Alvarez, F. Carosio, G. Camino, M. Antonietti, L. Bergström, *Nat. Nanotechnol.* **2015**, *10*, 277.

[18] Y. Liu, L. Yu, C. N. Ong, J. Xie, *Nano Res.* **2016**, *9*, 1983.

[19] L. E. F. Foa Torres, S. Roche, J.-C. Charlier, *Introduction to Graphene-Based Nanomaterials*, **2014**.

[20] J.-C. Charlier, J.-P. Michenaud, X. Gonze, J.-P. Vigneron, *Phys. Rev. B* **1991**, *44*, 13237.

[21] F. Guinea, A. H. Castro Neto, N. M. R. Peres, *Phys. Rev. B* **2006**, *73*, 245426.

[22] C.-H. Park, Y.-W. Son, L. Yang, M. L. Cohen, S. G. Louie, *Phys. Rev. Lett.* **2009**, *103*, 046808.

[23] K. S. Novoselov, E. McCann, S. V. Morozov, V. I. Fal'ko, M. I. Katsnelson, U. Zeitler, D. Jiang, F. Schedin, A. K. Geim, *Nat. Phys.* **2006**, *2*, 177.

[24] M. I. Katsnelson, K. S. Novoselov, A. K. Geim, *Nat. Phys.* **2006**, *2*, 620.

[25] K. I. Bolotin, K. J. Sikes, J. Hone, H. L. Stormer, P. Kim, *Phys. Rev. Lett.* **2008**, *101*, 096802.

[26] D. Guo, R. Shibuya, C. Akiba, S. Saji, T. Kondo, J. Nakamura, *Science* **2016**, *351*, 361.

[27] X. Li, D. Geng, Y. Zhang, X. Meng, R. Li, X. Sun, *Electrochem. Commun.* **2011**, *13*, 822.

[28] M. N. Groves, A. S. W. Chan, C. Malardier-Jugroot, M. Jugroot, *Chem. Phys. Lett.* **2009**, *481*, 214.

[29] J. Duan, S. Chen, S. Dai, S. Z. Qiao, *Adv. Funct. Mater.* **2014**, *24*, 2072.

[30] D. Geng, S. Yang, Y. Zhang, J. Yang, J. Liu, R. Li, T.-K. Sham, X. Sun, S. Ye, S. Knights, *Appl. Surf. Sci.* **2011**, *257*, 9193.

[31] L. Qu, Y. Liu, J.-B. Baek, L. Dai, *ACS Nano* **2010**, *4*, 1321.

[32] A. Zahoor, M. Christy, Y. J. Hwang, Y. R. Lim, P. Kim, K. S. Nahm, *Appl. Catal. B Environ.* **2014**, *147*, 633.

[33] C. Liang, Y. Wang, T. Li, *Carbon* **2015**, *82*, 506.

[34] Z. Ma, S. Dou, A. Shen, L. Tao, L. Dai, S. Wang, *Angew. Chem.* **2015**, *127*, 1908.

[35] M. A. Hoque, F. M. Hassan, D. Higgins, J.-Y. Choi, M. Pritzker, S. Knights, S. Ye, Z. Chen, *Adv. Mater.* **2014**, n/a.

[36] X. Li, L. Fan, Z. Li, K. Wang, M. Zhong, J. Wei, D. Wu, H. Zhu, *Adv. Energy Mater.* **2012**, *2*, 425.

[37] D. Sen, R. Thapa, K. K. Chattopadhyay, *ChemPhysChem* **2014**, *15*, 2542.

[38] S. Some, J. Kim, K. Lee, A. Kulkarni, Y. Yoon, S. Lee, T. Kim, H. Lee, *Adv. Mater. Deerfield Beach Fla* **2012**, *24*, 5481.

[39] C. Zhang, N. Mahmood, H. Yin, F. Liu, Y. Hou, *Adv. Mater. Deerfield Beach Fla* **2013**, *25*, 4932.

[40] P. A. Denis, C. Pereyra Huelmo, A. S. Martins, *J. Phys. Chem. C* **2016**, *120*, 7103.

[41] P. A. Denis, *Chem. Phys. Lett.* **2010**, *492*, 251.

[42] S. J. Zhang, S. S. Lin, X. Q. Li, X. Y. Liu, H. A. Wu, W. L. Xu, P. Wang, Z. Q. Wu, H. K. Zhong, Z. J. Xu, *Nanoscale* **2015**, *8*, 226.

[43] N. M. R. Peres, F. Guinea, A. H. Castro Neto, *Phys. Rev. B* **2006**, *73*, 125411.

[44] D. S. L. Abergel, V. Apalkov, J. Berashevich, K. Ziegler, T. Chakraborty, *Adv. Phys.* **2010**, *59*, 261.

[45] Y. Kim, J. Ihm, E. Yoon, G.-D. Lee, *Phys. Rev. B* **2011**, *84*, 075445.

[46] Q. Chen, A. W. Robertson, K. He, C. Gong, E. Yoon, G.-D. Lee, J. H. Warner, *ACS Nano* **2015**, *9*, 8599.

[47] R. Wang, S. Wang, D. Zhang, Z. Li, Y. Fang, X. Qiu, *ACS Nano* **2011**, *5*, 408.

[48] M. S. Nevius, M. Conrad, F. Wang, A. Celis, M. N. Nair, A. Taleb-Ibrahimi, A. Tejeda, E. H. Conrad, *Phys. Rev. Lett.* **2015**, *115*, 136802.

[49] G. Giovannetti, P. A. Khomyakov, G. Brocks, V. M. Karpan, J. van den Brink, P. J. Kelly, *Phys. Rev. Lett.* **2008**, *101*, 026803.

[50] R. Balog, B. Jørgensen, L. Nilsson, M. Andersen, E. Rienks, M. Bianchi, M. Fanetti, E. Lægsgaard, A. Baraldi, S. Lizzit, Z. Sljivancanin, F. Besenbacher, B. Hammer, T. G. Pedersen, P. Hofmann, L. Hornekær, *Nat. Mater.* **2010**, *9*, 315.

[51] C. Coletti, C. Riedl, D. S. Lee, B. Krauss, L. Patthey, K. von Klitzing, J. H. Smet, U. Starke, *Phys. Rev. B* **2010**, *81*, DOI 10.1103/Physrevb.81.235401.

[52] S. Y. Lee, D. L. Duong, Q. A. Vu, Y. Jin, P. Kim, Y. H. Lee, *ACS Nano* **2015**, *9*, 9034.

[53] Y. Zhang, T.-T. Tang, C. Girit, Z. Hao, M. C. Martin, A. Zettl, M. F. Crommie, Y. R. Shen, F. Wang, *Nature* **2009**, *459*, 820.

[54] A. J. Samuels, J. D. Carey, *ACS Nano* **2013**, *7*, 2790.

[55] T. Taychatanapat, K. Watanabe, T. Taniguchi, P. Jarillo-Herrero, *Nat. Phys.* **2011**, *7*, 621.

[56] X. Zhang, W.-P. Han, X.-F. Qiao, Q.-H. Tan, Y.-F. Wang, J. Zhang, P.-H. Tan, *Carbon* **2016**, *99*, 118.

[57] F. Zhang, B. Sahu, H. Min, A. H. MacDonald, *Phys. Rev. B* **2010**, *82*, 035409.

[58] C. H. Lui, Z. Li, K. F. Mak, E. Cappelluti, T. F. Heinz, *Nat. Phys.* **2011**, *7*, 944.

[59] H. C. Lee, W.-W. Liu, S.-P. Chai, A. R. Mohamed, C. W. Lai, C.-S. Khe, C. H. Voon, U. Hashim, N. M. S. Hidayah, *Procedia Chem.* **2016**, *19*, 916.

[60] D. Kireev, D. Sarik, T. Wu, X. Xie, B. Wolfrum, A. Offenhäusser, *Carbon* **2016**, *107*, 319.

[61] M. B. Lee, Q. Y. Yang, S. T. Ceyer, *J. Chem. Phys.* **1987**, *87*, 2724.

[62] M. Losurdo, M. M. Giangregorio, P. Capezzuto, G. Bruno, *Phys. Chem. Chem. Phys.* **2011**, *13*, 20836.

[63] J. H. Cho, J. J. Gorman, S. R. Na, M. Cullinan, *Carbon* **2017**, *115*, 441.

[64] X. Li, W. Cai, J. An, S. Kim, J. Nah, D. Yang, R. Piner, A. Velamakanni, I. Jung, E. Tutuc, S. K. Banerjee, L. Colombo, R. S. Ruoff, *Science* **2009**, *324*, 1312.

[65] X. Li, W. Cai, L. Colombo, R. S. Ruoff, *Nano Lett.* **2009**, *9*, 4268.

[66] Z. Sun, Z. Yan, J. Yao, E. Beitler, Y. Zhu, J. M. Tour, *Nature* **2010**, *468*, 549.

[67] T. Wu, G. Ding, H. Shen, H. Wang, L. Sun, D. Jiang, X. Xie, M. Jiang, *Adv. Funct. Mater.* **2013**, *23*, 198.

[68] Z. Li, P. Wu, C. Wang, X. Fan, W. Zhang, X. Zhai, C. Zeng, Z. Li, J. Yang, J. Hou, *ACS Nano* **2011**, *5*, 3385.

[69] *Appl. Phys. Lett.* **2010**, *96*, 063110.

[70] Y. Yao, Z. Li, Z. Lin, K.-S. Moon, J. Agar, C. Wong, *J. Phys. Chem. C* **2011**, *115*, 5232.

[71] A. Guermoune, T. Chari, F. Popescu, S. S. Sabri, J. Guillemette, H. S. Skulason, T. Szkopek, M. Siaj, *Carbon* **2011**, *49*, 4204.

[72] J. Campos-Delgado, A. R. Botello-Méndez, G. Algara-Siller, B. Hackens, T. Pardoen, U. Kaiser, M. S. Dresselhaus, J.-C. Charlier, J.-P. Raskin, *Chem. Phys. Lett.* **2013**, *584*, 142.

[73] D. Wei, Y. Liu, Y. Wang, H. Zhang, L. Huang, G. Yu, *Nano Lett.* **2009**, *9*, 1752.

[74] G. Buchowicz, P. R. Stone, J. T. Robinson, C. D. Cress, J. W. Beeman, O. D. Dubon, *Appl. Phys. Lett.* **2011**, *98*, DOI 10.1063/1.3536529.

[75] J.-H. Kim, J. H. Hwang, J. Suh, S. Tongay, S. Kwon, C. C. Hwang, J. Wu, J. Y. Park, *Appl. Phys. Lett.* **2013**, *103*, 171604.

[76] K. Thiyagarajan, A. Ananth, B. Saravanakumar, Y. S. Mok, S.-J. Kim, *Carbon* **2014**, *73*, 25.

[77] J. G. de Vries, S. David Jackson, *Catal. Sci. Technol.* **2012**, *2*, 2009.

[78] B. Cornils, W. A. Herrmann, *J. Catal.* **2003**, *216*, 23.

[79] N. M. Julkapli, S. Bagheri, *Int. J. Hydrog. Energy* **2015**, *40*, 948.

[80] G. A. Somorjai, *Adv. Catal.* **1977**, *26*, 1.

[81] T. Sabalitschka, K. Zimmermann, *Berichte Dtsch. Chem. Ges.* **1930**, *63*, 375.

[82] H. Ries, R. Vannordstrand, M. Johnson, H. Bauermeister, *J. Am. Chem. Soc.* **1945**, *67*, 1242.

[83] F. Hill, P. Selwood, *J. Am. Chem. Soc.* **1949**, *71*, 2522.

[84] H. Jüntgen, *Fuel* **1986**, *65*, 1436.

[85] R. I. Jafri, T. Arockiados, N. Rajalakshmi, S. Ramaprabhu, *J. Electrochem. Soc.* **2010**, *157*, B874.

[86] N. Balke, S. Jesse, A. N. Morozovska, E. Eliseev, D. W. Chung, Y. Kim, L. Adamczyk, R. E. Garcia, N. Dudney, S. V. Kalinin, *Nat. Nanotechnol.* **2010**, *5*, 749.

[87] S. Guo, S. Zhang, S. Sun, *Angew. Chem. Int. Ed.* **2013**, *52*, 8526.

[88] A. Kumar, F. Ciucci, A. N. Morozovska, S. V. Kalinin, S. Jesse, *Nat. Chem.* **2011**, *3*, 707.

[89] A. Harriman, I. J. Pickering, J. M. Thomas, P. A. Christensen, *J. Chem. Soc. Faraday Trans. 1 Phys. Chem. Condens. Phases* **1988**, *84*, 2795.

[90] S. Zhang, Y. Shao, G. Yin, Y. Lin, *J. Mater. Chem. A* **2013**, *1*, 4631.

[91] J. Zhang, C. Ming Li, *Chem. Soc. Rev.* **2012**, *41*, 7016.

[92] Y. Zhang, J. Ge, L. Wang, D. Wang, F. Ding, X. Tao, W. Chen, *Sci. Rep.* **2013**, *3*, DOI 10.1038/srep02771.

[93] S. Sharma, B. G. Pollet, *J. Power Sources* **2012**, *208*, 96.

[94] J. Duan, S. Chen, M. Jaroniec, S. Z. Qiao, *ACS Catal.* **2015**, *5*, 5207.

[95] G. Ruan, Z. Sun, Z. Peng, J. M. Tour, *ACS Nano* **2011**, *5*, 7601.

[96] P. Y. Huang, C. S. Ruiz-Vargas, A. M. van der Zande, W. S. Whitney, M. P. Levendorf, J. W. Kevek, S. Garg, J. S. Alden, C. J. Hustedt, Y. Zhu, J. Park, P. L. McEuen, D. A. Muller, *Nature* **2011**, *469*, 389.

[97] K. Kim, Z. Lee, W. Regan, C. Kisielowski, M. F. Crommie, A. Zettl, *ACS Nano* **2011**, *5*, 2142.

[98] A. W. Tsen, L. Brown, M. P. Levendorf, F. Ghahari, P. Y. Huang, R. W. Havener, C. S. Ruiz-Vargas, D. A. Muller, P. Kim, J. Park, *Science* **2012**, *336*, 1143.

[99] R. Raccichini, A. Varzi, S. Passerini, B. Scrosati, *Nat. Mater.* **2015**, *14*, 271.

[100] E. Llobet, *Sens. Actuators B Chem.* **2013**, *179*, 32.

[101] F. Schedin, A. K. Geim, S. V. Morozov, E. W. Hill, P. Blake, M. I. Katsnelson, K. S. Novoselov, *Nat. Mater.* **2007**, *6*, 652.

[102] S. Basu, P. Bhattacharyya, *Sens. Actuators B Chem.* **2012**, *173*, 1.

[103] F. Yavari, C. Kritzinger, C. Gaire, L. Song, H. Gulapalli, T. Borca-Tasciuc, P. M. Ajayan, N. Koratkar, *Small* **2010**, *6*, 2535.

[104] Y. Dan, Y. Lu, N. J. Kybert, Z. Luo, A. T. C. Johnson, *Nano Lett.* **2009**, *9*, 1472.

[105] W. Wu, Z. Liu, L. A. Jauregui, Q. Yu, R. Pillai, H. Cao, J. Bao, Y. P. Chen, S.-S. Pei, *Sens. Actuators B Chem.* **2010**, *150*, 296.

[106] J. D. Fowler, M. J. Allen, V. C. Tung, Y. Yang, R. B. Kaner, B. H. Weiller, *ACS Nano* **2009**, *3*, 301.

[107] G. Lu, S. Park, K. Yu, R. S. Ruoff, L. E. Ocola, D. Rosenmann, J. Chen, *ACS Nano* **2011**, *5*, 1154.

[108] G. Lu, L. E. Ocola, J. Chen, *Appl. Phys. Lett.* **2009**, *94*, 083111.

[109] J. T. Robinson, F. K. Perkins, E. S. Snow, Z. Wei, P. E. Sheehan, *Nano Lett.* **2008**, *8*, 3137.

[110] S. S. Varghese, S. Lonkar, K. K. Singh, S. Swaminathan, A. Abdala, *Sens. Actuators B Chem.* **2015**, *218*, 160.

[111] F. Yavari, Z. Chen, A. V. Thomas, W. Ren, H.-M. Cheng, N. Koratkar, *Sci. Rep.* **2011**, *1*, srep00166.

[112] J. Wu, K. Tao, Y. Guo, Z. Li, X. Wang, Z. Luo, S. Feng, C. Du, D. Chen, J. Miao, L. K. Norford, *Adv. Sci.* **2016**, *4*, DOI 10.1002/advs.201600319.

CHAPTER VI: Synthesis of Bijel-Templated 3-Dimensional Multi-layer Graphene

Abstract

Current synthesis methods for 3D graphene systems in electrochemical applications suffer from certain limitations. A tunable, consistent pore structure is desirable to optimize mass transport through the material, but self-assembled graphene oxide (GO) based synthesis methods (some of the most common 3D graphene synthesis methods) produce random pores which suffer from blocked pores and inaccessible geometry. Additionally, GO-based 3D graphene systems lose some of the desirable electronic transport and chemical properties of pristine graphene. Conversely, template-based synthesis methods can produce tunable and consistent geometries with high-quality graphene films, but their characteristic macropore sizes are typically on the order of hundreds of microns, making them too large to be optimally efficient. In this work, we utilize a template-based approach using bicontinuous interfacially jammed emulsion gels (bijels) to produce 3D graphene constructs with tunable macropores with a characteristic size of around 30 μm, highly interconnected and open domains, gyroid-like morphology, and highly accessible internal geometry for applications in catalysis and electrochemistry.

Introduction

Three dimensional carbon nanosystems are of great interest in numerous fields, ranging from low-density high-specific-surface-area systems for nanoelectronic devices and batteries to catalysts for reactions such as the oxygen reduction reaction in fuel cells[1–5]. A particularly

promising material for many of these applications is graphene, the sp2-hybridized allotrope of carbon remarkable for its chemical and mechanical stability, 2-dimensional geometry, and unique electronic structure[6–9]. Graphene's stability lends itself well to being a catalyst support because it is durable and chemically inert, while its flexible 2D geometry allows for the creation of very high surface area structures such as graphene nanotube networks, foams, and aerogels[10–15]. Studies of these structures have demonstrated the feasibility of carbon-based 3D structures for electrochemical applications, but the efficiency of these systems is limited by several factors. Many 3d-graphene systems are random arrays, so they can suffer from reduced analyte flow from blocked channels or otherwise inaccessible geometries. The random nature of the current growth methods can also lead to varying pore sizes and warping or kinks in the graphene sheets, and research suggests that graphene's electronic structure is changed by variations in surface curvature[16,17]. Additionally, current 3D-graphene materials suffer from a lack of accurate micro-scale tunability to adjust pore geometry and optimize analyte flow. Further advancement in 3D-graphene materials depends on improved organization, uniformity, and structural tunability.

To address these points, we use a class of materials called bicontinuous interfacially jammed emulsion gels (bijels) as templates for the growth of graphene-based porous materials. These materials are notable for having a mean curvature centered on zero and for having a negative area-averaged Gaussian curvature; properties similar to a gyroid. Bijels are formed through arrested spinodal decomposition of a ternary liquid-liquid-colloid mixture. During phase separation between the two liquid components, the colloidal particles group at the liquid-liquid interface and become jammed once the interfacial area is sufficiently small. The final morphology of this jammed particle system can be tuned by adjusting the liquid-liquid-colloid ratios and through the wetting characteristics of the chosen materials[18–20]. Free-standing

polymeric bijel templates are formed by infusing the mixture with a photoactive monomer that preferentially mixes with one of the two fluids. UV treatment results in selective polymerization and the remaining liquid phase is drained. This takes advantage of the smooth interface created during spinodal decomposition to form a node-free, uniform material with a tunable internal microstructure. Through a process outlined in detail below, we report 3D graphene constructs synthesized on bijel templates for the first time. In this process, a polymer bijel is coated with Ni through electroless deposition, graphene is grown via chemical vapor deposition (CVD), and the Ni template is etched away, leaving a 3D graphene bijel.

To develop these novel materials and optimize their structural and electrochemical properties to their various applications, it is necessary to understand the growth mechanics of graphene on the template material. We employ a variety of surface analytical techniques to characterize graphene growth on the bijel template. We also clarify the stacking behavior of the synthesized graphene films by creating a 2-dimensional analogous system composed of Ni on SiO2. We chose SiO2 as the substrate to aid in the characterization of graphene to take advantage of SiO2's chemically inert nature and weak coupling with graphene and to compare the quality of the present study's graphene with existing well-established benchmarks in graphene/SiO2 systems[21–23]. To modify SiO2 to better analogize polymer bijels and bond with the Pd^2+ catalysts for the electroless plating process we functionalized the SiO2 wafers with a self-assembled monolayer of APTES. We characterize these 2d systems using a combination of Raman spectroscopy, X-ray photoelectron spectroscopy (XPS), and scanning tunneling microscopy/spectroscopy (STM/STS), lending insight into the growth behavior of graphene on bijel templates.

Results and Discussion

Fabrication of three-dimensional multilayer graphene, bicontinuous architectures

Three-dimensional multilayer graphene (Bi-3DG) bicontinuous architectures are fabricated using chemical vapor deposition (CVD) of methane on a sacrificial Ni scaffold. The Ni scaffold is formed via electroless deposition of Ni on a polyethylene (glycol) diacrylate (PEGDA) bijel-derived template that provides the porous bicontinous 3D architecture. The fabrication procedure is described here**.** Briefly, bijels are formed by jamming of colloidal silica particles (500 nm diameter) at the interface between water and 2,6-Lutidine under spinodal decomposition. PEGDA templates form by infusing the mixture with a photoactive monomer that preferentially mixes with 2,6-Lutidine. After UV exposure polymerizes the PEGDA, the remaining water is drained and silica particles are removed with hydrofluoric acid.

Electroless deposition of Ni is carried out in a plating solution of 20 mM nickel chloride hexahydrate, 20 mM sodium tartrate dihydrate, and 1 M hydrazine for 60 minutes produces a Ni coating with an approximate thickness of 1 μm throughout the bijel template.[6] The Ni/PEGDA template is subsequently sintered for 1 hour at 300°C and 1 hour at 500°C in air to remove PEGDA and then annealed at 450°C in a reducing environment of 10% H_2 in Ar to reduce Ni, resulting in a metallic Ni scaffold. In the next processing stage, CVD is performed with methane as a precursor in a tube furnace to grow graphene on the Ni scaffold.[7–9] Finally, the Ni backbone is etched in a 1M solution of $FeCl_3$ to produce a free-standing three-dimensional multilayer graphene bicontinuous architecture (Bi-3DG). **Figure 21** shows the schematic of the growth steps with optical images of the PEGDA template, Ni scaffold before and after CVD, and finally the Bi-3DG structure alongside a inch ruler to show the macroscopic length scales.

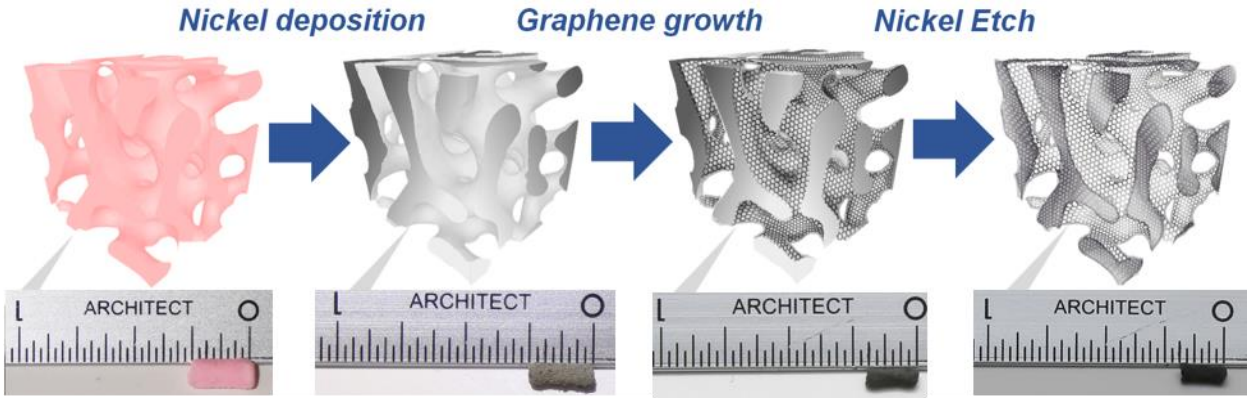

Figure 21: Schematic depicting the Bi-3DG synthesis process. A PEGDA bijel template is coated with a Ni film via electroless deposition. The Ni/PEGDA bijel template is sintered/reduced and then used as a scaffold for CVD graphene growth. Finally, the Ni backbone is etched away in an $FeCl_3$ solution.

After each processing stage, samples were characterized with scanning electron microscopy (SEM), X-ray photoelectron spectroscopy (XPS), and Brunauer, Emmett, and Teller (BET) specific surface area analysis. SEM images, as shown in **Figure 22** at different processing stages, confirms the preservation of the bicontinuous morphology through each of the sample processing stages.

The characteristic pore size of the PEGDA templates is tuned to a nominal value of 30 μm[6]. SEM micrographs at each processing stage show pore sizes consistent with this value. Magnified regions shown in the insets in **Figure 22** highlight the pore sizes of each sample. A red circle highlights the same feature on the surface at each processing stage.

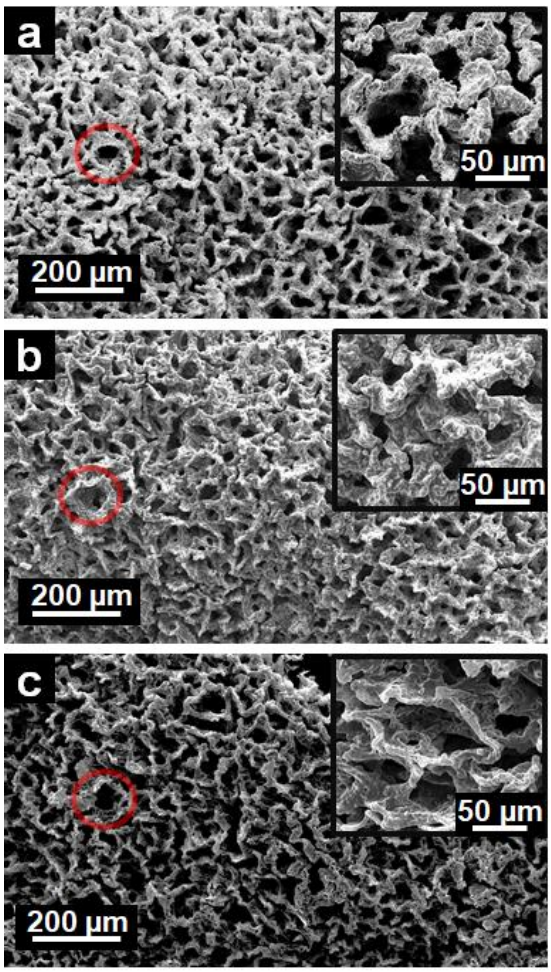

Figure 22: SEM images of the bijel-templated sample (a) after electroless plating of Ni, and sintering at 500°C in air and reducing in forming gas at 450°C, (b) after CVD growth of graphene at 900°C on Ni scaffold, and (c) after the Ni has been etched with $FeCl_3$ to form Bi-3DG structure.

Chemical analysis is conducted using XPS. As shown in **Figure 23**a, the signature Ni 2p peak at 852.6 eV is unsurprisingly observed after electroless deposition and CVD growth, but is not observable after etching. Thus, the $FeCl_3$ etch appears to remove the Ni scaffold completely. XPS spectra in the region of the C 1s peak is shown in **Figure 23**b. A small C 1s peak is observed before CVD graphene growth is performed, likely due to residual C remaining after the sintering step. Again unsurprisingly, the signal increases after CVD growth. Here, the C 1s peak

location shifts closer to 284 eV after CVD growth and indicates sp2-hybridized (graphitic) carbon.[10] Raman spectroscopy measurements were also performed after CVD growth and after Ni etch to further assess the nature of the deposited carbon. The two most intense features observed in **Figure 23**c are located at the 1580 cm^{-1} G band and the 2700 cm^{-1} 2D band. It is understood that as the number of layers of graphene increases, the relative intensity of the 2D peak decreases with respect to the G peak, and the 2D band itself broadens.[11]. Thus, the typical intensity ratio I_{2D}/I_G of approximately 0.5 after the $FeCl_3$ etch confirms that the final Bi-3DG system is mostly composed of many layers of graphene, although the total number of layers and the stacking configuration remains unknown with just Raman spectra.

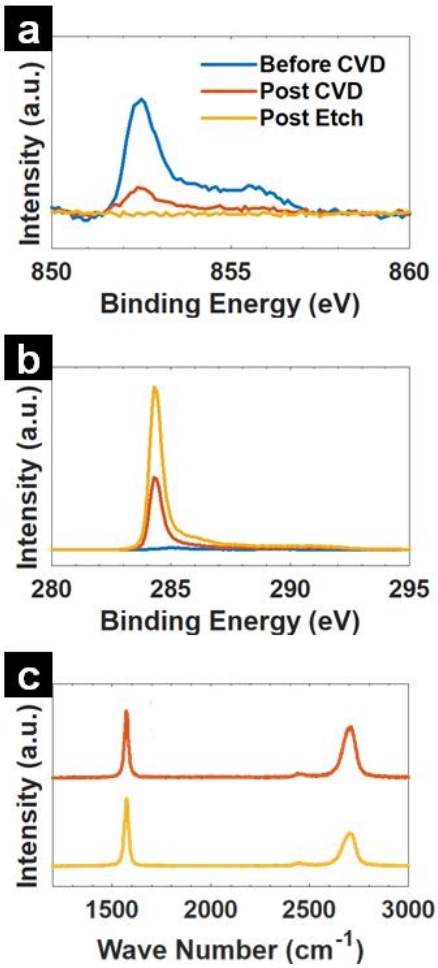

Figure 23: XPS spectra of (a) Ni 2p peak and (b) C 1s peak on the bijel-templated sample on Ni scaffold (blue curve), after CVD growth (red curve), Bi-3DG (gold curve). (c) Representative Raman spectra taken after CVD growth and Ni etch.

Finally, the BET method using N_2 adsorption was applied to measure specific surface areas (SSA). Results determined SSAs of 6.42 m^2/g before CVD growth, 14.0 m^2/g after growth, and 500 m^2/g after etching. The initial increase in SSA after CVD growth is attributed to the extra surface area of the multilayer graphene. The high SSA in the final Bi-3DG system indicated the successful synthesis of a high surface area material and confirmed that effects such as graphene re-stacking and pore collapse did not significantly reduce the accessible surface area.

Characterization of a two-dimensional analogue

To clarify the stacking behavior of the synthesized graphene films, we utilized STM. In order to perform high resolution STM measurements of systems similar to the Bi-3DG system, we produced two-dimensional analogues (2DG); 1μm Ni films were electrolessly deposited onto modified SiO_2 surfaces followed by CVD graphene growth (see Methods for further details). Raman spectroscopy measurements shown in **Figure 24**a indicate that the 2DG system serves as a simplified two-dimensional analogue of the Bi-3DG system, displaying what appears to be similar graphene stacking behavior without the added variability of a 3D substrate. The typical values of 2D peak full width at half maximum (FWHM) for the 2DG system were around 65 cm^{-1}, upshifted with respect to the corresponding values of around 55 cm^{-1} for the graphene-modified Ni scaffold, and the intensity ratios I_{2D}/I_G were lower at around 0.5 compared to the 3D system's 0.7. We attribute this to the lack of curvature-related effects in this system. **Figure 24** b and c show low-voltage SEM images were taken on both the Bi-3DG and 2DG after CVD growth. Ni grains of about 1-5 μm in size can be seen in both images. Additionally, regions of various contrasts are visible, and previous studies have determined these regions to correspond to different graphene domains. [12]

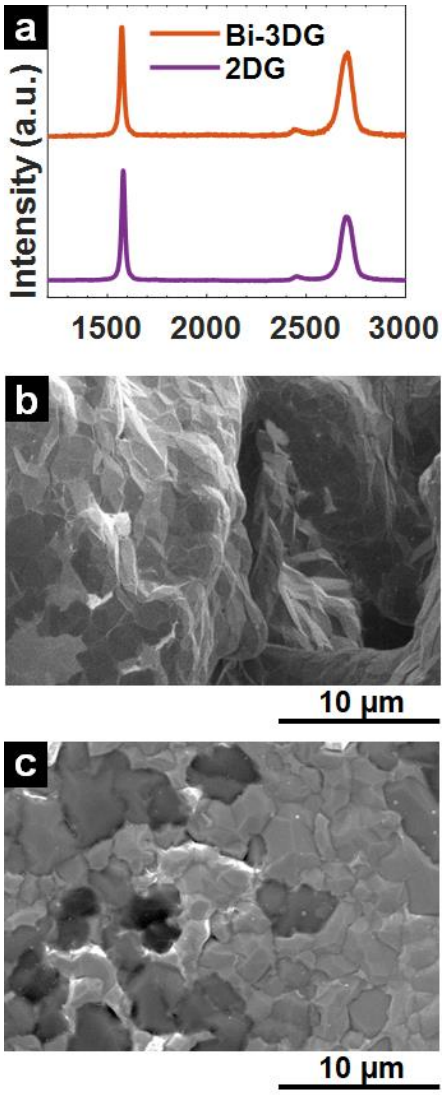

Figure 24: (a) Average of Raman spectroscopy maps taken for both the 2DG analogue and bijel-templated system show comparable intensity ratios between I_{2D} and I_G peaks. (b,c) Low voltage SEM image of the bijel-templated sample and of 2DG sample after graphene growth.

When the sample is characterized via scanning tunneling microscopy (STM), various Moiré patterns are visible on the surface. An example of this is shown in **Figure 26**: 50 nm X 50 nm STM image of a 2DG analogue (I_{set}=0.4nA, V_{GAP}=400 mV) of graphene on EN. Fourier transforms are taken in three regions displaying different Moire patterns., in which three patterns are visible. Shown in the figure's insets, the Fourier transforms of the three indicated regions in

the image also reflect this finding, with low frequency spots visible.. The large domain (**Figure 6**b) exhibits two different Moiré patterns, which suggest an incommensurability with regards to two rotationally different graphene domains, both of which exist immediately below the surface layer. The boundary between these domains is visible in the top left of the figure. The Moiré pattern in the upper right corner (**Figure 6**c) of the image represents another uppermost graphene domain that is rotationally distinct from its neighbor. A clear defect boundary demarks the transition from one domain into the other. The variety of rotational domains observed suggests decoupling between the graphene layers in the system. Additional faint boundaries can be seen in the large domain, suggesting the presence of deeper sub-surface graphene layers. Although it is uncertain how deep these layers are, the fact that the visible Moiré patterns appear independent of these boundaries suggests that overall, the graphene layers are decoupled from each other and the nickel film. These findings are consistent with that of similar studies that investigated the growth behavior of graphene on polycrystalline Ni. [13] For polycrystalline Ni, domains are randomly oriented on the macroscopic scale, and some of these will possess the same facets as Ni(111). During the CVD, the formation of graphene is inhomogeneous over a surface, because of the competing mechanisms of Ni(111) surface-catalyzed growth, [14] diffusion of C atoms into the bulk Ni, segregation of C to the surface, and graphene nucleation at the grain boundaries where different crystal orientations with different segregation abilities coexist. As such, graphene grains may connect with or grow over each other, resulting in multilayer graphene with rotational disorder and weak interlayer interactions in the final system.

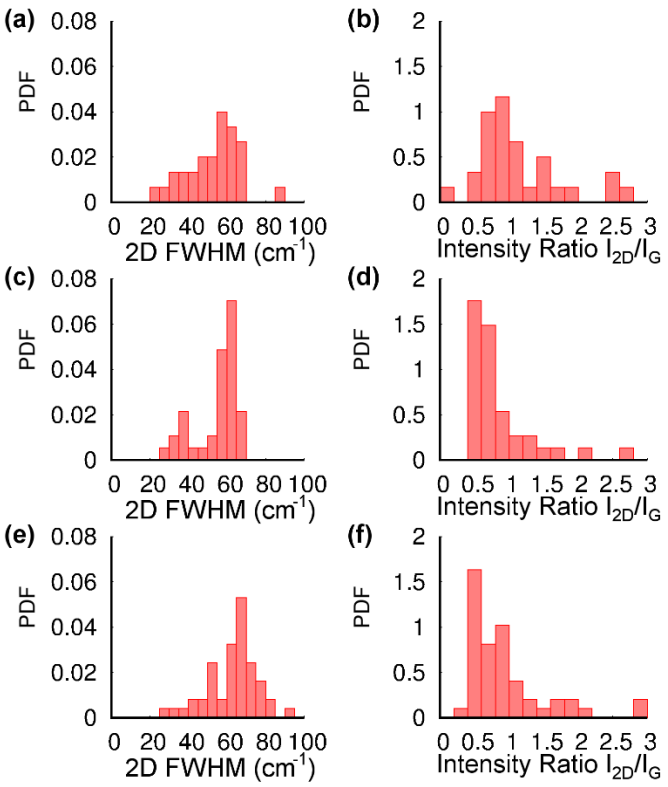

Figure 25: Probability density histograms showing results of Raman spectrum analysis. The measured values for the 2D peak FWHM and the intensity ratio I_{2D}/I_G are shown for (a and b) the graphene-modified Ni scaffold, (c and d) Bi-3DG, and (e and f) the graphene-modified two-dimensional analogous system.

This interpretation is supported by Raman measurements. The majority of Raman spectra of the 2-dimensional system have a 2D FWHM near 65 cm^{-1} and an intensity ratio I_{2D}/I_G near *0.5*, however there are many spectra that exhibit a smaller 2D FWHM and a higher intensity ratio (See Supplemental Figure S1). These spectra resemble single-layer graphene with their low FWHMs and high intensity ratios, but single-layer graphene should interact strongly with the Ni substrate and suppress the signature graphene modes. [15] Rather, these variations in the spectra correspond to varying degrees of interlayer coupling due to rotational misalignment and geometrical variations, and are not purely due to variations in layer number. [16,17] In comparison,

Raman spectra taken from the graphene-modified Ni scaffold show variations in *2D FWHM* and intensity ratio that are more pronounced, which we attribute to geometry-related effects. After the rigid Ni scaffold is removed, the system relaxes and graphene films are free to stack more closely. As a result, Raman spectra for the Bi-3DG system show less random variation than the Ni-supported systems, but approximately 20% of the spectra exhibit a FWHM around 35 cm^{-1} and an intensity ratio above 0.7, corresponding to regions where the graphene layers become electronically decoupled from each other due to large interlayer mismatch angles.[16]

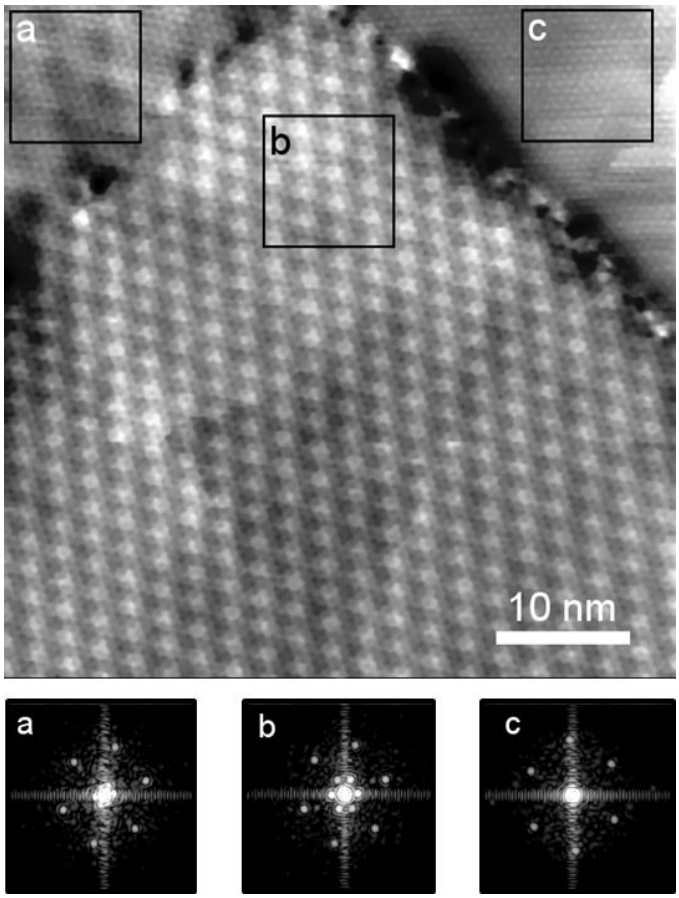

Figure 26: 50 nm X 50 nm STM image of a 2DG analogue (I_{set}=0.4nA, V_{GAP}=400 mV) of graphene on EN. Fourier transforms are taken in three regions displaying different Moire patterns.

Conclusion

We have synthesized a highly porous 3-dimensional graphene-based material with the tunable microstructure of a bijel using a template-based approach. It was demonstrated that the bijel's unique pore morphology is preserved throughout the processing stages. Raman spectroscopy and STM results indicate that the material consists of mainly multi-layered graphene sheets with rotational misalignment. The material also has a high SSA of 500 m^2/g. The Bi-3DG system should prove to be a promising material for catalysis and electrochemistry due to its high SSA, pristine graphene sheets with a large size, and its gyroid-like pore morphology, allowing for efficient mass transport and electron transport while taking advantage of graphene's unique surface chemistry. These results, combined with the scalable and relatively facile nature of the synthesis methods used, should prove to have significant implications in both academia and industry.

Methods

Synthesis of bicontinuous jammed emulsion (bijel)

Poly(ethylene glycol) diacrylate (PEGDA) bijels are synthesized as described in a previous report. [18] Stöber process silica with controlled surface chemistry were dispersed via ultrasonic horn in water (Millipore) and mixed with 2-6 Lutidine (Sigma-Aldrich, St. Louis, MO, CAS#108-48-5), such that the respective volume fractions were 66.9%, 30.1% and 3.02%. 205 microliter samples were heated in a microwave for 30 seconds at a power of 160W to induce spinodal decomposition of the water and oil, and then transferred to a 70°C oven to maintain sample temperature above the critical point of 33.9°C.[19] The oven was controlled to 70°C because of the potential for temperature drops during monomer addition or polymerization. 35µl

of polyethylene glycol diacrylate 250 (PEGDA, Sigma Aldrich, St. Louis, MO, CAS# 26570-48-9) was added to the top of each sample with 1 vol% Darocur 1173 (Ciba Specialty Chemicals, Basel, Switzerland) as a photoinitiator. The monomer diffused through the organic phase of the bijel for four hours before UV polymerization (Omnicure Series 1000, 100W power). After curing, the scaffolds were rinsed with deionized water to remove unreacted monomer. Silica particles were etched from internal surfaces via 5 hour treatment with 6M hydrofluoric acid (Fisher Scientific, Hampton, NH, CAS # 7732-18-5). Excess acid was rinsed from the polymer scaffold with water and left to dry at 70°C

Synthesis of Electroless Ni (EN) 3D scaffold

Nickel is deposited on the PEGDA bijel templates using an EN solution. This system is then heated in air and subsequently in heated in a reducing environment to remove the PEGDA and leave a freestanding Ni scaffold as described in previous work.[4] The electroless deposition of nickel onto PEGDA scaffolds has been detailed thoroughly in [Ref here]. Briefly, the scaffolds soak in a saturated solution of palladium chloride in alcohol overnight. The plating solution is 0.02 M nickel chloride hexahydrate (Fisher Scientific, Hampton, NH, CAS# 7791-20-0), 0.02 M sodium tartrate dehydrate (Aldrich Chemical Company, Milwaukee, WI, CAS# 6106-24-7), and 1M hydrazine (Sigma-Aldrich, St. Louis, MO, CAS#10217-52-4). The pH of the bath is adjusted to ~10 by addition of sodium hydroxide and maintained throughout the duration of the plating process with NaOH additions as necessary. The temperature of the bath is controlled to 95°C via immersion in a hot water bath. The plating bath is drained after 75 minutes and the scaffolds rinsed in water to remove unreacted salts. The scaffolds are heat treated for 1 hour at 300°C and 1 hour at 500°C in air to remove the polymer backbone. The furnace is then purged with argon and filled with forming gas (10% H_2, 90% Ar) for the final 8 hours at 450 °C to reduce the

oxidized nickel to its metallic state and sinter particles together to impart structural integrity to the scaffold.

Synthesis of 2-dimensional EN thin films

SiO_2/Si wafers (300nm oxide) are treated with an RCA-1 solution for 15 minutes, immersed in 3 separate deionized water baths, rinsed in flowing deionized water, and dried with N_2 gas. The wafers were immediately transferred into a 0.5 mmol (3-Aminopropyl) triethoxysilane (APTES) / deionized water and left for 12-16 hours. Afterwards, the wafers are removed from the APTES solution, rinsed in a methanol stream and sonicated in methanol for 2 minutes. The wafers are ethanol rinsed and activated in a solution of supersatured $PdCl_2$ in ethanol for at least 1 hour. Subsequently, EN deposition was performed as described in the above section with the addition of Tween 20 surfactant to reduce bubble-induced delamination on the EN surface. The resultant EN/SiO_2/Si were rinsed with ethanol and dried on a hot plate at 105°C for 5 minutes.

Chemical vapor deposition of Graphene

All samples were loaded into a 1" quartz tube and evacuated to a pressure of ~10^{-2} torr while flowing forming gas (5% H_2 in Ar) at 100 SCCM into the system. The furnace was purged under forming gas for one hour and then ramped at a rate of 10°C/min to 800°C. The samples are held at 800°C for 30 minutes. The furnace temperature was then increased to 900°C at a rate of 10°C/min, at which point, 5 SCCM CH_4 was introduced into the system for 30 minutes (with 100 SCCM forming gas flowing during the entirety of the experiment). Subsequently, CH_4 was turned off and the furnace was allowed to cool to room temperature at 10°C/min with no active cooling.

Freestanding 3D Graphene

After CVD growth on EN, samples are etched in 1M $FeCl_3$ aqueous solution at room temperature for 12 hours. The remaining graphene structure is immersed in deionized water three times and dried on a hot plate at 130°C for 5 minutes.

Characterization

Raman measurements were obtained on a Renishaw *InVia* Raman microscope with 532 nm incident laser. XPS measurements were performed with an *AXIS Supra* XPS by Kratos Analytical using a monochromated Al K α radiation (hν = 1486.6 eV). SEM images were performed in an FEI/Philips XL30 FESEM. Low accelerating voltage images were taken in a FEI Magellan 400 XHR SEM. Images were scanned at 10 kV and 1kV (respectively) with 3.0 μm spot size, and 10 mm working distance. STM measurements were taken with an *Omicron VT-SPM* operating at room temperature and at a base pressure of approximately 10^{-11} torr. Etched tungsten tips were thermally degassed before use and used for all measurements. Images were analyzed using Image Metrology's SPIP and Wolfram Mathematica v11 software. Samples were annealed for 24 hours at 600 ºC to remove surface adsorbates prior to scanning.

References

[1] M. E. Cates, P. S. Clegg, *Soft Matter* **2008**, *4*, 2132.

[2] M. N. Lee, J. H. J. Thijssen, J. A. Witt, P. S. Clegg, A. Mohraz, *Adv. Funct. Mater.* **2013**, *23*, 417.

[3] M. N. Lee, A. Mohraz, *Adv. Mater.* **2010**, *22*, 4836.

[4] W. Yan, W.-Y. He, Z.-D. Chu, M. Liu, L. Meng, R.-F. Dou, Y. Zhang, Z. Liu, J.-C. Nie, L. He, *Nat. Commun.* **2013**, *4*, 2159.

[5] D. Dutta, B. C. Wood, S. Y. Bhide, K. G. Ayappa, S. Narasimhan, *J. Phys. Chem. C* **2014**, *118*, 7741.

[6] J. A. Witt, D. R. Mumm, A. Mohraz, *J. Mater. Chem. A* **2016**, *4*, 1000.

[7] A. Reina, X. Jia, J. Ho, D. Nezich, H. Son, V. Bulovic, M. S. Dresselhaus, J. Kong, *Nano Lett.* **2009**, *9*, 30.

[8] S. Thiele, A. Reina, P. Healey, J. Kedzierski, P. Wyatt, P.-L. Hsu, C. Keast, J. Schaefer, J. Kong, *Nanotechnology* **2010**, *21*, 015601.

[9] L. G. De Arco, Yi Zhang, A. Kumar, Chongwu Zhou, *IEEE Trans. Nanotechnol.* **2009**, *8*, 135.

[10] R. I. . Blyth, H. Buqa, F. . Netzer, M. . Ramsey, J. . Besenhard, P. Golob, M. Winter, *Appl. Surf. Sci.* **2000**, *167*, 99.

[11] A. C. Ferrari, *Solid State Commun.* **2007**, *143*, 47.

[12] X. Li, W. Cai, J. An, S. Kim, J. Nah, D. Yang, R. Piner, A. Velamakanni, I. Jung, E. Tutuc, S. K. Banerjee, L. Colombo, R. S. Ruoff, *Science* **2009**, *324*, 1312.

[13] Y. Zhang, T. Gao, S. Xie, B. Dai, L. Fu, Y. Gao, Y. Chen, M. Liu, Z. Liu, *Nano Res.* **2012**, *5*, 402.

[14] J. C. Shelton, H. R. Patil, J. M. Blakely, *Surf. Sci.* **1974**, *43*, 493.

[15] A. Dahal, M. Batzill, *Nanoscale* **2014**, *6*, 2548.

[16] C.-H. Yeh, Y.-C. Lin, P. K. Nayak, C.-C. Lu, Z. Liu, K. Suenaga, P.-W. Chiu, *J. Raman Spectrosc.* **2014**, *45*, 912.

[17] J.-B. Wu, H. Wang, X.-L. Li, H. Peng, P.-H. Tan, *Carbon* **2016**, *110*, 225.

[18] J. A. Witt, D. R. Mumm, A. Mohraz, *J. Mater. Chem. A* **2016**, *4*, 1000.

[19] A. Loven, O. Rice, *Trans. Faraday Soc.* **1963**, *59*, 2723.

CHAPTER VII: Future Applications of Bi-3DG

Applications

Graphene has become a very important topic in fields such as electrochemical sensing, heterogeneous catalysis, and gas sensing due to its extremely high specific surface area, high charge mobility and tunable carrier density, unique band structure, and unique electrochemical properties. Graphene-based electrochemical sensors have shown great promise due to graphene's resistance to corrosion[1], excellent charge transport properties[2], and potential for extremely high surface areas to increase sensitivity[3,4]. Graphene oxide (GO)-based systems are frequently used for these applications because of its relative ease to deposit on an electrode and abundance of carboxylic groups[5], but this often requires hybridization with another functional material. However, the inherent disorder due to the synthesis of these systems is detrimental to the bulk transport properties of the final electrode systems. To take advantage of graphene's inherent properties, it is therefore optimal to avoid GO-based synthesis methods. For this reason, template-based approaches to graphene synthesis are appealing for producing high quality highly multiplexed 3D graphene structures.

Heterogeneous catalysts based on graphene systems have also risen in popularity. Its resistance to corrosion has made noble-metal-decorated graphene an important research topic, with the potential for graphene-derived systems to reduce catalyst poisoning[6], increase catalyst lifespan[7], and take advantage of graphene's transport properties while utilizing the same chemistry of traditional heterogeneous catalysts[8]. Moreover, metal-free catalysis is made possible with graphene, indicating the potential for graphene systems to be dramatically more sustainable than traditional noble-metal heterogeneous catalysts[9,10].

Gas sensing applications are another important application of graphene. Carbon nanotubes (CNTs) have been studied for gas sensing applications since 2000, when it was demonstrated that their conductivity was strongly dependent on ambient gas composition[11]. Single-layer graphene sheets have also been used as chemiresistive gas sensors, and demonstration of single-molecule detection limits was one of the largest triumphs of graphene research after the seminal report of its isolation by Geim and Novoselov in 2004[12,13]. Further research has demonstrated gas sensors derived from CNTs as well as graphene sheets modified with heteroatom dopants or noble metal nanoparticles. However, these systems often suffer from issues arising from contamination, variations from sample to sample, and a high cost to manufacture[14].

Many of the setbacks to graphene-based devices overlap, so improvements with one application in mind can often be beneficial for other reasons. For instance, these applications benefit from efficient charge transfer and mass transfer pathways to facilitate surface processes. Simple, reliable, and scalable synthesis methods allow for large-scale synthesis of these devices while reducing unwanted variability in the final products. Careful control of the surface chemistry is also desired to reduce contamination and protect from corrosion. These issues can be addressed with a sufficiently well-controlled template-based synthesis technique. With careful design of a 3D template with appropriate pore structure, template-grown graphene can have a morphology that is conducive to both efficient charge transfer within the graphene sheets as well as efficient mass transfer through the system's open pores. A template structure with a highly controllable and scalable synthesis method can be used to facilitate this. Additionally, graphene synthesized via chemical vapor deposition (CVD) on metal templates is well-characterized and of high quality, and modifiable to obtain doped or multi-layered graphene sheets. An interesting

strategy to utilize these advantages is to use a bijel-derived metal scaffold for templated graphene growth, as presented in the previous chapter. Their large surface area, balanced with an internal surface area completely accessible to a fluid analyte[15], and macroporous tunable morphology make them ideally suited to applications requiring surface contact with an analyte, such as electrochemical applications[16]. The process laid out in the previous chapter describes the synthesis of bijel-templated 3D porous graphene constructs (Bi-3DGs), and following are brief outlines for future work to apply this material to real-world applications.

Gas Sensing using Bi-3DG

Existing graphene-based chemiresistor gas sensors typically operate by having a target gas modulate carrier concentration in the graphene lattice. For this reason, Pd-modified sheet graphene and GNRs have shown remarkable promise since PdH_X groups tend to decrease the density of p-type carriers, increasing the sheet resistance of graphene sheets. This effect is more pronounced in GNRs[17,18].

The Bi-3DG system, however, is morphologically distinct from these lower dimensional systems. This is a large (mm-scale) device, consisting of graphene flakes on the order of 1 micron in width. This implies that there will be a large number (at least (device lengthscale)/(flake lengthscale) = 1000) of interlayer transitions, making the total resistance of the Bi-3DG system a combination of the AB-axis resistance and the C-axis resistance. Graphene's large carrier mobility makes its sheet resistance low, but the C-axis (out of plane) resistance is much higher due to the relatively weak interlayer coupling[19]. The large number of interlayer transitions causes there to be a large contribution to the overall resistance.

Additionally, since the limiting factor in the conductivity is the interlayer coupling, a reduction in interlayer coupling should increase resistance.

The sensitivity of the Bi-3DG system to H_2 gas was investigated, and it was found that there was only a negligible chemiresistive response. The modulation in c-axis conductivity is too weak to make a large difference in bulk conductivity of the Bi-3DG. To apply this system to gas sensing applications, one would therefore have to significantly modify the graphene films to sensitize them to a target gas such as H_2.

Electrochemical application of Bi-3DG

Surface area is an essential characteristic of an electrode material in electrochemistry, particularly in applications such as energy storage, biocatalysis, and sensors[20]. Bi-3DG systems were demonstrated to have a respectable SSA of 500 m^2/g, only an order of magnitude lower than that of single-layer graphene. In practice, however, it will be important to tune the morphology of the structure to maximize the surface area accessible to an analyte. Preliminary electrochemical tests were performed, and trapped gas bubbles were found to be a large problem, reducing the electroactive surface area (calculated by comparing cyclic voltammograms in a ferricyanide solution for the Bi-3DG and a glassy carbon electrode with known surface area) drastically. However, Electrochemical impedance spectroscopy measurements found the charge transfer resistance of the Bi-3DG to be lower than that of a glassy carbon electrode, indicating that the pristine CVD graphene's electronic transport properties aid in charge transfer to solution.

The Bi-3DG is therefore promising in electrochemical applications, but steps must be taken to apply it in a useful way. First, the air bubbles must be dealt with, likely using a vacuum system to pull the air from the bijel. Second, the graphene films must be modified to optimize the

surface chemistry to particular applications. Graphene's surface chemistry is dramatically altered in the presence of dopants, defects, functional groups, and adsorbed species, and these modifications can be used to optimize a graphene system to a particular catalytic or sensing application[20].

A straightforward route forward to develop Bi-3DG electrodes is to pursue synthesizing nitrogen-doped Bi-3DGs. Nitrogen-doped graphene is one of the most well-studied modified graphene systems, and it has been demonstrated to catalyze oxygen reduction, and as a promising electrode material in supercapacitors and Li-ion batteries[10,21]. Particularly appealing about this system is that nitrogen-doped graphene can be synthesized via chemical vapor deposition by simply adding ammonia to the carbon precurso[21]r mixture; an easy modification to make.

Another route forward, and a vital one at that, is layer engineering; the careful control of the number of graphene layers and the interlayer interaction. It was found that the current Bi-3DG system has many layers. If the total number of layers were to be reduced, the surface area would of course increase, and we may see an increase in bulk conductivity due to the system behaving more like single-layer graphene (rather than graphite). However, there will be a tradeoff, for the mechanical strength of the system will be compromised with a reduction in graphene layers. Careful study and control of the graphene layers will be very important in the optimization of the system. Preliminary studies have, in fact, indicated that the number of graphene layers can be modulated by changing the composition of the bijel-derived sacrificial metal template. When a Cu-Ni alloy was used (rather than pure Ni) and decorated with graphene using chemical vapor deposition, Raman spectra indicated that there were fewer graphene layers. This is due to changes in the alloy's carbon solubility affecting the graphene growth mechanics.

Precise control over the graphene growth and film properties will be of the utmost importance in the creation of a robust, stable, and efficient electrode for electrochemistry.

Conclusion

To summarize, the Bi-3DG system may not be ideally suited as-is for gas sensing applications, but it holds great promise in electrochemical applications. It has the potential to take advantage of graphene's unique electronic, structural, and chemical properties to make a highly desirable electrode. Moving forward, the next steps in the development of this 3d graphene system are creating a nitrogen-doped system to apply to electrochemical sensing and the precise control of the layer structure to optimize electronic transport and structural stability.

References

[1] D. Prasai, J. C. Tuberquia, R. R. Harl, G. K. Jennings, K. I. Bolotin, *ACS Nano* **2012**, *6*, 1102.

[2] A. V. Rozhkov, G. Giavaras, Y. P. Bliokh, V. Freilikher, F. Nori, *Phys. Rep.* **2011**, *503*, 77.

[3] X. Dong, X. Wang, L. Wang, H. Song, H. Zhang, W. Huang, P. Chen, *ACS Appl. Mater. Interfaces* **2012**, *4*, 3129.

[4] L. Zhang, F. Zhang, X. Yang, G. Long, Y. Wu, T. Zhang, K. Leng, Y. Huang, Y. Ma, A. Yu, Y. Chen, *Sci. Rep.* **2013**, *3*, DOI 10.1038/srep01408.

[5] S. Roy, N. Soin, R. Bajpai, D. S. Misra, J. A. McLaughlin, S. Sinha Roy, *J. Mater. Chem.* **2011**, *21*, 14725.

[6] N. M. Julkapli, S. Bagheri, *Int. J. Hydrog. Energy* **2015**, *40*, 948.

[7] Y. Zheng, Y. Jiao, M. Jaroniec, Y. Jin, S. Z. Qiao, *Small* **2012**, *8*, 3550.

[8] S. Bong, Y.-R. Kim, I. Kim, S. Woo, S. Uhm, J. Lee, H. Kim, *Electrochem. Commun.* **2010**, *12*, 129.

[9] Z. Ma, S. Dou, A. Shen, L. Tao, L. Dai, S. Wang, *Angew. Chem.* **2014**, n/a.

[10] L. Qu, Y. Liu, J.-B. Baek, L. Dai, *ACS Nano* **2010**, *4*, 1321.

[11] J. Kong, N. R. Franklin, C. Zhou, M. G. Chapline, S. Peng, K. Cho, H. Dai, *Science* **2000**, *287*, 622.

[12] K. S. Novoselov, A. K. Geim, S. V. Morozov, D. Jiang, Y. Zhang, S. V. Dubonos, I. V. Grigorieva, A. A. Firsov, *Science* **2004**, *306*, 666.

[13] F. Schedin, A. K. Geim, S. V. Morozov, E. W. Hill, P. Blake, M. I. Katsnelson, K. S. Novoselov, *Nat. Mater.* **2007**, *6*, 652.

[14] E. Llobet, *Sens. Actuators B Chem.* **2013**, *179*, 32.

[15] M. N. Lee, A. Mohraz, *Adv. Mater.* **2010**, *22*, 4836.

[16] J. A. Witt, D. R. Mumm, A. Mohraz, *J. Mater. Chem. A* **2016**, *4*, 1000.

[17] A. Kaniyoor, R. I. Jafri, T. Arockiadoss, S. Ramaprabhu, *Nanoscale* **2009**, *1*, 382.

[18] M. Batzill, *Surf. Sci. Rep.* **2012**, *67*, 83.

[19] J. Kim, C. Hwan Kwak, W. Jung, Y. Suk Huh, B. Hoon Kim, *Phys. Chem. Chem. Phys.* **2016**, *18*, 15514.

[20] D. A. C. Brownson, C. E. Banks, *Analyst* **2010**, *135*, 2768.

[21] R. Yadav, C. K. Dixit, *J. Sci. Adv. Mater. Devices* **2017**, *2*, 141.

APPENDICES

Appendix I: Raman Data Analysis Mathematica Package (raman.m)

```
(*Save this file in the directory given by:
 FileNameJoin[{$UserBaseDirectory,"Applications"}]
Load the definition with either Needs["raman`"] or Get["raman`"]*)

BeginPackage["raman`"]

ClearAll[importRaman];
ClearAll[doCurve];
ClearAll[doPlot];
ClearAll[mapPlot];
ClearAll[at];
ClearAll[display];
ClearAll[reportColorRange];
ClearAll[trimPoint];

process::usage="process[fname] processes fname into a convenient
 display. Images are displayed, spectra are plotted,
  and maps are averaged, plotted, and histogrammed.
 This should be the most important function to the user."

importRaman::usage="importRaman[fname] Imports Raman Data from
 fname. *Note: only compatible with Rennishaw
 Image files go unprocessed. Unknown file types are disregarded.
 Text files are parsed and identified as either Point Spectra
 or Map Data, and output accordingly.
 Point Spectra: Prints a plot of the spectrum and outputs the
 file name and the calculated data.
 Map Data: Prints a plot of the average spectrum and outputs file
 name and calculated data for every point in the map"
doPlot::usage="doPlot[dat] plots a point spectrum or average
 spectrum with all extra data labeled.
 dat is of the form {fname, data} (i.e. the output of
 importRaman[])"
mapPlot::usage="mapPlot[dat, index] plots a map of the calculated
  value indicated by the integer index.
 To see which \"index\" is which, execute mapPlot[index]"

doCurve::usage=
 "doCurve[data] processes the ordered-pair list data and gives
  the peak information for all detected peaks.
 Optional input \"plotQ\" determines whether the spectrum is
  plotted too.
 Optional input \"dataOut\" determines whether the spectrum data
 is output too."
Begin["`Private`"]
Options[importRaman]={};
importRaman[fname_String,OptionsPattern[]]:=
```

```
  Block[{data,wnCount,map=False},
   If[DirectoryQ[fname],Return[{fname,"Can't import a directory
      this way"}]];
   If[StringMatchQ[fname,"*.bmp"]||StringMatchQ[fname,"*.jpg"],
    Return[{fname,Import[fname]}]];
   If[!StringMatchQ[fname,"*.txt"],
    Return[{fname,"Unknown File Type"}]];
   data=Import[fname,"TSV"];
   If[Length[data[[1]]]==4,wnCount=Length[Tally[data[[All,3]]]];
    map=True;data=Partition[data,wnCount];];
   {fname,data}
   ];
Options[doCurve]={"noiseMultiplier"->2(*how many sigmas of noise
   should peaks exceed?*),
   "plotQ"->False(*print a plot?*),
   "dataOut"->False(*output spectrum data?*),
   "fit"->True(*use a fit to get fwhm?*)};
doCurve[datat_,OptionsPattern[]]:=Block[{data=datat,peaks,
    res,pos,peaks2,nlm,fwhm,ratio,notes={},cutoff,bgPoints,
    mainPeaks={},out=0,out2=0,i=0,p},
   (*The following if statement tests if
   datat is formatted correctly*)
   If[datat[[2,0]]=!=List,If[OptionValue["plotQ"],
     If[datat[[2,0]]===Image,Print[datat[[2]]],
      Print["Error: Incompatible Data"]]];Return["Incompatible data"],

    (*Now begins the meaningful code*)

    (*defines a noise limit for defining peaks*)
    cutoff=OptionValue["noiseMultiplier"]StandardDeviation[
                 HighpassFilter[data[[All,2]],1]];
    (*points used for background identification*)
    bgPoints=Select[Transpose[{data[[All,1]],Range[Length[data]]}],
       #[[1]]<1200||1700<#[[1]]<2300||2900<#[[1]]&][[All,2]];
    (*2nd degree polynomial fluorescence subtraction*)
    data=({#[[1]],#[[2]]-(a+b #[[1]] + c #[[1]]^2)}&/@data)
                 /.FindFit[data[[bgPoints]],a+b xx + c xx^2,{a,b,c},xx];
    peaks=FindPeaks[data[[All,2]],20,.005,cutoff,
      InterpolationOrder->0];(*Where are the peaks?*)
    peaks=Transpose[{peaks[[All,1]],data[[peaks[[All,1]],2]]}];

    (*How close are the peaks in the x-direction*)
    res=SequenceCases[peaks[[All,1]],{x_,y_}:>y-x,Overlaps->True];


    peaks2=If[MemberQ[res,_?(#<50&)],
      pos=SequenceCases[Transpose[{Range[Length[res]],res}],
         {p:_?(#[[2]]<50&)}:>{p}][[All,All,1]];
      SortBy[Join[MaximalBy[#,Last][[1]]&/@Table[
          peaks[[Join[pos[[i,All]],{pos[[i,-1]]+1}]]]
          ,{i,Length[pos]}],peaks[[Complement[Range[Length[peaks]],
           Sort[Join[#,#+1]&@Position[#<50&/@res,True][[All,1]]]]]]],First],
      peaks];(*If any peaks are close together,only take the larger*)

    peaks2=Select[peaks2,51<#[[1]]<Length[data]-51&];
```

```
(*only take peaks far from edges so the fitting works*)

nlm=
 Table[
  (*Print[peaks2[[n,1]]];*)
  If[OptionValue["fit"],
   FindFit[
    N@ToExpression[data[[peaks2[[n,1]]-50;;peaks2[[n,1]]+50]]],
    a/(Pi g) (g^2/((x-x0)^2 + g^2)),
    {{a,peaks2[[n,2]]},{g,20},{x0,data[[peaks2[[n,1]],1]]}},x],
   (*If "fit" False, this segment brute-forces fitting parameters
   out and out2 find the points where the data crosses "half-max"*)
   out=0;out2=0;
   p=peaks2[[n,1]];
   For[i=1,i<=100,i++,
    If[data[[p+i-1,2]]>=  data[[p,2]]/2>= data[[ p+i,2]],
      out=
       NSolve[(data[[p+i,2]]-data[[p+i-1,2]])/
              (data[[p+i,1]]-data[[p+i-1,1]])*(x-data[[p+i-1,1]])+
            data[[p+i-1,2]]==data[[p,2]]/2,x][[1,1,2]];Break[];
      ];
    ];
   For[i=1,i>=-100,i--,
    If[data[[p+i+1,2]]>=  data[[p,2]]/2>= data[[ p+i,2]],
      out2=
       NSolve[(data[[p+i,2]]-data[[p+i+1,2]])
             /(data[[p+i,1]]-data[[p+i+1,1]])*(x-data[[p+i+1,1]])
           +data[[p+i+1,2]]==data[[p,2]]/2,x][[1,1,2]];Break[];
      ];
    ];
   {x0->data[[peaks2[[n,1]],1]],
    a->data[[peaks2[[n,1]],2]]*Pi*Abs[out-out2]/2 ,
    g->Abs[out-out2]/2}
   ],
  {n,Length[peaks2]}];

(*Get position, height, and FWHM for these 4 main peaks*)
If[Length[peaks2]!=0,
 mainPeaks=
  Flatten[Nearest[data[[peaks2[[All,1]],1]]->({x0, a/(g Pi),
          Abs[2 g]}/.nlm),#,{1,50}]]&/@{2700,2450,1580,1350}];

(*Print a plot if desired*)
If[OptionValue["plotQ"],
 Print[ListPlot[{data,datat},PlotRange->All]]];

(*Give xy data as ordered pairs if desired*)
If[OptionValue["dataOut"],{#,data},{#}]&@
 If[Length[mainPeaks]!=0,
  ({
      (*2D/G ratio*)
      If[Length[#[[1]]]!=0&&Length[#[[3]]]!=0,#[[1,2]]/#[[3,2]],0],
      (*D/G Ratio*)
      If[Length[#[[4]]]!=0&&Length[#[[3]]]!=0,#[[4,2]]/#[[3,2]],0],
      (*2D fwhm*)
```

```
          If[Length[#[[1]]]!=0,#[[1,3]],0],
          (*2D location*)
          If[Length[#[[1]]]!=0,#[[1,1]],0],
          (*G fwhm*)
          If[Length[#[[3]]]!=0,#[[3,3]],0],
          (*G location*)
          If[Length[#[[3]]]!=0,#[[3,1]],0],
          (*give all peak information (not just the 4 main ones)*)
          ({x0, a/(g Pi),Abs[2 g]}/.nlm)
          }&[mainPeaks]),
      {0,0,0,0,0,0,{mainPeaks}}]
    ]];
Options[doPlot]={};
doPlot[datat_,OptionsPattern[]]:=
  Block[{fname=datat[[1]],data=datat[[2]],pdata,
    map=Depth[datat[[2]]]!=3},
   If[data[[0]]=!=List,Return["Incompatible data"]];

   (*If data is just one spectrum, process it and get the num. data
   If it is a map, average all the points (just for a quick visual)*)
   pdata=If[Depth[data]==3,
     doCurve[data,"plotQ"->False,"dataOut"->True],
     data=Mean[data][[All,{3,4}]];
     doCurve[data,"plotQ"->False,"dataOut"->True]
     ];
   (*Much of the following is just formatting for aesthetics
   The end result is just a plotted spectrum*)
   ListPlot[
    {#[[1]],30Length[pdata[[2]]]#[[2]]/
         Total[pdata[[2,All,2]]]}&/@pdata[[2]]
    (*normalize data by total number of counts*)
    ,PlotRange->{All,{-350,All}},Axes->{True,False},
    Joined->True,PlotMarkers->None,
    PlotLabel->Style["Raman Spectrum: "<>Last@FileNameSplit@fname<>
       "\n"<>If[map,"Map Average","Point Spectrum"],
      Black,Bold,14],
    ImageSize->Large,
    Epilog->Join[Flatten[({
           Black,Inset[Framed[Style["\!\(\*OverscriptBox[\(ν\), \(~\)]\):"
               <>ToString[#[[1]]]<>"\nσ:"<>ToString[#[[3]]]<>"\nI:"<>
               ToString[#[[2]]],10],Background->LightYellow],{#[[1]],-200}],
           Red,Line[{{#[[1]],-20},{#[[1]],1*^7}}]
           }&/@pdata[[1,-1,All]])],
      {Black},
      {Arrow[{Scaled[{0.2,0.7}],If[pdata[[1,2]]==0,
          Scaled[{0.2,0.7}],{1350,0}]}]},
      {If[pdata[[1,2]]==0,
        Inset[Framed[Style["No defect peak",12],Background->LightYellow],
         Scaled[{0.2,0.7}]],
        Inset[Framed[Style["\!\(\*SubscriptBox[\(I\), \(D\)]\)/\!\(\*
            SubscriptBox[\(I\), \(G\)]\) = "<>ToString[pdata[[1,2]]],12],
          Background->LightYellow],Scaled[{0.2,0.7}]]]},
      {Arrow[{Scaled[{0.9,0.7}],If[pdata[[1,1]]==0,Scaled[{0.9,0.7}],
          {2690,0}]}]},
      {If[pdata[[1,1]]==0,
```

```
        Inset[Framed[Style["No C",12],Background->LightYellow],
         Scaled[{0.2,0.7}]],
        Inset[Framed[Style["\!\(\*SubscriptBox[\(I\), \(2  D\)]\)/\!\(\*
            SubscriptBox[\(I\), \(G\)]\) = "<>ToString[pdata[[1,1]]],12],
          Background->LightYellow],Scaled[{0.9,0.7}]]]}],
    PlotMarkers->{Automatic,Small}]
   ];
Options[mapPlot]={"plotOptions"->{Mesh->None,
     InterpolationOrder->0,ColorFunction->GrayLevel},"parallel"->True,
   "fit"->False};
mapPlot[index_Integer]:=
  "This index gives: "<>Switch[index,
    1,"\!\(\*SubscriptBox[\(I\), \(2  D\)]\)/\!\(\*SubscriptBox[\(I\),
     \(G\)]\)",
    2,"\!\(\*SubscriptBox[\(I\), \(D\)]\)/\!\(\*SubscriptBox[\(I\),
     \(G\)]\)",
    3,"2D FWHM",
    4,"Wavenumber(\!\(\*OverscriptBox[\(ν\), \(~\)]\)) 2D",
    5,"G FWHM",
    6,"Wavenumber(\!\(\*OverscriptBox[\(ν\), \(~\)]\)) G"];
mapPlot[dat_,index_,OptionsPattern[]]:=Block[{fname=dat[[1]],
    coords=dat[[2,All,1,{1,2}]],data=dat[[2,All,All,{3,4}]],directory,
    values,outDimension,index2,plot,colors,range,contour},

   If[$ProcessorCount<8&&True
    (*&&true forces this to never run in parallel.
    Remove if using a capable machine and doing a lot of data*),
    data=Map[doCurve[#,"fit"->False]&,data];,
    DistributeDefinitions[doCurve];

    data=ParallelMap[doCurve[#,"fit"->False]&,data];
    ];

   index2=If[Length[index]!=0,Select[index,1<=#<=6&],
     Clip[index,{1,6}]];If[index2=={},Return["No valid indices" ]];
   (*only take valid index values*)
   outDimension=Length[index2];

   values=MapThread[Join[#1,If[Length[#2]!=0,#2,{#2}]]&,
     {coords,data[[All,1,index2]]}];

   Table[
    {plot,colors,range}=reportColorRange[ListDensityPlot[
       values[[All,{1,2,2+i}]]
       ,
       Mesh->None,InterpolationOrder->0,ColorFunction->GrayLevel,
       ImageSize->Medium,Frame->False
       ]];
    contour=display[  {
       Show[
         Graphics[{Style[Text[ToString[fname]<>"\nViewing "<>
              ToString[Abs[Min[#]-Max[#]]&[coords[[All,1]]]]<>"µm by "<>
              ToString[Abs[Min[#]-Max[#]]&[coords[[All,2]]]]<>"µm"<>"map of:"
              <>Switch[
               If[outDimension==0,index2,index2[[i]]],
```

```
              1,"\!\(\*SubscriptBox[\(I\), \(2
D\)]\)/\!\(\*SubscriptBox[\(I\),
               \(G\)]\)",
              2,"\!\(\*SubscriptBox[\(I\),
\(D\)]\)/\!\(\*SubscriptBox[\(I\),
              \(G\)]\)",
              3,"2D FWHM",
              4,"Wavenumber(\!\(\*OverscriptBox[\(ν\), \(~\)]\)) 2D",
              5,"G FWHM",
              6,"Wavenumber(\!\(\*OverscriptBox[\(ν\), \(~\)]\)) G"]

            ,Scaled[{.3,1.1}]],Black,Bold,12],Yellow,
          Rectangle[Scaled[{0.022,0.022}],Scaled[{.978,.978}]]}],
        plot
        ]//at[{0,0},Scaled[{.85,1}]],colorLegend[colors,range,10]
       //at[{0.85,.05},Scaled[{.15,1}]]},AspectRatio->01,
      ImageSize->Medium]
    ,{i,Length[values[[1]]]-2}]
   ];

(*Plot Formatting, extra functions*)
reportColorRange[plotFunction_]:=Module[{p,min,max,plotHead,
   plotBody,colFunc,colScale,h,b,cf,cfs},{plotHead,plotBody}=
   First@Cases[Hold[plotFunction],h_[b__]->{h,Hold[b]},1];

  colFunc=Replace[
    First@Join[Cases[plotBody,HoldPattern[ColorFunction->cf_]->cf],
      {ColorData["LakeColors"]}
      ],s_String:>ColorData[s]];
  colScale=First@Append[Cases[plotBody,
      HoldPattern[ColorFunctionScaling->cfs_]->cfs],True];
  plotBody=plotBody/.HoldPattern[ColorFunction->_]|HoldPattern[
       ColorFunctionScaling->_]->Sequence[];
  {min,max}={Min[#],Max[#]}&@Flatten@Last@Reap[p=Apply[plotHead,
         Join[plotBody,Hold[ColorFunction->{(Sow[#];Hue[#])&},
           ColorFunctionScaling->False]
          ]]];
  {If[Cases[p,Hue[_],Infinity]=!={},If[colScale,p/.Hue[x_]:>
       colFunc[(x-min)/(max-min)],p/.Hue[x_]:>colFunc[x]],plotFunction],
   colFunc,{min,max}}
  ]
SetAttributes[reportColorRange,HoldAll];

trimPoint[n_,digits_]:=NumberForm[n,digits,NumberFormat->
   (DisplayForm@RowBox[Join[{StringTrim[#1,
          RegularExpression["\\.$"]]},If[#3!="",{"*",
          SuperscriptBox[#2,#3]},{}]]]&)]
at[position_,scale_: Automatic][obj_]:=
  Inset[obj,position,{Left,Bottom},scale];
colorLegend[cFunc_,range_,n_,opts:OptionsPattern[]]:=
 Module[{frameticks},frameticks={If[TrueQ["LeftLabel"/.{opts}],
       Reverse[#],#]&@{None,Function[{min,max},{#,trimPoint[#,
           ("Digits"/.{opts}/."Digits"->3)],{0,.1}}&/@Table[min+(i-1)
           (max-min)/(n-1),{i,n}]]},{None,None}};
  Framed[Graphics[Inset[Graphics[Raster[Transpose@{Map[
```

```
          List@@ColorConvert[cFunc[#],RGBColor]&,(Range[10n-1]-1)/(10n-2)]}],
      ImagePadding->0,PlotRangePadding->0,AspectRatio->Full],
     {0,First[range]},{0,0},{1,range[[-1]]-range[[1]]}],
    PlotRange->{{0,1},range[[{1,-1}]]},Frame->True,
    FrameTicks->frameticks,LabelStyle->(LabelStyle/.{opts}/.
       LabelStyle->Black),PlotRangePadding->0,AspectRatio->Full],
   Background->(Background/.{opts}/.Background->LightGray),
   FrameStyle->(FrameStyle/.{opts}/.FrameStyle->None),
   RoundingRadius->(RoundingRadius/.{opts}/.RoundingRadius->10)]]
display[g_,opts:OptionsPattern[]]:=
 Module[{frameOptions=FilterRules[{opts},Options[Graphics]]},
  Graphics[g,PlotRange->{{0,1},{0,1}},
   Evaluate@Apply[Sequence,frameOptions]]]

Options[process]={};
SetAttributes[process,Listable];
process[fname_String,OptionsPattern[]]:=
  Block[{data},
   If[DirectoryQ[fname],
     (
        data=importRaman[#];
        If[data[[2,0]]===Image||data[[2,0]]===String,Return[data]];
        If[Depth[data[[2]]]==3,
         Return[doPlot[data]];,
         Return[{doPlot[data],mapPlot[data,{1,3}]}]];
        Return["???"]
        )&[FileNames["*",{fname}]]
     ,
     data=importRaman[fname];
     If[data[[2,0]]===Image||data[[2,0]]===String,Return[data]];
     If[Depth[data[[2]]]==3,
      Return[doPlot[data]];,
      Return[{doPlot[data],mapPlot[data,{1,3}]}]];
     Return["???"]
     ];];

End[]
EndPackage[]
```

Appendix II: Sample Outputs for Raman Data

Single Spectrum

A single Raman spectrum from a point on a sample is saved as a tab-separated text file containing 2 columns (corresponding to wavenumber and counts) and N rows, where N is the total number of wavenumber bins. A sample output from running the command "process[filename]" or "doPlot[{filename,data}]" on one of these files is shown below.

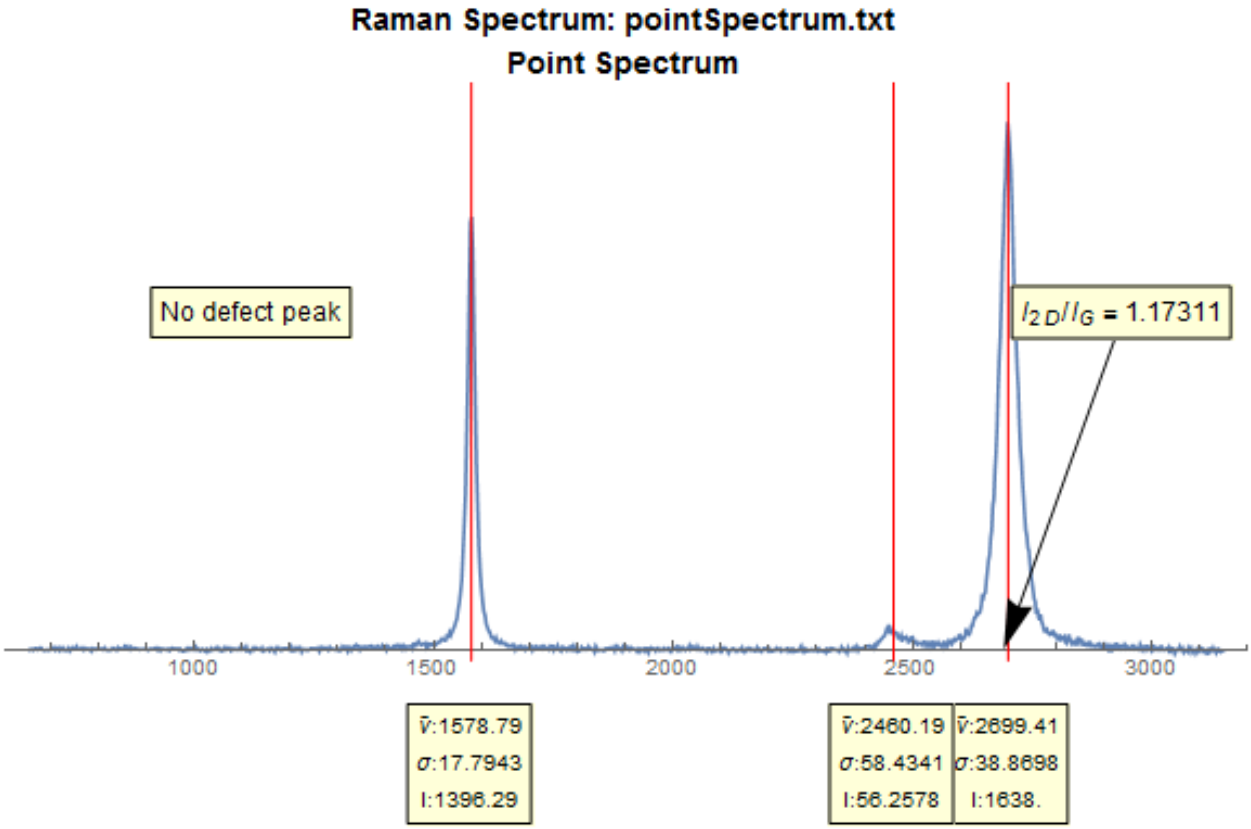

Map Spectra

Map data is saved as a tab-separated text file with four columns (corresponding to x-position, y-position, wavenumber, and counts) and $N \times M$ rows, where N is the total number of wavenumber bins and M is the total number of points in the Raman map. Sample outputs are given below for the mapPlot function. The six plots are maps of: (i) intensity ratio I_{2D}/I_G, (ii) defect-to-G intensity ratio I_D/I_G, (iii) 2D-peak FWHM, (iv) 2D-peak location, (v) G-peak FWHM, and (vi) G-peak location. All maps are for the same sample; a SiO_2/Si chip coated with Ni and then modified with a multi-layer graphene film.

ramanMap.txt
Viewing 23.μm by 27.μm map of: I_{2D}/I_G

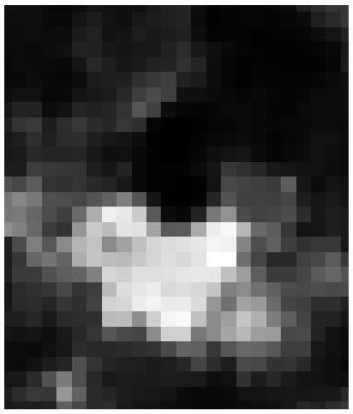

ramanMap.txt
Viewing 23.μm by 27.μm map of: I_D/I_G

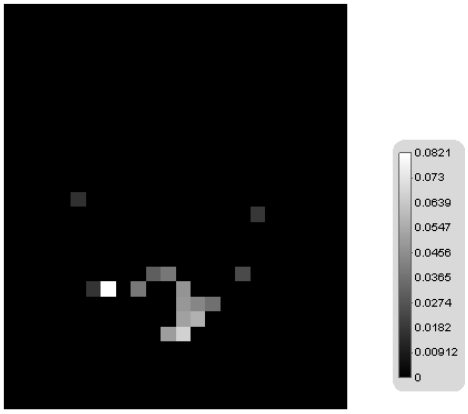

ramanMap.txt
Viewing 23.μm by 27.μm map of: 2D FWHM

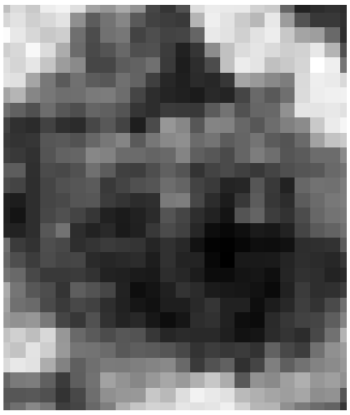

ramanMap.txt
Viewing 23.μm by 27.μm map of: Wavenumber ($\tilde{\nu}$) 2D

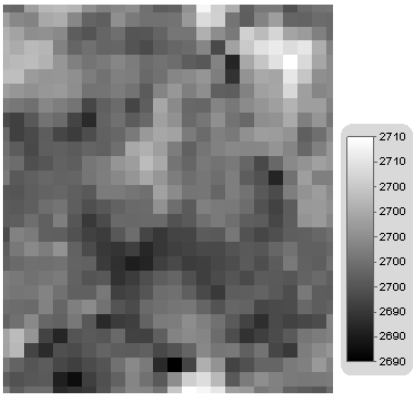

ramanMap.txt
Viewing 23.μm by 27.μm map of: G FWHM

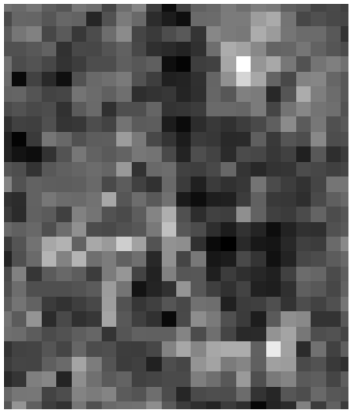

ramanMap.txt
Viewing 23.μm by 27.μm map of: Wavenumber ($\tilde{\nu}$) G